# CRYSTAL FIELD EFFECTS IN MANTLE MINERALS

Thesis by

Edward S. Gaffney

In Partial Fulfillment of the Requirements

For the Degree of

Doctor of Philosophy

California Institute of Technology

Pasadena, California

1973

(Submitted September 21, 1972)

ACKNOWLEDGEMENT

The author acknowledges the assistance and encouragement of Professors Thomas J. Ahrens and George R. Rossman with the experimental portions of this work. Professor Don L. Anderson participated in many invaluable discussions on the nature and effects of iron in the lower mantle. In the design of the shock-wave spectrographic system, the help of John Lower, Hallett Swift and Earl J. Bunker, Jr. was greatly appreciated. The author benefited from several discussions on crystal field theory with Jack Thibeault who also provided some of the computer software used. Professors Ahrens and Rossman critically read the manuscript prior to its completion. Several comments by Professor Kamb have also been helpful.

Conversations with fellow students have been very valuable in the production of this thesis. The author is especially indebted to Peter Lagus, Rex Gibbons and Geoffrey Davies. The work described herein was supported by the National Science Foundation.

ABSTRACT

The behavior of $Fe^{2+}$ in the lower mantle will depend on the effects of crystal fields. A point charge model, scaled to fit observed spectra at low pressures is developed to predict these effects. Two of the three parameters needed to predict spin-pairing transitions can only be determined from spin-forbidden electronic transitions. The spectra of garnet, gillespite and peridot are examined and found to have such absorption features. Assignment of these spectra leads to values of the Racah parameters, B and C, as well as the crystal field parameter Dq.

A new experimental technique, which allows the measurement of optical absorption spectra of solids in the visible region during shock loading, is described. Results are discussed for periclase and ruby. The ruby data indicate that the point charge model is good to at least 15 percent (volume) compression.

The effects of low-spin $Fe^{2+}$ in the earth's lower mantle are investigated in considerable detail. The existence of low-spin $Fe^{2+}$ permits the formation of a separate phase since $Mg^{2+}$ and low-spin $Fe^{2+}$ may not form solid solutions. The bulk elastic behavior of such phases

is predicted from volume-bulk modulus systematics and compared with available shock wave data. It is likely that the high pressure phases of several ferrous iron compounds involve low-spin $Fe^{2+}$. Iron will be spin-paired in the mantle below 1200 km and likely at higher levels as well. The observed density and bulk modulus in the lower mantle are inconsistent with any combination of phases in a pyrolite bulk composition but can be fit quite well by a model with all $Fe^{2+}$ spin-paired below 630 km and nearly olivine composition at that depth, with MgO decreasing to almost a pyroxene composition at the core.

An origin of the upper mantle from the lower mantle by chemical fractionation is proposed. The spin-pairing of $Fe^{2+}$ provides an excellent mechanism for both iron and silicon enrichment in the lower mantle by partial melting yielding a pyrolite upper mantle, and hence, a chemically inhomogeneous mantle. This removes the motivation for reducing FeO and $SiO_2$ in the mantle to supply Fe and Si for the core.

TABLE OF CONTENTS

# LIST OF TABLES

Chapter V (continued)

# LIST OF FIGURES

Chapter II



Chapter III

Chapter III (continued)



Chapter IV

Chapter V

# I. INTRODUCTION

Iron is an important constituent of the earth's mantle; for this reason the behavior of iron-bearing minerals under compression is of considerable interest to geophysics. The presence of ferrous iron in the mantle will effect its density, its seismic properties, both elastic and anelastic, its thermal and electrical conductivity and perhaps even its mineralogical character.

The present study is an attempt to apply available theoretical projections, aided by a new experimental technique, to the question of how ferrous minerals behave at high pressures, and how this will affect the properties of the mantle. The chemical and physical behavior of iron (as is the case with most transition metals) in solids is primarily governed by the effects considered in crystal field theory. Chapter II briefly reviews some of the bases of this theory and discusses in some detail the point charge approximation. In Chapter III the spectra of several iron-bearing minerals at atmospheric pressure are considered using (in part) the theory of Chapter II. This is done so as to more precisely determine several of the parameters used in applying

crystal field theory. In Chapter IV a technique for measuring optical absorption spectra at very high dynamic stresses is described and some experimental results obtained with this technique are discussed. It is found that there is some cause for optimism in the use of the approach of Chapter II at high pressures. Finally, in Chapter V, the earlier chapters are synthesized into a mantle model for the behavior of $Fe^{2+}$. Starting with the model of Ringwood, some modifications are in order and many physical and chemical properties can be predicted. Of particular import is a proposed change in the ground state of $Fe^{2+}$ in the intermediate region of the mantle.

## II. A BRIEF OUTLINE OF CRYSTAL FIELD THEORY

The energy states of a transition metal ion in a crystal or complexed in solution can be fairly well understood in terms of crystal field theory. The theory considers the perturbation on the free-ion energies by the electric field of the surrounding atoms. A fairly comprehensive review of the theory is found in books by Griffiths (1) and Ballhausen (2) and the reader is referred thereto for details. Here only the broad outline of the theory and such details as are of immediate interest are given. First a general transition metal is considered with six nearest neighbors octahedrally situated, followed by some remarks about other symmetries. Then the question of how the effects of crystal fields can be estimated a priori, that is, when we have no spectra from which to infer the energies of states involved, is discussed. And finally some practical matters concerning the use of energy level diagrams in interpreting transition metal spectra are considered.

### A. Octahedral Symmetry

The transition elements are distinguished by the presence of d-electrons in their ground states. There are

five d-orbitals which, in the free ion, are degenerate. In the presence of an electric field however, this degeneracy may be removed.

Consider the case of an ion with d-orbitals placed in a site surrounded by six anions situated at the vertices of an octahedron. Choose the x, y, and z axes of the ion to correspond with the four-fold axes of the octahedron. The five d-orbitals are conveniently expressed in terms of spherical harmonics $Y_\ell^m$ as

$$d_{z^2} = Y_2^0$$

$$d_{x^2 - y^2} = \frac{1}{\sqrt{2}} (Y_2^2 + Y_2^{-2})$$

$$d_{xy} = \frac{1}{i\sqrt{2}} (Y_2^2 - Y_2^{-2})$$

$$d_{xz} = -\frac{1}{\sqrt{2}} (Y_2^1 - Y_2^{-1})$$

$$d_{yz} = -\frac{1}{i\sqrt{2}} (Y_2^1 + Y_2^{-1})$$

where the first two orbitals concentrate charge along the x, y, and z axes and the latter three orbitals concentrate it between the axes. Therefore, the first two orbitals will have higher energy than the latter ones. In fact, it can be shown that the first two are degenerate, as are the

other three. So the effect of surrounding this ion by six anions thusly has been to split the five degenerate d-orbitals into two sets (called $e_g$ for $d_{z^2 - y^2}$, and $t_{2g}$ for the others) separated by some energy which is conventionally called either $\Delta$ or 10 Dq. In Section C it is shown that, in the approximation that the surrounding ions are point charges, the magnitude of Dq will vary as $R^{-5}$ where R is the interionic distance.

If the central ion has only one d-electron (such as $Ti^{3+}$ which has the electronic structure $\left[1s^2\ 2s^2\ 2p^6\ 3s^2\ 3p^6\right]3d^1$ or more briefly $3d^1$) a determination of the energy levels of the orbitals completes the problem since there is no appreciable electron repulsion between the electrons in the argon shell (in square brackets) and the 3d electrons. (Throughout this discussion we ignore the effects of spin-orbit coupling on energy of states.) There are only two states in which the $3d^1$ system can be, either $t_{2g}^{\ 1}$ or $e_g^{\ 1}$, separated by energy $\Delta$.

Adding another electron considerably complicates matters since repulsion between two d-electrons must now be considered. Two electrons with wave functions $\psi_1$ and $\psi_2$ will interact to give an additional term to the energy.

This energy involves integrals of the form

$$\iint \psi_1^* \, \psi_2^* \, \frac{e^2}{r_{12}} \, \psi_2 \, \psi_1 \, d\tau_1 \, d\tau_2$$

whose evaluation is lucidly discussed by Ballhausen (2, pp. 19-21). Suffice it here to say that their effect, for 3d orbitals, can be expressed in terms of two parameters B and C, called Racah parameters. They introduce off-diagonal terms into the energy matrices and thereby give rise to considerable complication of the solution of energy of states. As interatomic distances decrease the electrons will tend to expand out toward the surrounding ions thereby decreasing their interaction with each other and thereby decreasing the Racah parameters so that in a very general sense, B and C are indicative of the degree of covalency of the metal-oxygen bonds. These parameters should therefore, decrease with compression, since the degree of covalency should increase. Unfortunately it is not possible to be more explicit regarding the details of this variation with R. In Chapter III the limited experimental data will be applied to this problem.

For the octahedral symmetry presently under discussion the complete energy matrices for $d^n$ systems have been worked out in terms of Dq, B and C by Tanabe and Sugano (3).

B. Other Symmetries

Further changes in the energy levels can be expected for atomic arrangements other than octahedral. As long as the symmetry belongs to one of the "cubic" groups ($T_d$ or $O_h$) exactly the same formalism and even the same energy matrices will apply. The only changes will be in the values of Dq, B and C. At least four common coordination polyhedra belong to the cubic groups; in addition to the octahedron, they are the tetrahedron, cube and dodecahedron (110). For these figures (using the methods of Section C) the relations for constant R can be derived as follows

$$-\frac{9}{4}\,Dq(\text{tetra.}) = Dq(\text{octa.}) = -\frac{9}{8}\,Dq(\text{cube}) = -2\,Dq(\text{dodeca.}).$$

If there were no change of interatomic distance with coordination the revised Dq values could be used in the matrices to get the revised energies. However, in general,

$$R(\text{tetra.}) < R(\text{octa.}) < R(\text{cube}) < R(\text{dodeca.}) .$$

The change in R will effect Dq, B and C so that one should expect

B, C(tetra.) < B, C(octa.) < B, C(cube) < B, C(dodeca.)

and using the $R^{-5}$ dependence of Dq,

$$-\frac{9}{4} R^5(\text{tetra.})\, Dq(\text{tetra.}) = R^5(\text{octa.})\, Dq(\text{octa.})$$
$$= -\frac{9}{8} R^5(\text{cube})\, Dq(\text{cube})$$
$$= -2\, R^5\, (\text{dodeca.})\, Dq(\text{dodeca.}).$$

For lower symmetries (which do not belong to the cubic groups) the situation is more complicated. The $e_g$ and $t_{2g}$ sets of orbitals may be split into several non-degenerate orbitals. This will change the states available to the system so that, in general, the matrices of Tanabe and Sugano will no longer be valid. More than one parameter will be required to completely describe the direct effects of the crystal field. The number of such parameters can be as great as 14 for $C_1$ symmetry, but for most cases we will be interested in, is no more than four. (See Table 8.1, p. 199 in (1).) In the next section some lower symmetry environments are discussed in the point charge approximation.

In the cases of $D_4$, $C_{4v}$, $D_{2d}$, and $D_{4h}$ symmetry the matrix elements including the crystal field and electron repulsion (but no spin-orbit coupling) have been determined by Otsuka (4) in terms of the one-electron energy levels and the two Racah parameters. These symmetries include many sites of particular interest to us including the $Fe^{2+}$ site in gillespite, the M1 site in olivine (approximately) and the $Fe^{2+}$ site in garnet. By comparing observed and calculated energies in these minerals it should therefore, be possible to determine the values of the Racah parameters in these three quite dissimilar environments.

C. Point Charge Calculations

The earth's mantle is under high pressures (greater than one megabar at the core) and most of the minerals have structures which have never been observed isochemically in the laboratory. For this reason one is tempted to estimate the crystal fields involved so that one may predict some of the properties of these minerals. A point charge approximation is used here to do so. The general method and some comments on the validity of the technique are given in this section, but the detailed application of the method will be the subject of Chapter V.

The point charge approximation will be developed here after the manner of Hutchings (5). For any arrangement of n point charges about a site $(R_i, \theta_i, \phi_i)$, the field can be expanded as a sum of spherical harmonics.

$$V(r,\theta,\phi) = \sum_{i=1}^{n} q_i \sum_{\ell} \frac{r_<^{\ell}}{r_>^{\ell+1}} \frac{4\pi}{(2\ell+1)} \sum_{m=-\ell}^{\ell} Y_{\ell}^{m*}(\theta_i,\phi_i) Y_{\ell}^{m}(\theta,\phi) \tag{1}$$

where $q_i$ is the charge on the $i^{th}$ ion, $r_<$ is the smaller of r and $R_i$, the radii of the field point and the $i^{th}$ source point respectively, and the $Y_{\ell}^{m}$ are spherical harmonics. Only that part of the field which can interact with 3d electrons is of interest so only even values of $\ell$ less than or equal to 4 need be considered. This considerably simplifies equation (1).

Equation (1) can be reduced to:

$$V(r,\theta,\phi) = \sum_{\ell} \sum_{m=-\ell}^{\ell} \frac{r_<^{\ell}}{r_>^{\ell+1}} \gamma_{\ell m} Y_{\ell}^{m}(\theta,\phi) \tag{2}$$

where

$$\gamma_{\ell m} \equiv \frac{2\sqrt{2\pi}}{(2\ell+1)} \sum_{i=1}^{n} Y_{\ell}^{m*}(\theta_i, \phi_i) \tag{3}$$

if all the ligands are at the same distance and have the same charge q. The former restriction is relaxed below. For many symmetries most of the $\gamma_{\ell m}$ will vanish.

Having expressed the potential $V(r, \theta, \phi)$ the energies can now be obtained by direct integration of the wave functions

$$E_{ab} = \int d\tau \ (\psi_a^* \ V(\tau) \ \psi_b)$$

$$= \sum_{\ell} \sum_{m=-\ell}^{\ell} \int d\tau \left[ R_a^*(r) Y_{\ell_a}^{m_a *} \ \gamma_{\ell m} \frac{r_<^{\ell}}{r_>^{\ell+1}} \ Y_{\ell}^{m}(\theta,\phi) R_b(r) Y_{\ell_b}^{m_b} \right]$$

where $R_a(r)$ is the radial part of the $a^{th}$ wave function and $Y_{\ell_a}^{m_a}$ is the angular part. For 3d electrons this becomes

$$E_{ab} = \sum_{\ell} \sum_{m=-\ell}^{\ell} R_{\ell} \int Y_2^{m_a *} \ Y_{\ell}^{m} \ Y_2^{m_b} \ \gamma_{\ell m} \ d\Omega$$

where

$$R_{\ell} \equiv q \sqrt{\pi/2} \ \int_o^{\infty} \frac{r_<^{\ell}}{r_>^{\ell+1}} \ R_a^*(r) \ R_b(r) \ r^2 \ dr \ . \qquad (4)$$

Using

$$c^k(\ell m, \ell' m') \equiv \sqrt{\frac{2}{2k+1}} \int_o^{\pi} P_k^{m-m'}(\cos\theta) P_{\ell}^{m}(\cos\theta) P_{\ell'}^{m'}(\cos\theta) \sin^2 d\theta$$

this reduces to

$$E_{ab} = \sum_{\ell} \sum_{m=-\ell}^{\ell} R_{\ell} \ \gamma_{\ell m} \ c^{\ell}(2m_a, \ 2m_b) \ \delta(m - m_a + m_b) \qquad (5)$$

The $c^k$'s are tabulated in various books (e.g., (2) p. 20 ). The $R_{\ell}$'s will be discussed shortly.

For most choices of coordinate axes the best angular functions are not the pure $Y_2^{m_a}$'s used above but the linear combinations given earlier (Section A). The energy of these combined orbitals is easily calculated, from the $E_{ab}$ of equation (5).

$$\left.\begin{aligned} E(d_{z^2}) &= E_{00} \\ E(d_{x^2-y^2}) &= \tfrac{1}{2}\,(E_{22} + 2E_{2-2} + E_{-2-2}) = E_{22} + E_{2-2} \\ E(d_{xy}) &= E_{22} - E_{2-2} \\ E(d_{xz}) &= E_{11} - E_{1-1} \\ E(d_{yz}) &= E_{11} + E_{1-1} \end{aligned}\right\} \quad (6)$$

Now consider the radial parts of the integrals as expressed in Equation (4). The radial wave functions, $R_a(r)$ and $R_b(r)$ do not depend explicitly on the interionic distance R so that the R dependence of the integrals will be contained entirely in the term $r_<^{\ell}/r_>^{\ell+1}$. Furthermore, $R_a(r)$ and $R_b(r)$ will be quite small for $r > R$ so

$$R_\ell = \int_o^R \frac{r^{\ell+2}}{R^{\ell+1}} R_a^*(r)R_b(r)dr + \int_R^\infty \frac{R^\ell}{r^{\ell-1}} R_a^*(r)R_b(r)dr$$

$$\int_o^\infty \frac{r^{\ell+2}}{R^{\ell+1}} R_a^*(r)R_b(r)dr = \frac{1}{R^{\ell+1}} \int_o^\infty r^{\ell+2} R_a^*(r)R_b(r)dr .$$

The integral in this expression does not depend explictly on R so

$$R_\ell \simeq \frac{A_\ell}{R^{\ell+1}} \tag{7}$$

where

$$A_\ell = \int_o^\infty r^{\ell+2} R_a^*(r)R_b(r)dr . \tag{7a}$$

Only $\ell = 0, 2, 4$ are important here:

$$R_0 = \frac{A_0}{R}, \qquad R_2 = A_2/R^3, \qquad R_4 = A_4/R^5 . \tag{8}$$

If the ligands are at different distances $r_i$ then pick some $r_0$ and rewrite (3) as

$$\gamma'_{\ell m} \equiv \frac{2\sqrt{2\pi}}{(2\ell+1)} \sum_{i=1}^{n} \frac{r_0^{\ell+1}}{r_i^{\ell+1}} Y_\ell^{m*}(\theta_i, \phi_i) \tag{3'}$$

and

$$R'_\ell \simeq \frac{A_\ell}{r_0^{\ell+1}} \tag{7'}$$

and use $\gamma'_{\ell m}$ and $R'_\ell$ in (5) to get the $E_{ab}$'s.

The next step is the downfall of all point charge calculations for transition elements. Whatever type of wave functions are used in Equation (7a), the values of $A_l$ is grossly in error compared with the observed spectra. The plan here is to use these calculations to predict the crystal field of $Fe^{2+}$ minerals in the mantle which suggests the following approach. Consider a wide variety of environments represented in low pressure spectra and choose $A_l$'s to best fill <u>all</u> of the observed data.

Three spectra have been used to evaluate $A_2$ and $A_4$: gillespite and two olivines. All have $Fe^{2+}$ in $D_{4h}$ (tetragonal) symmetry so that both terms are involved in the spectra. For the olivine of intermediate composition the energies have been calculated using a coordination of the $M_1$ site which is the average of $Fe^{2+}$ and $Mg^{2+}$ as determined by x-ray diffraction. Values of bond lengths of the separate elements almost certainly are not equal to this average, so that larger errors are to be expected from the calculations in olivine. Values of $A_2$ and $A_4$ were adjusted so as to give a good fit to all six energy levels simultaneously, and the results are shown in Table 1.

TABLE 1

SPECTRA OF OLIVINE AND GILLESPITE (OBSERVED AND CALCULATED).

| Mineral | $r_0$(Å)[d] | $\nu_1$($cm^{-1}$) (calculated) | $\nu_1$($cm^{-1}$) (observed) | $\nu_2$($cm^{-1}$) (calculated) | $\nu_2$($cm^{-1}$) (observed) |
|---|---|---|---|---|---|
| Gillespite[a] $BaFe_2Si_4O_{10}$ | 2.003 | 20260 | 19000 | 6990 | 7500 |
| Olivine[b] $Mg_{1.6}Fe_{0.4}SiO_4$ | 2.08 | 11410 | 11660 | 9740 | 9000 |
| Fayalite[c] $Fe_2SiO_4$ | 2.125 | 10590 | 11000 | 8140 | 8000 |

a. Spectral and structural data from (6).

b. Structure from (7); spectrum interpolated from (7). Values quoted are for the $D_{4h}$ M1 site only.

c. Spectral and structural data from (8). Values quoted are for the $D_{4h}$ and M1 site only.

d. $r_0$ is the smallest interatomic distance.

There are several sources of error in the procedure described, most deriving from the model. The errors involved in the point charge approximation are discussed in the chemical literature (5, 9) and are of moderate size. The assumption of ionic bonding is probably quite good for Fe-O bonds.

An estimate of the errors involving the magnitude of the radial integrals can be made from Table 1 which compares the calculated and observed spectra of olivines and gillespite. The errors are about 10 percent.

The method described here can be used to calculate the one-electron energy levels for the case of octahedral coordination. When this is done it is found that

$$E(x^2 - y^2) - E(xy) = \frac{10}{3} R_4$$

but in Section A that energy difference was defined to be 10 Dq or $\Delta$ so

$$Dq = \frac{1}{3} R_4 \ .$$

Then using (8)

$$Dq = \frac{A_4}{3R^5}$$

or

$$Dq \propto \frac{1}{R^5} \ .$$

D. Energy Level Diagrams

The standard technique for displaying energy levels of transition metal ions is to plot them as functions of the strength of the crystal field, the so-called Tanabe-Sugano diagram. These diagrams assume a particular B and C. (Berkes (10) has compiled several Tanabe-Sugano diagrams for a variety of systems.) For most of the present purposes such plots are not very convenient because it is usually much easier to determine the crystal field from the spectra than the Racah parameters. It makes more sense, therefore, to plot energy levels as functions of B or C while keeping the crystal field constant. Figures 1 through 6 show such plots for $Fe^{2+}$ in a variety of coordinations and a range of C/B in each coordination. The point of chief interest is that the spin-allowed bands in each diagram are independent of the Racah parameters (in the high-spin case) but they do depend on the crystal field. Therefore, these bands can be used to fix the crystal field while B and C are obtained from the spin-forbidden bands.

Figure 1

Energy of states of $Fe^{2+}$ in an octahedral field ($Dq = 1000\ cm^{-1}$) as a function of B for constant C/B. Heavy lines are quintet states. Some of the lower excited states are labelled.

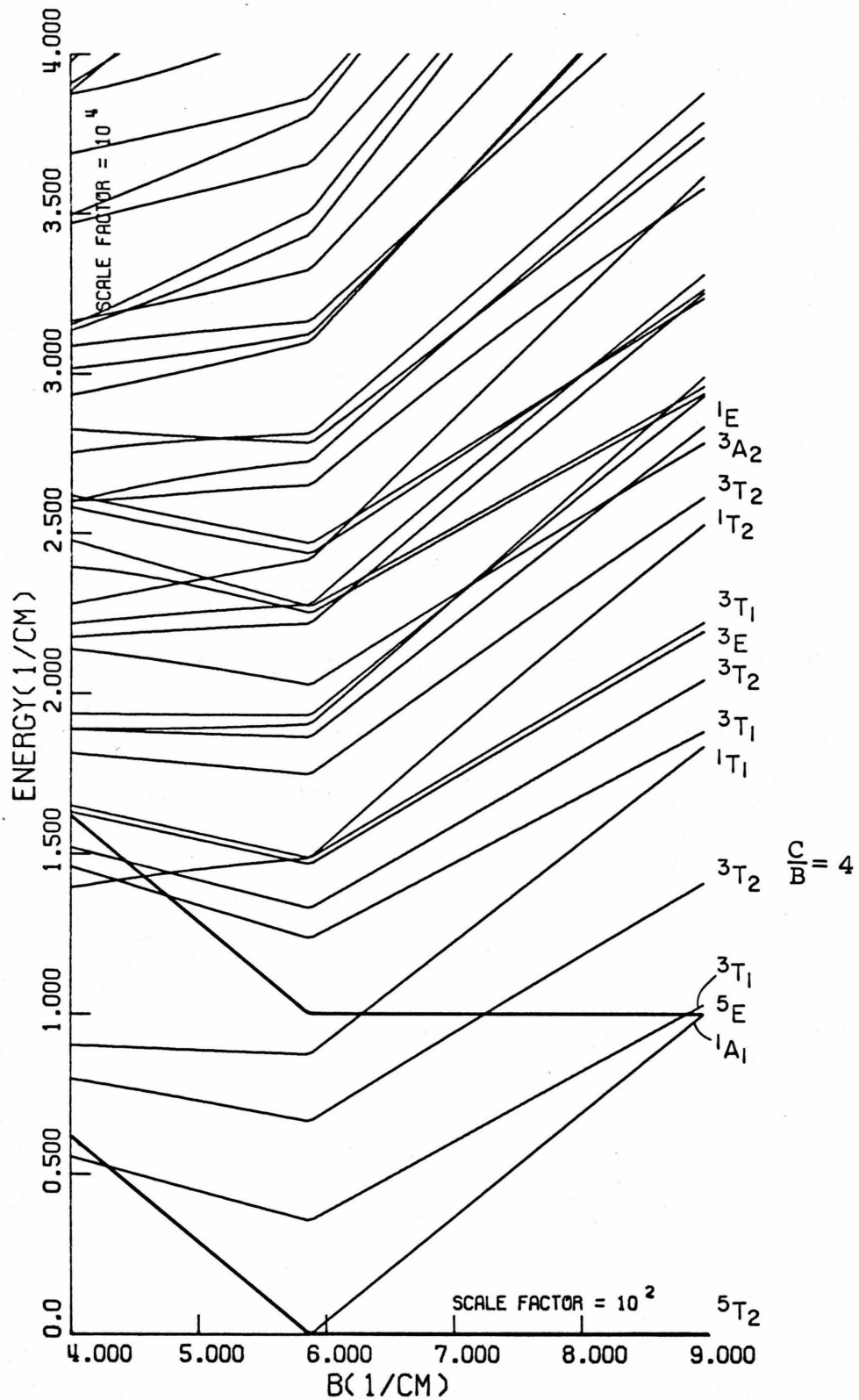
ENERGY(1/CM)
B(1/CM)
SCALE FACTOR = 10^4
SCALE FACTOR = 10^2
0.0
0.500
1.000
1.500
2.000
2.500
3.000
3.500
4.000
4.000
5.000
6.000
7.000
8.000
9.000
1E
3A2
3T2
1T2
3T1
3E
3T2
3T1
1T1
3T2
3T1
5E
1A1
5T2
C/B = 4

Figure 2

Energy of states of $Fe^{2+}$ in an octahedral field ($Dq = 1000\ cm^{-1}$) as a function of B for constant C/B. Heavy lines are quintet states. Some of the lower excited states are labelled.

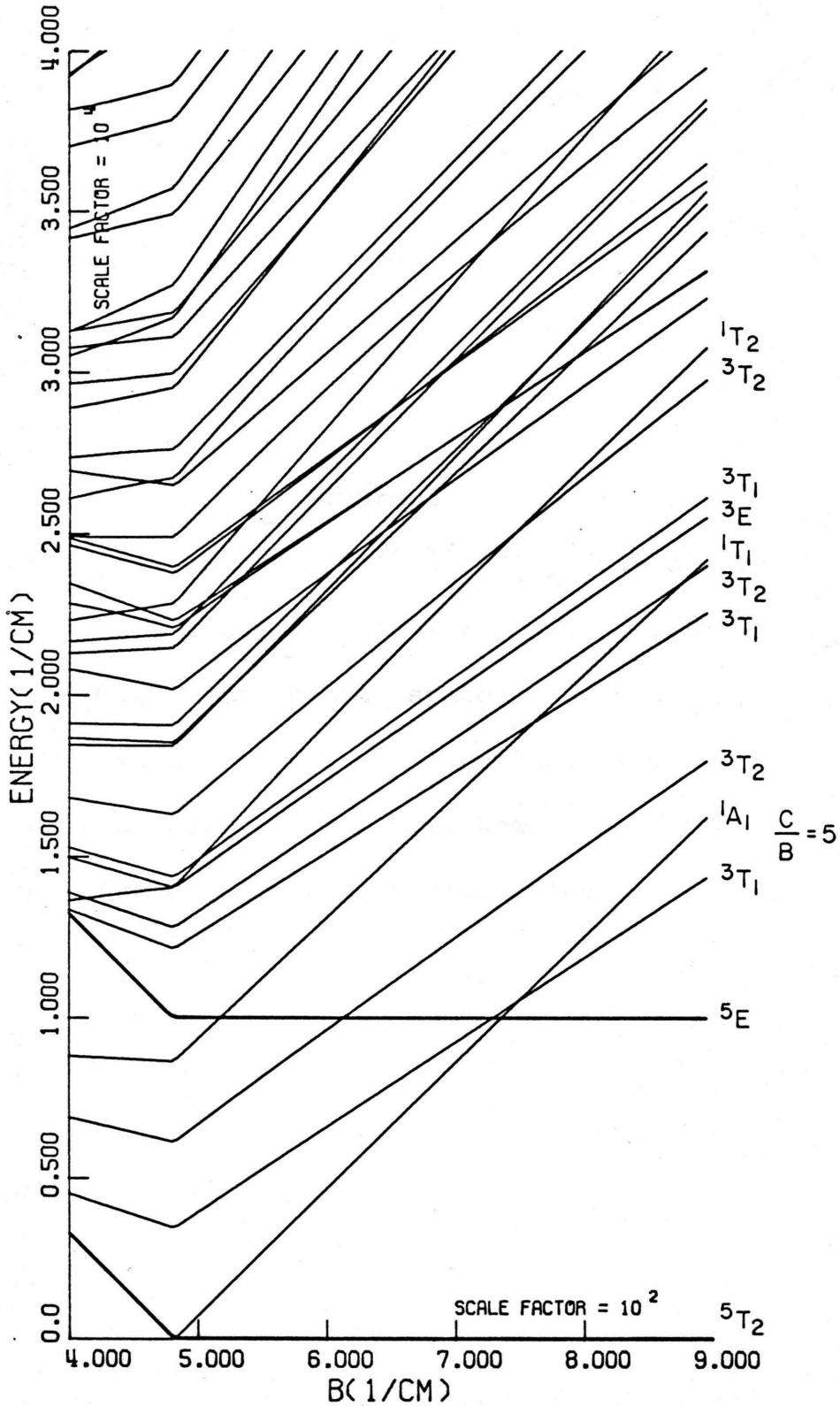
ENERGY(1/CM)
0.0
0.500
1.000
1.500
2.000
2.500
3.000
3.500
4.000
SCALE FACTOR = 10^4
4.000
5.000
6.000
7.000
8.000
9.000
B(1/CM)
SCALE FACTOR = 10^2
1T2
3T2
3T1
3E
1T1
3T2
3T1
3T2
1A1
3T1
5E
5T2
C/B = 5

Figure 3

Energy of states of $Fe^{2+}$ in a $D_{4h}$ (gillespite) field as a function of B for constant C/B. Heavy lines are quintet states. Some of the lower excited states are labelled. The one electron energy levels have been chosen to fit the observed spectrum of gillespite.

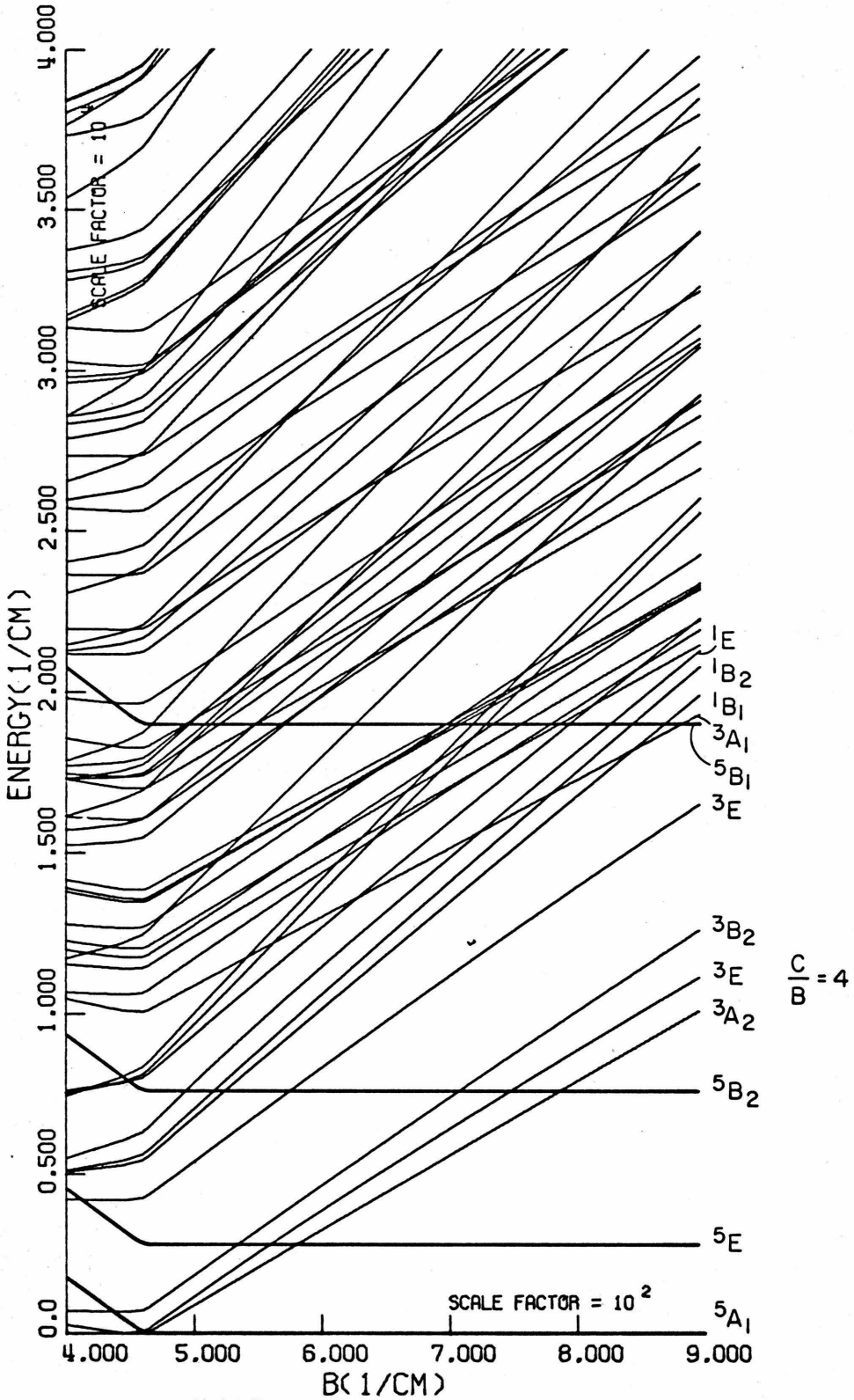
ENERGY( 1/CM )
0.0
0.500
1.000
1.500
2.000
2.500
3.000
3.500
4.000
SCALE FACTOR = 10 4
4.000
5.000
6.000
7.000
8.000
9.000
B( 1/CM )
SCALE FACTOR = 10 2
1E
1B2
1B1
3A1
5B1
3E
3B2
3E
3A2
5B2
5E
5A1
C/B = 4

Figure 4

Energy of states of $Fe^{2+}$ in a $D_{4h}$ (gillespite) field as a function of B for constant C/B. Heavy lines are quintet states. Some of the lower excited states are labelled.

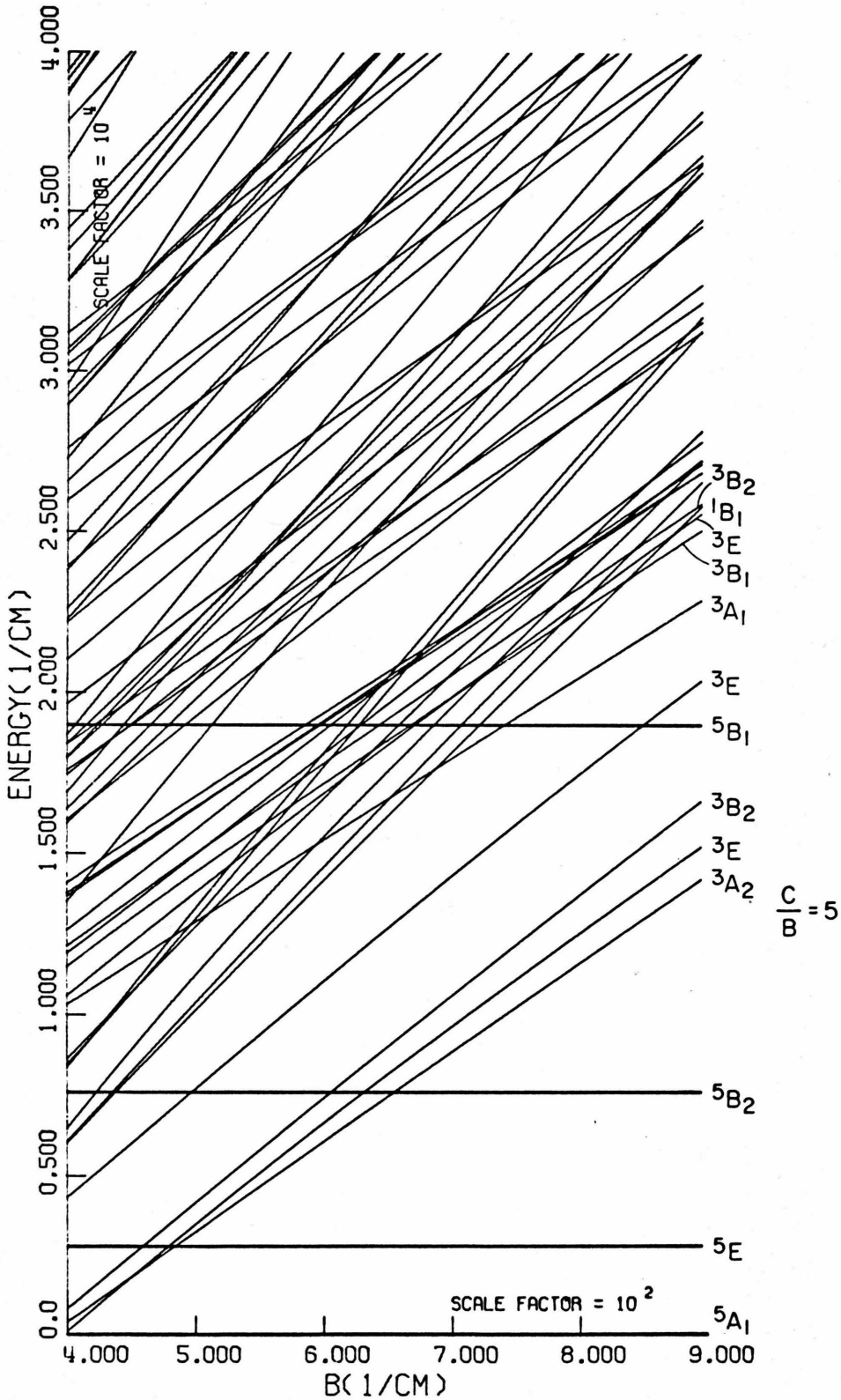
ENERGY( 1/CM )
B( 1/CM )
SCALE FACTOR = 10 4
SCALE FACTOR = 10 2
0.0
0.500
1.000
1.500
2.000
2.500
3.000
3.500
4.000
4.000
5.000
6.000
7.000
8.000
9.000
3B2
1B1
3E
3B1
3A1
3E
5B1
3B2
3E
3A2
5B2
5E
5A1
C/B = 5

Figure 5

Energy of states of $Fe^{2+}$ in a $D_{2d}$ (garnet) field as a function of B for constant C/B. Heavy lines are quintet states. Some of the lower excited states are labelled. The one electron energy levels have been chosen to fit the observed spectrum of almandine garnet.

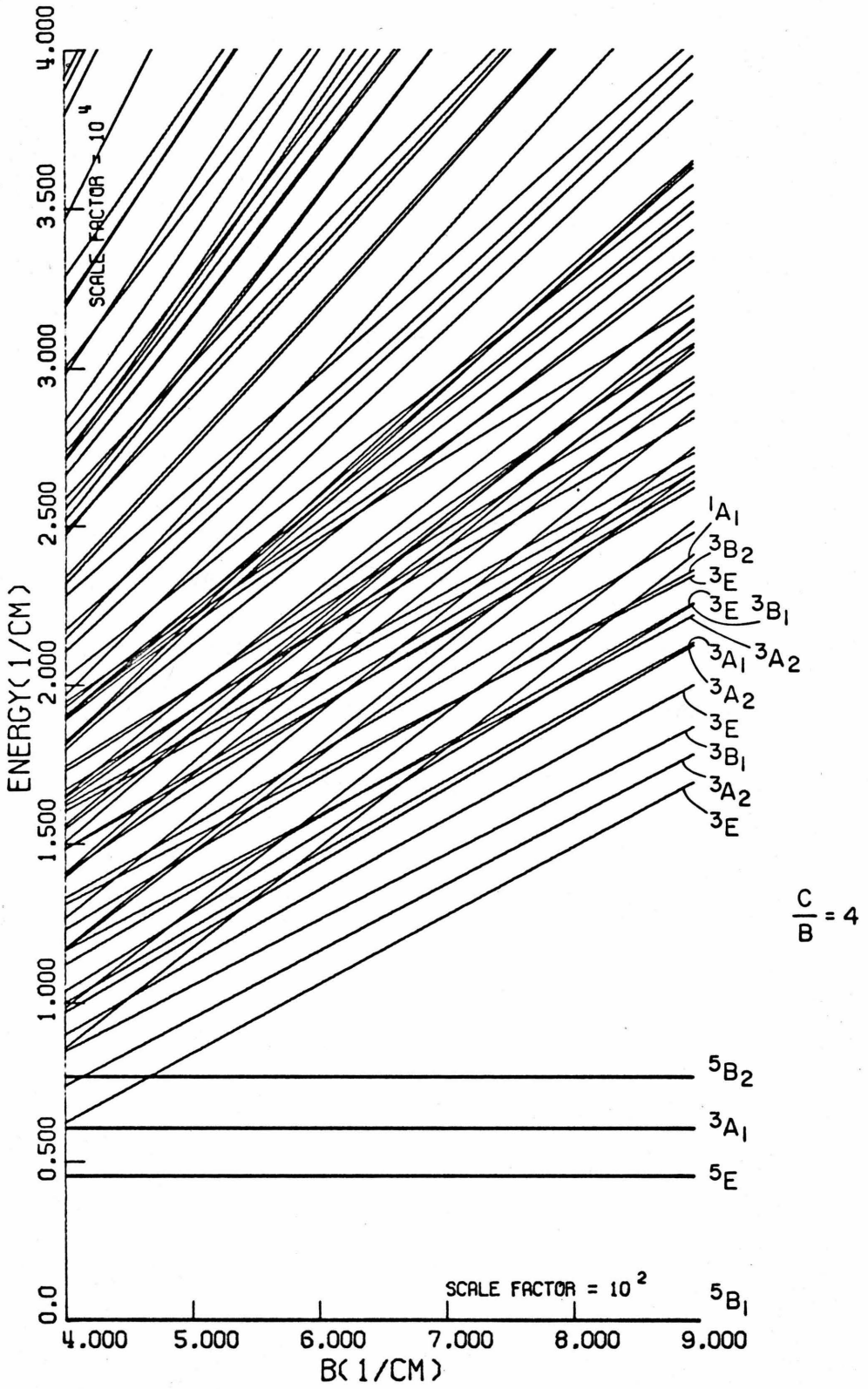
ENERGY( 1/CM )
B( 1/CM )
SCALE FACTOR = 10^4
SCALE FACTOR = 10^2
0.0
0.500
1.000
1.500
2.000
2.500
3.000
3.500
4.000
4.000
5.000
6.000
7.000
8.000
9.000
$^1A_1$
$^3B_2$
$^3E$
$^3E$ $^3B_1$
$^3A_1$ $^3A_2$
$^3A_2$
$^3E$
$^3B_1$
$^3A_2$
$^3E$
$^5B_2$
$^3A_1$
$^5E$
$^5B_1$
C/B = 4

Figure 6

Energy of states of $Fe^{2+}$ in a $D_{2d}$ (garnet) field as a function of B for constant C/B. Heavy lines are quintet states. Some of the lower excited states are labelled.

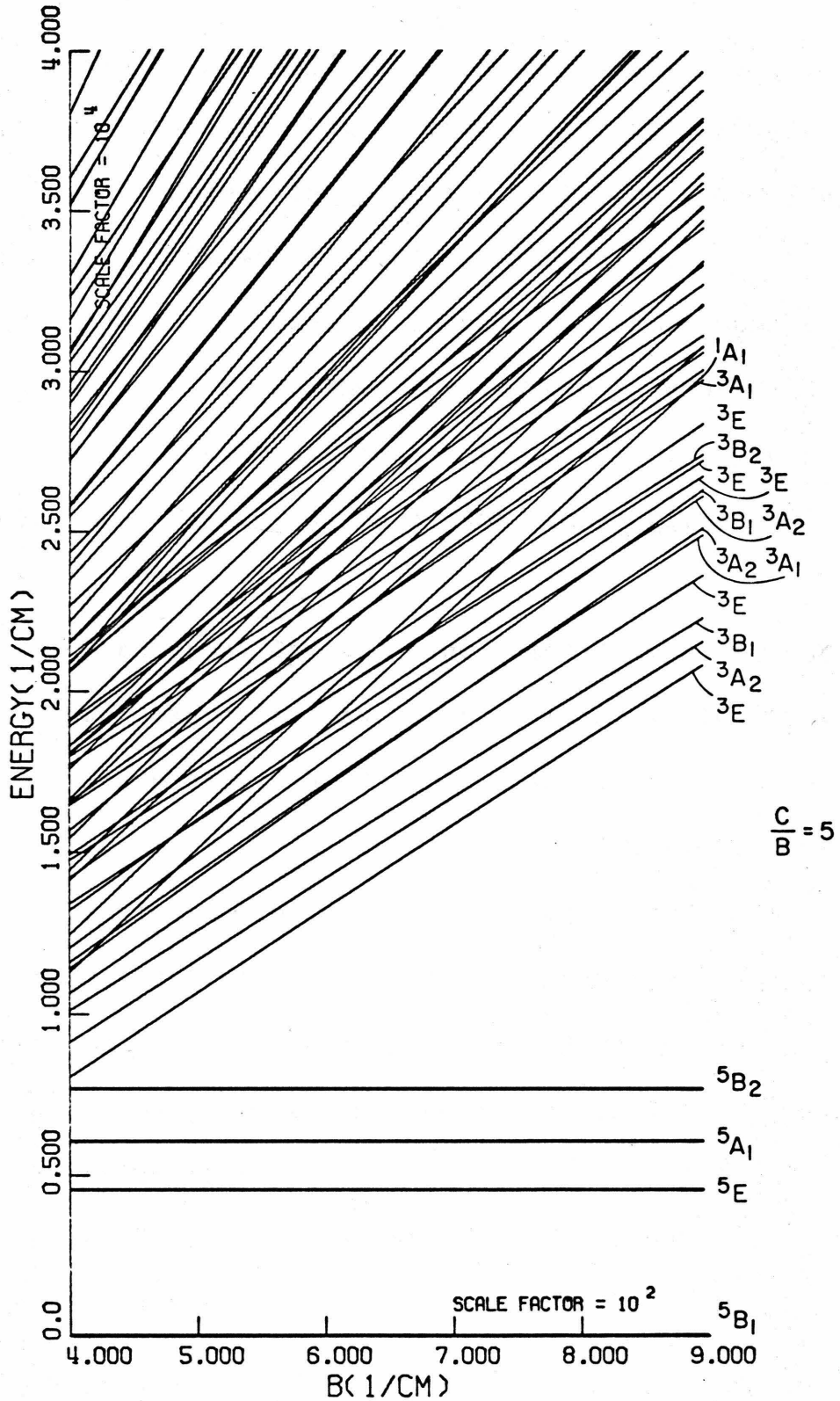
ENERGY(1/CM)
B(1/CM)
SCALE FACTOR = 10 4
SCALE FACTOR = 10 2
4.000
3.500
3.000
2.500
2.000
1.500
1.000
0.500
0.0
4.000
5.000
6.000
7.000
8.000
9.000
1A1
3A1
3E
3B2
3E 3E
3B1 3A2
3A2 3A1
3E
3B1
3A2
3E
5B2
5A1
5E
5B1
C/B = 5

## REFERENCES

(1) J. S. Griffiths, The Theory of Transition-Metal Ions. 455 pp., Cambridge Univ. Press, Cambridge (1964).

(2) C. J. Ballhausen, Introduction to Ligand Field Theory. 298 pp., McGraw-Hill, New York (1962).

(3) Y. Tanabe and S. Sugano, On the absorption spectra of complex ions. I. J. Phys. Soc. Japan 9, 753-766 (1954).

(4) J. Otsuka, Electrostatic interaction of $d^n$ systems in tetragonal fields. J. Phys. Soc. Japan 21, 596-620 (1966).

(5) M. T. Hutchings, Point-charge calculations of energy levels of magnetic ions in crystalline electric fields. Solid State Phys. 16, 227-273 (1966).

(6) R. G. Burns, M. G. Clark, and A. J. Stone, Vibronic polarization in the electronic spectra of gillespite, a mineral containing iron (II) in square-planar coordination. Inorg. Chem. 5, 1268-1272 (1966).

(7) R. G. Burns, Electronic spectra of silicate minerals: application of crystal field theory to aspect of geochemistry. Ph. D. Dissertation. Univ. Calif., Berkeley (1965).

(8) R. G. Burns, Crystal field spectra and evidence of ordering in olivine minerals. Am. Mineralog. 55, 1608-1632 (1970).

(9) P. Bloomfield, A. W. Lawson, and C. Ray, Crystal field splitting and covalent bonding in $Fe^{++}$ silicate garnets. J. Chem. Phys. 34, 749-756 (1961).

(10) J. S. Berkes, Energy Level Diagrams for Transition Metal Ions in Cubic Crystal Fields. MRL Monograph No. 2, Material Res. Lab., Penna. State Univ. (1968).

## III. ZERO PRESSURE SPECTRA OF FERROUS MINERALS

Changes in the spin multiplicity of the ground state of $Fe^{2+}$ at high pressures have been observed in complex oxides. (1) The pressures required for such transitions can be predicted if the elastic properties of the host mineral and the parameters of the crystal field, Dq, B and C, are known. (2) These parameters must be determined from observed spectra, and the last two, the Racah parameters, can only be determined from spin-forbidden transitions. Assignments of spin-forbidden transitions in the spectra of ferrous minerals and compounds are rare in the literature. (3-6)

### A. Spinel

In the course of an investigation of such bands in several silicates (vide infra) the spectra of (Mg, Fe)$Al_2O_4$ previously published by Slack (7) have been reexamined. The system is an ideal one for studying such spectra because the $Fe^{2+}$ is in the tetrahedral site. The matrix elements for d-electron wave functions in such a site have been determined (8) in terms of the crystal field parameter Dq and the Racah parameters. Furthermore, the site lacks

an inversion center which will permit considerably greater absorbances than in a centrosymmetric site.

The spectra of Slack's samples R75 and R97 are summarized in the first two columns of Table 1. In a few cases, the energies given in the table do not agree exactly with those given by Slack; these are all broad peaks on a sloping background and it is felt that the values quoted here (obtained by assigning the transition energy to the point at which a line parallel to the baseline is tangent to the spectrum) are a better estimate of the transition energies. The intense absorption near 2.5 μm (4000 $cm^{-1}$) was assigned to spin-allowed transitions of 3d electrons on $Fe^{2+}$ ions in the tetrahedral sites. Several weaker features in the visible were assigned to similar transitions on minor amounts of $Cr^{3+}$ and $Fe^{3+}$ (principally in octahedral sites). Weak absorptions near 1 μm (10,000 $cm^{-1}$) were assigned to octahedral $Fe^{2+}$ - $Fe^{3+}$ charge transfer.

There is little doubt as to the validity of the assignment of the 2.5 μm bands, especially in light of Slack *et al.*'s excellent low temperature study of them (9). However, the assignments of many of the remaining weaker bands are awkward. All of the transitions are assigned to minor

Table 1. Spectral Assignments for $(Mg,Fe)Al_2O_4$

| Slack's Assignment[a.] | | Observed Energy[b.] ($cm^{-1}$) | Present Assignment | | Calculated Energy ($cm^{-1}$) 4 bands[c.] | 7 bands[d.] |
|---|---|---|---|---|---|---|
| $Fe^{2+}$ in T | $^5E \rightarrow {}^5T_2$ | 3600, 4900 | $Fe^{2+}$ in T | $^5E \rightarrow {}^5T_2$ | 4390 | 4390 |
| $Fe^{2+}$ in O<br>$Fe^{2+}$-$Fe^{3+}$ charge transfer | | 9500<br>10800 | $Fe^{2+}$ in O | $^5T_2 \rightarrow {}^5E$ | - | - |
| $Fe^{2+}$ in O | | 14300 | $Fe^{2+}$ in T | $^5E \rightarrow {}^3T_1$ | 14290 | 14260 |
| $Cr^{3+}$ in O | $^4A_2 \rightarrow {}^4T_2$ | 18100 | $Fe^{2+}$ in T | $^5E \rightarrow {}^3T_1$ | 18130 | 18100 |
| $Fe^{3+}$ in T | $^6\Gamma \rightarrow {}^4\Gamma$ | 19400 | $Fe^{2+}$ in T | $^5E \rightarrow {}^3A_2$ | 19600 | 19590 |
| $Fe^{3+}$ in T | $^6\Gamma \rightarrow {}^4\Gamma$ | 21400 | $Fe^{2+}$ in T | $^5E \rightarrow {}^3T_1$ | 21410 | 21390 |
| $Cr^{3+}$ in O | $^4A_2 \rightarrow {}^2T_2$ | 21900 | $Fe^{2+}$ in T | $^5E \rightarrow {}^3E$ | 21830 | 21870 |
| $Cr^{3+}$ in O | $^4A_2 \rightarrow {}^4T_1$ | 26050<br>27000 | $Fe^{2+}$ in T<br>$Fe^{2+}$ in T | $^5E \rightarrow {}^3T_1$<br>$^5E \rightarrow {}^3E$ | 26000<br>27040 | 25980<br>27130 |
| $Cr^{3+}$ in O | $^4A_2 \rightarrow {}^2A_1$ | 28600 | $Fe^{2+}$ in T | $^5E \rightarrow {}^3T_2$ | 28250 | 28360 |
| Crystal field parameters | | | | Dq | 439 $cm^{-1}$ | 439 $cm^{-1}$ |
| | | | | B | 703 $cm^{-1}$ | 714 $cm^{-1}$ |
| | | | | C | 3422 $cm^{-1}$ | 3405 $cm^{-1}$ |
| Standard deviation[e.] | | | | $\sigma$ | 42 $cm^{-1}$ | 110 $cm^{-1}$ |

a. O indicates octahedral site; T indicates tetrahedral.

b. See text for discrepancy between some of these values and those of Slack (ref. 1).

c. Best fit using only peaks at 18100, 21900, 26050, and 27000 $cm^{-1}$ as constraints.

d. Best fit including peaks at 14300, 14400, and 28600 $cm^{-1}$ with half the statistical weight of those in c.

e. Does not include spin-allowed peak (4390 $cm^{-1}$).

constituents of the spinel in the nearly centrosymmetric octahedral site and many of those proposed are spin-forbidden. If one must appeal to spin-forbidden transitions to explain the spectra of these spinels, it is more reasonable to first consider such transitions for the predominant transition-metal ion. Indeed, it is shown below that every one of the visible spectral features can be assigned to a spin-forbidden (quintet to triplet) transition of $Fe^{2+}$ in tetrahedral sites in a consistent fashion.

A revised assignment of the spinel spectra is given in the third column of Table 1. Values of Dq, B and C were calculated to give a least squares fit to two sets of data. In the first set only the four sharp transitions were the energies given in the table agree with Slack's energies were used; in the second set the other peaks were also included with a statistical weight of 0.5. In both cases the spin-allowed band at about 4000 $cm^{-1}$ was not used to constrain the fit. The values of Dq, B and C are virtually identical for the two models. Furthermore, the value of Dq (439 $cm^{-1}$) is less than 2 percent lower than the value obtained from low-temperature studies of the

spin-allowed bands (9). The values of B and C are less than the free ion values of 1058 $cm^{-1}$ and 3901 $cm^{-1}$, respectively. (10) This is reasonable since bonding will tend to reduce electron repulsion. The ratio C/B is near that of several other ferrous minerals described below.

The value of Dq in the spinel structure deserves some comment. Based on the model of Chapter II, it is predicted that

$$r^5(O_h)\ Dq(O_h) = -\frac{9}{4}\, r^5(T_d)\ Dq(T_d).$$

In many oxides (5) $r(O_h) \sim 2.15$ Å and $Dq(O_h) \sim 1000\ cm^{-1}$. So for $r(T_d) = 1.81$ Å as in spinel (9) we expect $Dq(T_d)$ to be about 1000 $cm^{-1}$. Such a large deviation of experiment from theory indicates that our assumption of pure ionic bonding may be incorrect. It is likely that in the spinels there is appreciable $\pi$-bonding between the ligand $2p(\pi)$ orbitals and the $Fe^{2+}$ $e_g$ orbitals which effectively raises the energy of the latter by almost 6000 $cm^{-1}$. Such a large amount of mixing of ligand orbitals with $e_g$ orbitals will make the detailed analysis of Slack et al. (9) uncertain as regard to spin-orbit coupling. However, as stated in Chapter II, this should decrease the Racah coefficients but

such an effect is not apparent. It is likely that the assumptions leading to Equation (6) in Chapter II are not valid for such short interatomic separations.

It is interesting to note that tetrahedral $Fe^{2+}$ does not have any spin-forbidden transitions in the vicinity of 1 μm, thus supporting Slack's conclusion that there is some octahedral $Fe^{2+}$ in these specimens. Note however that we assign the peak at 10,800 $cm^{-1}$ to this site rather than the one at 14,300 $cm^{-1}$. This reduces the Jahn-Teller splitting in the $^5E$ state of octahedral $Fe^{2+}$ to 1300 $cm^{-1}$, a value nearer to that observed in other materials (11) than Slack's value of 3400 $cm^{-1}$.

B. Garnets

The spectra of several garnets are reported here: a rhodolite, two spessartines, an andradite, and a hessonite. Only the former is directly of interest to the purpose of this work, the evaluation of the behavior of $Fe^{2+}$ in the lower mantle — the others were studied so that the contributions of $Fe^{3+}$ and $Mn^{2+}$ to the rhodolite spectra could be determined. The compositions of the garnets (as determined by electron microprobe) are given in Table 2 and the observed spectra are shown in Figures 1

TABLE 2 CHEMICAL COMPOSITION OF SAMPLES

| MINERAL | COMPOSITION |
|---|---|
| Dementoid | $(Ca_{3.03}Mg_{.01})Fe^{3+}_{1.97}Si_{2.98}O_{12}$ |
| Hessonite | $(Ca_{2.86}Mn_{.01}Fe^{2+}_{.11})\ Al_{1.91}Fe^{3+}_{.09}\ Si_{3.01}O_{12}$ |
| Spessartine | $(Mn_{2.89}Fe^{2+}_{.07}Ca_{.06})\ Al_{2.02}Si_{2.96}O_{12}$ |
| Almandine-Spessartine | $(Fe^{2+}_{1.61}Mn_{1.36}Ca_{0.03})\ Al_{1.99}Si_{2.98}O_{12}$ |
| Rhodolite | $(Mg^{2+}_{1.83}Fe^{2+}_{.99}Ca_{.14}Mn_{.04})\ Al_{2.01}Si_{2.99}O_{12}$ |
| Gillespite | $Ba_{.98}Na_{.01}Fe_{.97}Mg_{.01}Si_4O_{10}$ |
| Tephroite | $Mn_{1.85}Mg_{.09}Fe_{.02}Ca_{.04}SiO_4$ |
| Peridot | $(Mg_{1.76}Fe^{2+}_{.22}Mn_{.002}Ca_{.003})\ Si_{1.005}O_4$ |

Figure 1

Spectra of ferric iron silicate garnets:

a) dementoid, .455 mm thick and b)hessonite.

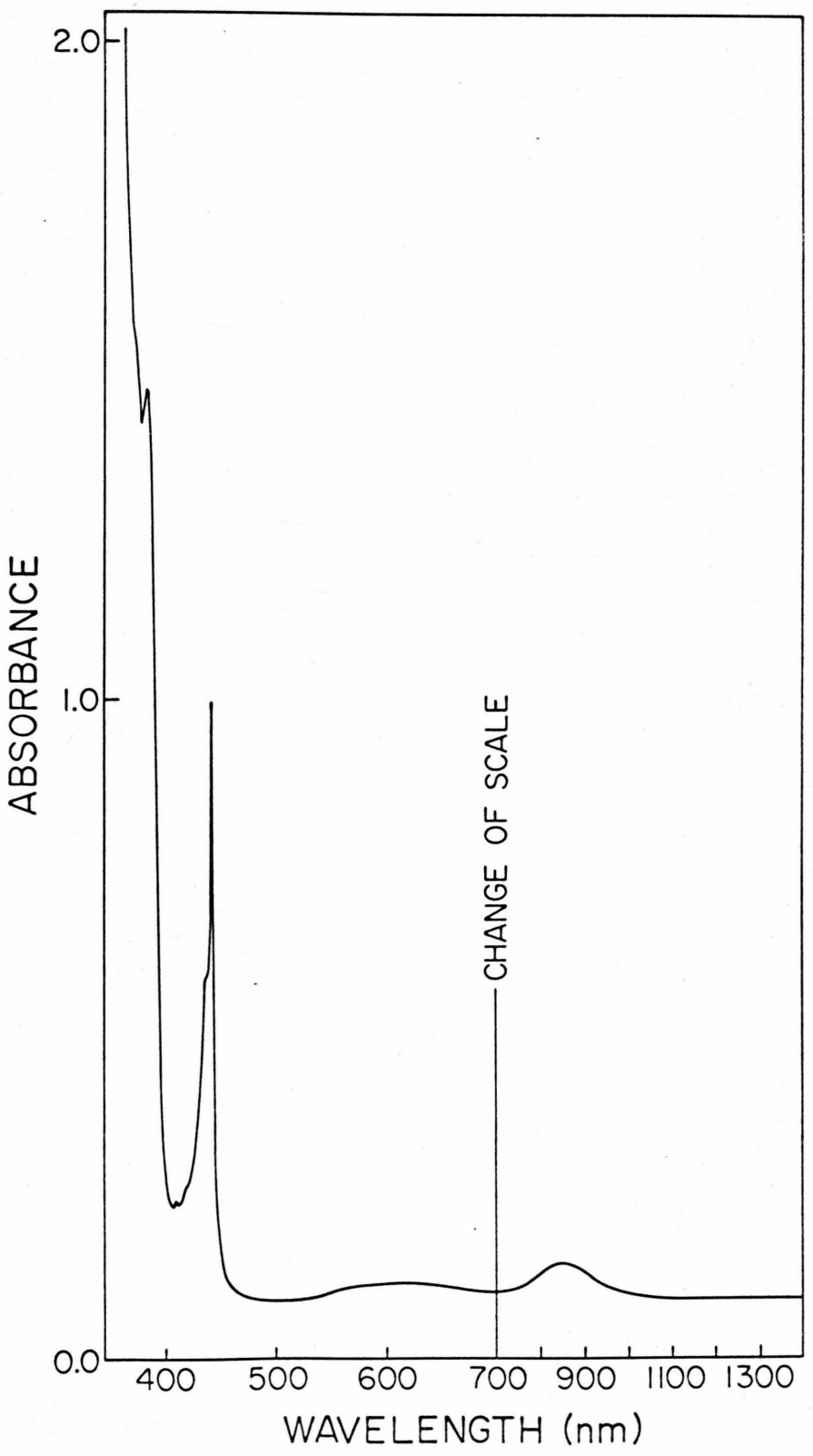
2.0
1.0
0.0
ABSORBANCE
CHANGE OF SCALE
400
500
600
700
900
1100
1300
WAVELENGTH (nm)

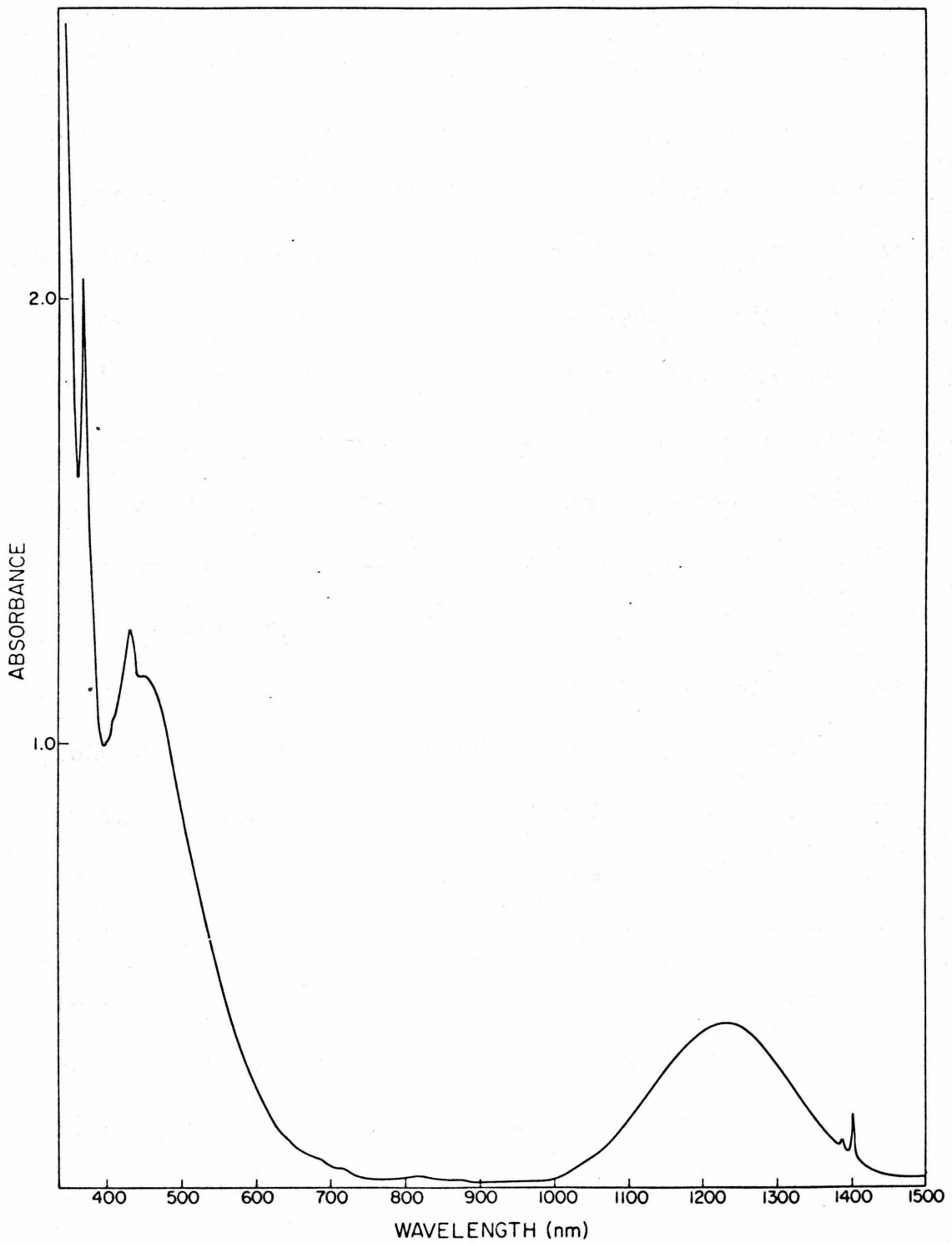
ABSORBANCE
2.0
1.0
400
500
600
700
800
900
1000
1100
1200
1300
1400
1500
WAVELENGTH (nm)

through 3. All spectra were measured on a Cary 17 spectrophotometer, by either the author or Professor George Rossman, with the exception of the low temperature spectra, which were measured by Charles Cowman.

The spectra of silicate garnets have been studied for many years by several authors. For a recent compilation of these studies, see Table 2 of Slack and Chrenko (12). For all garnets with even small amounts of almandine ($Fe_3Al_2Si_3O_{12}$) there are three broad bands in the infrared. These are universally assigned to spin-allowed electronic transitions among the $Fe^{2+}$ quintets separated due to effects of the crystal field. In more almandine-rich garnets there are also several weaker absorptions in the visible region. Since 1928 most investigators have followed the lead of Weigel and Ufer (13), assigning these features to transitions of impurities such as $Cr^{3+}$, $Fe^{3+}$ and $Mn^{2+}$. Only Anderson (14) and Manning (15) have expressed doubt about these assignments. Both of these authors preferred to attribute these bands to spin-forbidden transitions of $Fe^{2+}$, the major transition metal ion, rather than to minor elements; they did not however, make any specific assignments.

Figure 2

Spectra of manganous silicate garnets: a) spessartine, .69 mm thick and b) spessartine-almandine ~.7 mm thick.

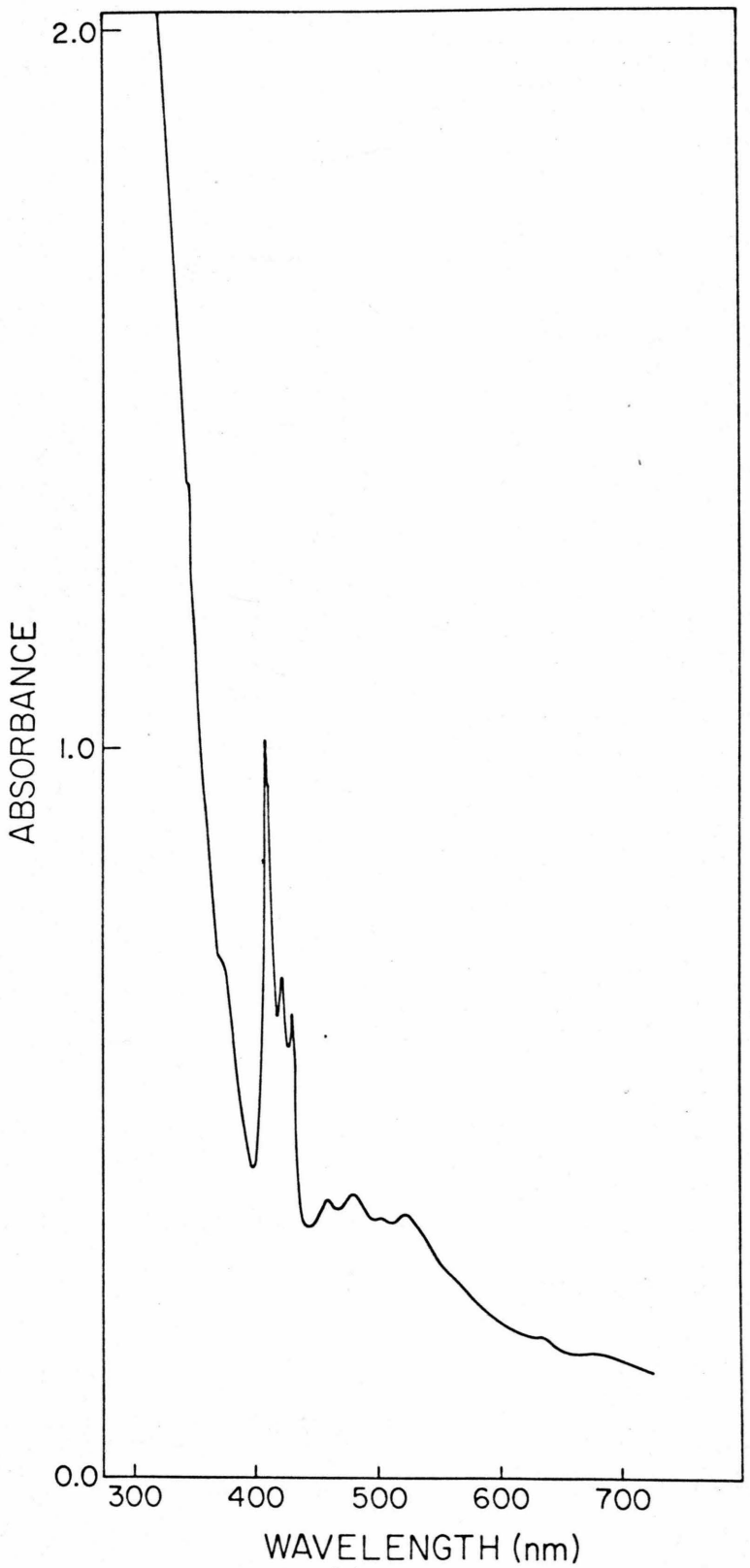
2.0
1.0
0.0
ABSORBANCE
300
400
500
600
700
WAVELENGTH (nm)

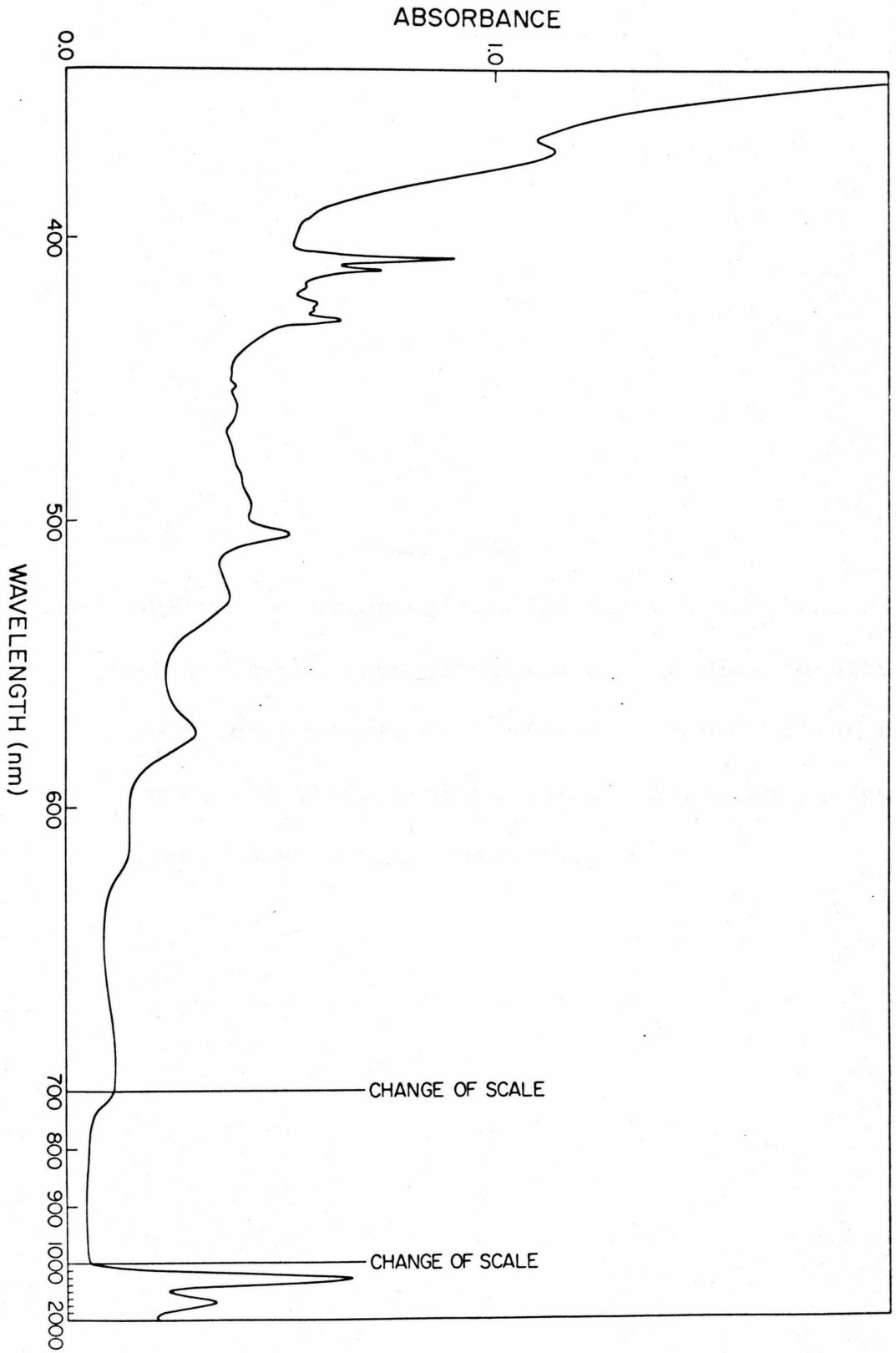
ABSORBANCE
0.0
1.0
400
500
600
700
800
900
1000
2000
WAVELENGTH (nm)
CHANGE OF SCALE
CHANGE OF SCALE

Figure 3

Spectra of pyrope-almandine garnet, var. rhodolite. a) Infrared, room temperature. b) Visible-ultraviolet, room temperature. c) Infrared, liquid helium temperature. d) Visible-ultraviolet, liquid helium temperature. Sample thickness ~1.2 mm.

(a)

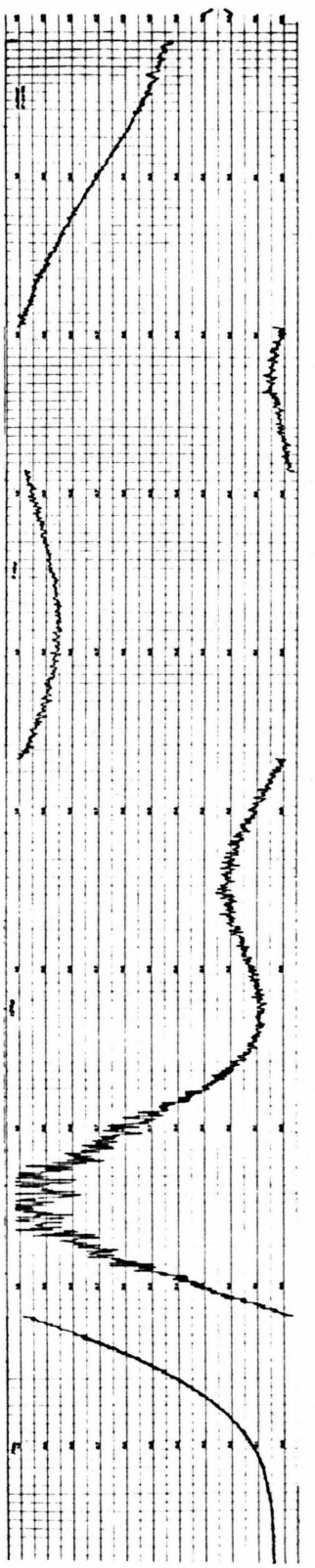

(b)

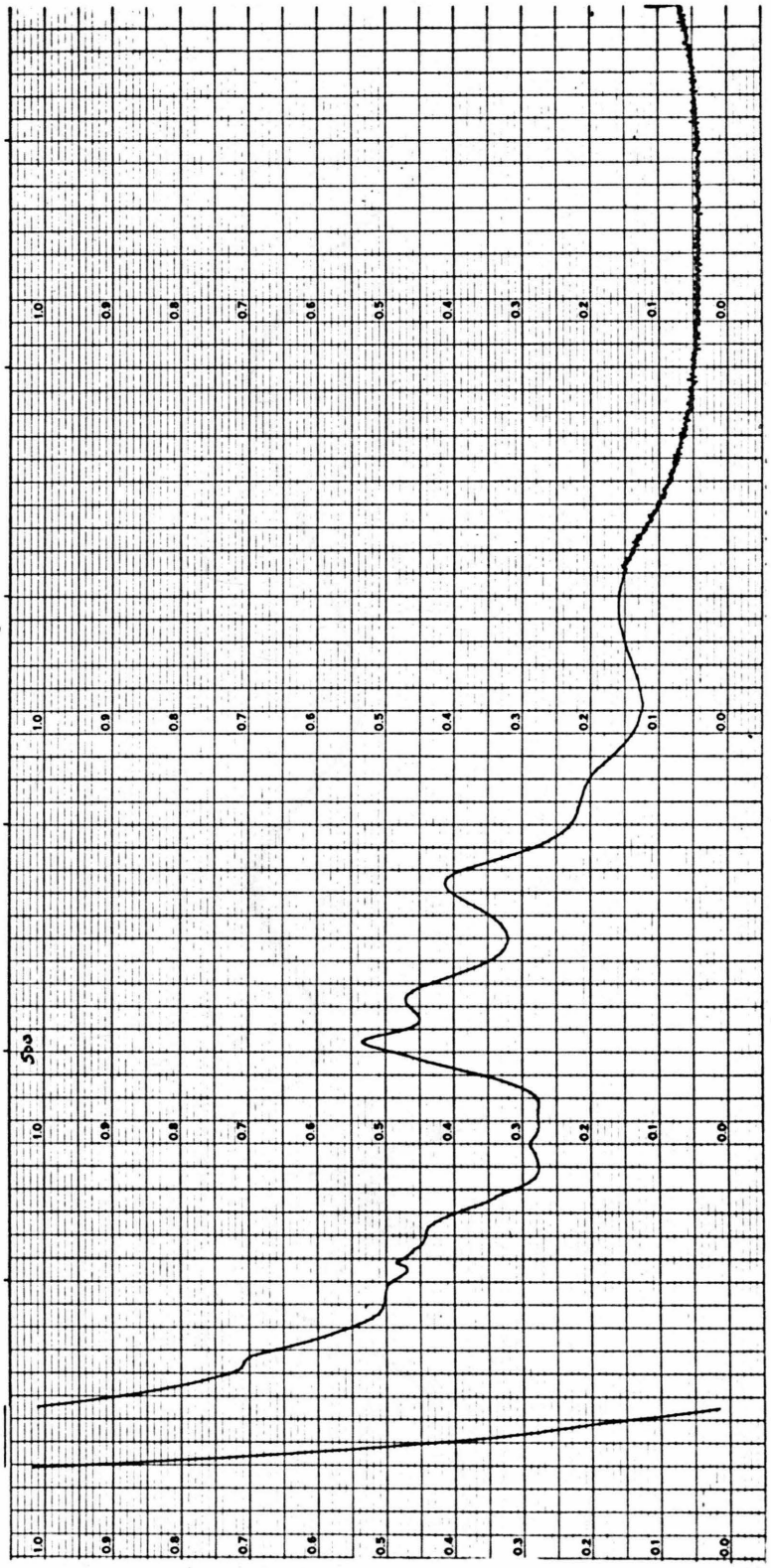

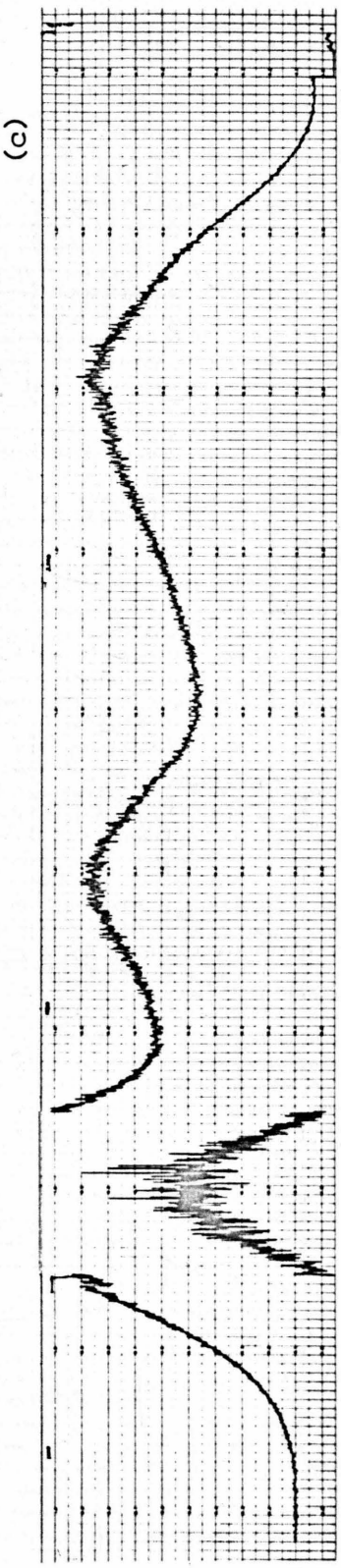
(c)

(d)

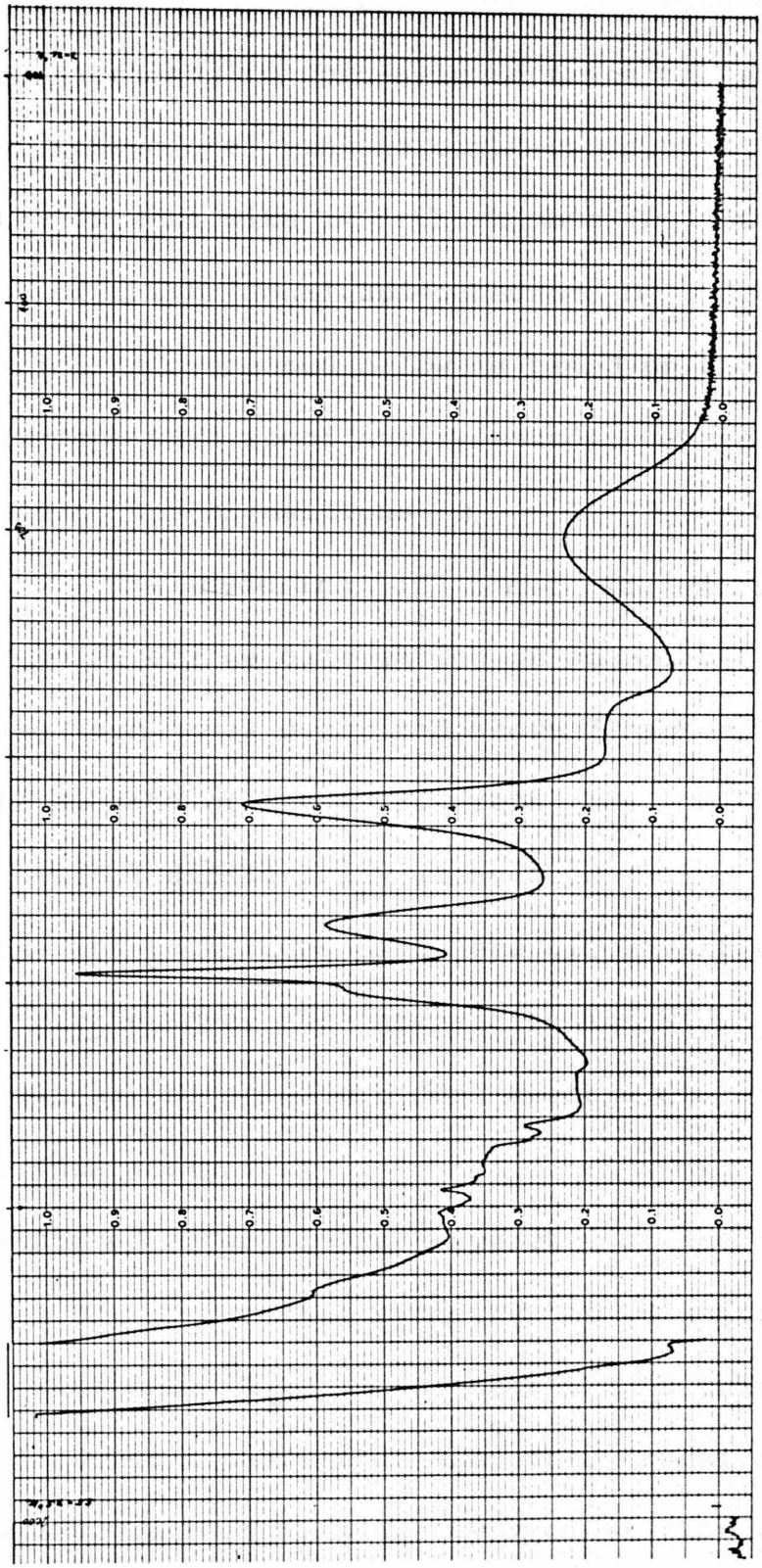

The infrared bands observed here, following earlier workers, are assigned to spin-allowed transitions among the 3d electrons of $Fe^{2+}$ in the eight-coordinate site. The symmetry of this site is orthorhombic ($D_2$) but is very nearly that of the trigonal dodecahedron ($D_{2d}$) (16). The analysis which is presented below is based on the $D_{2d}$ symmetry (except when specifically noted). These bands are assigned to the transitions $^5B_1 \longrightarrow {}^5E$, $^5B_1 \longrightarrow {}^5A_1$, and $^5B_1 \longrightarrow {}^5B_2$. The ordering of these states is based on a point charge calculation of one-electron energy levels using techniques described above (Chapter II) and the structural data of Novak and Gibbs (16). Although there are several difficulties associated with point charge calculations the techniques used here circumvent the worst of these. Furthermore, the intensities and widths of the bands as well as the spin-forbidden spectra discussed below do support this assignment.

As mentioned above the real symmetry of the $Fe^{2+}$ site in garnet is $D_2$. Under this symmetry the $^5E$ state of $D_{2d}$ symmetry splits into $^5B_2 + {}^5B_3$ so that the $^5E$ transitions should be somewhat broader than the other transitions. Indeed the 2200 nm band is slightly broader than the others.

Furthermore, under the selection rules of $D_2$ the transition (in $D_{2d}$ terminology) $^5B_1 \longrightarrow {}^5A_1$ is forbidden and this is the weakest of the three bands. None of the above arguments by itself justifies the assignments given, but the combination permits some confidence.

In the visible and ultraviolet region of the spectra let us first consider the dementoid and hessonite. Both of these minerals have octahedral $Fe^{3+}$ as their dominant transition metal. Ferric iron has no spin-allowed electronic transitions so we should expect the absorption features to be fairly weak. Both spectra show absorption features near 440 nm — sharp in demantoid and broader in hessonite. In the hessonite there is a distinct peak at about 370 nm while in demantoid there is only a shoulder and a sharp peak at 383 nm. It is suggested that the features at 440 nm and 383 nm are due to octahedral $Fe^{3+}$ and that smaller amounts of $Mn^{2+}$ in the non-centrosymmetric $D_{2d}$ dominate the spectra of andradite and hessonite. A complete assignment of these spectra is given in Table 3 along with the inferred values of Dq, B and C.

Next, consider the spessartine spectra. The most abundant transition metal in these specimens is dodecahedral

TABLE 3 SPECTRA OF FERRIC GARNETS

| DEMENTOID | | | HESSONITE | | ANDRADITE | | ASSIGNMENT |
|---|---|---|---|---|---|---|---|
| $\lambda$(nm) | $E_{obs}(cm^{-1})$ | $E_{calc}(cm^{-1})$ | $\lambda$(nm) | $E_{obs}(cm^{-1})$ | $\lambda$(nm) | $E_{obs}(cm^{-1})$ | |
| 373 | 26810 | | 368 | 27170 | 373 | 26810 | $Mn^{2+}$ |
| 383 | 26110 | 25986 | 385 | 25970 | | | $^6A_1 \rightarrow {}^4T_2$ |
| 408.5 | 24480 | | 410 | 24390 | 410 | 24390 | $Mn^{2+}$ |
| 418 | 23920 | | | | | | $Mn^{2+}$ |
| 434 | 23070 | | 433 | 22780 | | | $Mn^{2+}$ |
| 440 | 22730 | 23180 | | | 438 | 22830 | $^6A_1 \rightarrow {}^4A_1, {}^4E$ |
| | | | 450 | 22220 | | | $Mn^{2+}$ |
| | | | 470 | 21280 | 470 | 21280 | $Mn^{2+}$ |
| 596 | 16810 | 16743 | | | | | $^6A_1 \rightarrow {}^4T_2$ |
| 855 | 11700 | 11767 | 815 | 12290 | | | $^6A_1 \rightarrow {}^4T_1$ |

Dq = 1381 $cm^{-1}$ B = 774 $cm^{-1}$ C = 3089 $cm^{-1}$
Standard deviation of fit for demantoid = 136 $cm^{-1}$

$Mn^{2+}$ which is isoelectronic with $Fe^{3+}$ and likewise has no spin-allowed bands. However, since the dodecahedral site lacks an inversion center, we can expect stronger absorptions than in the case of $Fe^{3+}$. Although some of the bands and shoulders are assigned to $Fe^{2+}$ spin-forbidden transitions, the most prominent are due to $Mn^{2+}$ (see Table 4 for complete assignments). Because of the low symmetry of the dodecahedral site ($D_2$, nearly $D_{2d}$) the $^4A_1$, $^4E$ band usually seen at 410 nm in $Mn^{2+}$ compounds (17) is split into three bands at 408 nm, 422 nm and 431 nm. The $^4T_2$ band at 450 nm in most minerals (17) is split into two bands at 461 nm and 482 nm. These bands are much weaker than the 408-431 nm group (less than 0.1 as intense). Finally, the $^4T_1$ absorption is virtually unaffected at 535 nm and has roughly the same intensity as the 460-480 group.

Having determined the positions of $Fe^{3+}$ and $Mn^{2+}$ absorptions in garnets where they are major constituents, let us now turn to the analysis of the rhodolite where they are minor components, and $Fe^{2+}$ is the dominant transition metal. This spectrum is much more complicated than the others, especially at liquid helium temperatures. Most of the features in the visible portion of the spectrum

TABLE 4 SPECTRA OF MANGANOUS GARNETS

| AMELIA SPESSARTINE | | | SPESSARTINE-ALMANDINE | | ASSIGNMENT |
|---|---|---|---|---|---|
| $\lambda$(nm) | $E_{obs}$($cm^{-1}$) | $E_{calc}^{a}$($cm^{-1}$) | $\lambda$(nm) | $E_{obs}$($cm^{-1}$) | |
| 345 | 28990 | 28441 | | | $^6A_1 \rightarrow {}^4E$ |
| 351 | 28490 | | | | |
| 376 | 26760 | 26762 | 373 | 26810 | $^6A_1 \rightarrow {}^4T_2$ |
| | | | 408 | 24510 | |
| 408 | 24510 | | 412 | 24270 | |
| | | | 418 | 23920 | |
| 422 | 23700 | 23870 | 423 | 23640 | $^6A_1 \rightarrow {}^4A_1, {}^4E$ |
| | | | 427 | 23420 | |
| 431 | 23200 | | 429 | 23310 | |
| | | | 453 | 22080 | |
| 461 | 21690 | 21628 | 461 | 21690 | $^6A_1 \rightarrow {}^4T_2 \begin{matrix} \nearrow {}^4E \\ \searrow {}^4A_1 \end{matrix}$ |
| 482 | 20750 | | 485 (?) | 20620 | |
| | | | 493 | 20280 | |
| 505 | 19800 | | 505 | 19800 | $Fe^{2+}$ |
| 535 | 18690 | 18482 | 528 | 18940 | $Fe^{2+}$ and $Mn^{2+}$: $^6A_1 \rightarrow {}^4T_1$ |
| 572 | 17480 | | 574 | 17420 | |
| | | | 603 | 16580 | |
| 637 | 15700 | | 616 | 16230 | $Fe^{2+}$ |
| 672 | 14880 | | | | |
| 710 | 14080 | | 694 | 14410 | |

Dq = 786 $cm^{-1}$ B = 653 $cm^{-1}$ C = 3468 $cm^{-1}$

Standard deviation of fit for spessartine = 220 $cm^{-1}$

a. Grouping bands as shown and using $O_h$ symmetry.

are attributable to spin-forbidden transitions of dodecahedral $Fe^{2+}$ although some bands are attributed to $Mn^{2+}$ and $Fe^{3+}$. Indeed, using matrix elements of $D_{2d}$ symmetry (18) it is possible to fit the observed spectrum exceedingly well. Using a least squares technique* to optimize the fit to all but four of eighteen bands, B and C are determined to be 638 $cm^{-1}$ and 3245 $cm^{-1}$, respectively. The observed and calculated transitions are listed in Table 5.

The primary effort in fitting the observed spectrum was directed toward the six strongest peaks between 14,000 $cm^{-1}$ and 21,000 $cm^{-1}$. The initial assignment of bands to electronic transitions was done with the aid of energy level diagrams similar to Figures 5 and 6 in Chapter II. The agreement there is very good. As a result of such a fit it was found that almost all of the observed bands should be assigned to spin-forbidden transitions on $Fe^{2+}$. The calculated energies in Table 5 are the results

---

* A computer program for $D_{2d}$, $D_4$, $D_{4h}$ and $C_{4v}$ symmetries was adapted from a program written by J. C. Thibeault for $O_h$ and $T_d$ symmetries. This latter program was used in analysis of the olivine data discussed in a later section.

TABLE 5 SPECTRUM OF RHODOLITE GARNET

| WAVELENGTH λ(nm) | ENERGY ($cm^{-1}$) | EXCITED STATE | ENERGY ($cm^{-1}$) CALCULATED[a] | DIFFERENCE[b] | NOTES |
|---|---|---|---|---|---|
| 2200 | 4545 | $^5E$ | | | |
| 1650 | 6060 | $^5A_1$ | | | |
| 1300 | 7690 | $^5B_2$ | | | |
| 698 | 14325 | $^3E$ | 14456 | 131 | |
| 620 | 16130 | $^3B_1$ | 16173 | 43 | |
| 579 | 17270 | $^3E$ | 17176 | - 94 | |
| 526 | 19011 | $^3B_1$ | 19094 | 83 | |
| 504 | 19840 | $^3A_2$ | 19696 | 144 | |
| 496 | 20160 | $^3E$ | 20061 | 98 | |
| 460 | 21740 | $^3E$ | | | $Mn^{2+}$: $^6A_1 \rightarrow {}^4T_2$ |
| 451 | 22175 | | | | $Mn^{2+}$: $^6A_1 \rightarrow {}^4T_2$ (?) |
| 436 | 22935 | $^3B_1$ | | | $Fe^{3+}$: $^6A_1 \rightarrow {}^4A_1$, $^4E$; $Mn^{2+}$: $^6A_1 \rightarrow {}^4A_1$, $^4E$ |
| 427 | 23420 | $^3E$ | 23531 | 111 | |
| 420 | 23810 | | | | $Mn^{2+}$: $^6A_1 \rightarrow {}^4A_1$, $^4E$ |

a. $B = 629\ cm^{-1}$, $C = 3242\ cm^{-1}$, spin allowed bands as input. Assuming pure $D_{2d}$ symmetry.

b. Standard deviation for $Fe^{2+}$ bands is $92\ cm^{-1}$.

TABLE 5 SPECTRUM OF RHODOLITE GARNET

| WAVELENGTH λ(nm) | ENERGY ($cm^{-1}$) | EXCITED STATE | ENERGY ($cm^{-1}$) CALCULATED[a.] | DIFFERENCE[b.] | NOTES |
|---|---|---|---|---|---|
| 413 | 24215 | $^3B_2$ | 24131 | 84 | |
| 408 | 24510 | $^3A_2$ | | | $Mn^{2+}$: $^6A_1 \rightarrow {}^4A_1$, $^4E$ |
| 397 | 25190 | $^3E$ | 25218 | 92 | |
| 392 | 25510 | $^3A_1$ | 25415 | 95 | |
| 363 | 27550 | | | | $Mn^{2+}$: $^6A_1 \rightarrow {}^4T_2$ (?) |
| 345 | 28985 | $^3E$ | 28980 | - 5 | $Mn^{2+}$: $^6A_1 \rightarrow {}^4E$ |
| 338 | 29585 | $^3B_2$ | 29591 | 6 | |

a. B = 629 $cm^{-1}$, C = 3242 $cm^{-1}$, spin allowed bands as input. Assuming pure $D_{2d}$ symmetry.

b. Standard deviation for $Fe^{2+}$ bands is 92 $cm^{-1}$.

of a second calculation taking the complete assignments into account. The standard deviation of the resulting fit (92 $cm^{-1}$) is excellent in view of the complexity of the system considered and the fact that the actual symmetry is lower than that used in the calculations. Only three bands (22175, 23810, and 27550 $cm^{-1}$) are unassigned in this scheme. These bands together with two which could be assigned as well to $Fe^{2+}$ (24510 and 28985 $cm^{-1}$) are attributed to $Mn^{2+}$ and $Fe^{3+}$ as shown in Table 5.

C. Gillespite

The spectrum of gillespite ($BaFeSi_4O_{10}$) has been reported by Burns (5). Spin-allowed transitions were observed at 20,000 $cm^{-1}$ and 8000 $cm^{-1}$ and a third transition near 2800 $cm^{-1}$ was inferred from analysis of the spectrum of the $Cu^{2+}$ analog of gillespite (19). The spectra of a sample of gillespite from Mariposa County, California at 300° K and 6° K are shown in Figure 4. The specimen was 0.75 mm thick, mounted on a fused quartz slide with the c-axis approximately in the direction of propagation. The results of an electron microprobe analysis of the sample appear in Table 2. In addition to

Figure 4

Spectra of gillespite, $BaFeSi_4O_{10}$. a) liquid helium temperature and b) room temperature. Sample thickness ~ .7 mm.

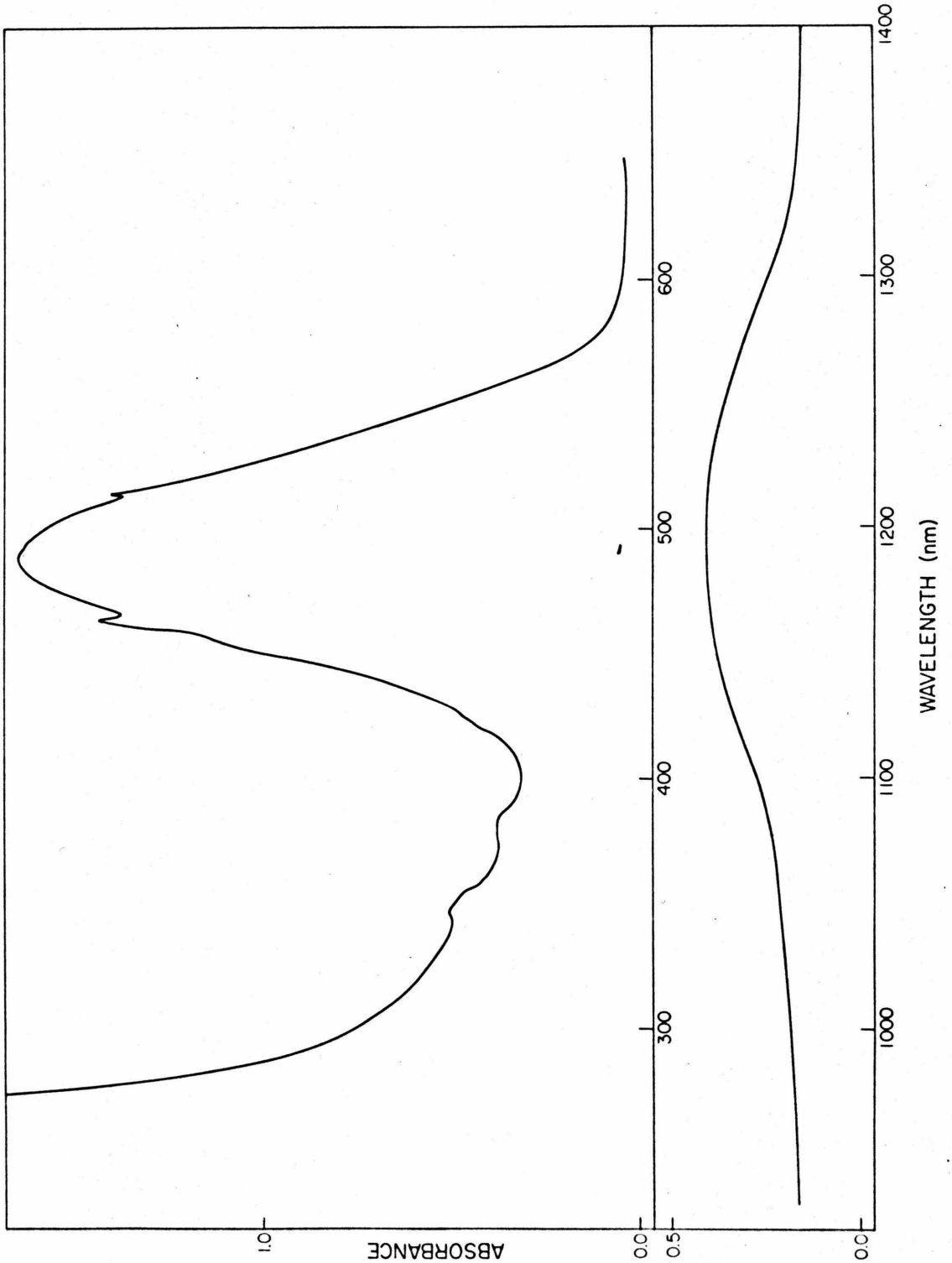
ABSORBANCE
1.0
0.0
0.5
0.0
300
400
500
600
1000
1100
1200
1300
1400
WAVELENGTH (nm)

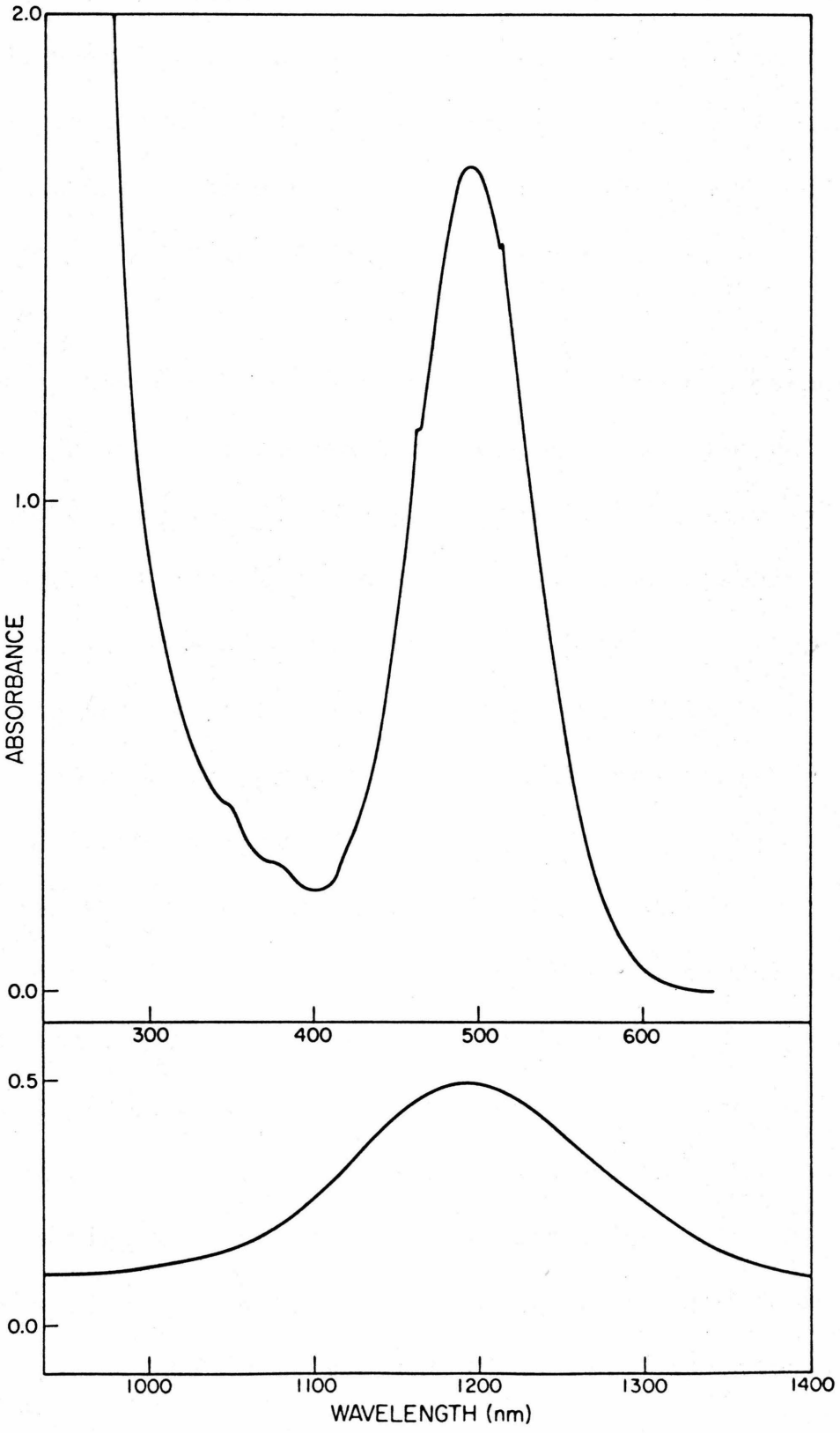
2.0
1.0
0.0
ABSORBANCE
300
400
500
600
0.5
0.0
1000
1100
1200
1300
1400
WAVELENGTH (nm)

the two peaks reported by Burns several very weak peaks are observed near 20,000 to 30,000 $cm^{-1}$ at both high and low temperatures. These bands are attributed to spin-forbidden electronic transitions on the $Fe^{2+}$ in square planar coordination (the structure of gillespite was reported by Wainwright (20)).

Using the procedure described in fitting the garnet spectrum the spin-forbidden bands are assigned and values for B and C determined. The positions of the peaks and the assignments are shown in Table 6. The values of B and C obtained are B = 582 $cm^{-1}$ and C = 2601 $cm^{-1}$ with C/B = 4.47. The values of B and C are very low. This is exactly the behavior predicted for small interatomic distances in Chapter II.

Given the values of B and C a modified Tanabe-Sugano diagram can be constructed for gillespite. Such diagram is shown in Figure 5 where the ratios of the separations of one electron energies are kept constant and the magnitude $1/2(^5A_{1g} - {}^5B_{1g})$ or Y is used as the abscissa. It is interesting to note that only a little increase in Y is necessary in order to change the ground state from $^5A_{1g}$ to $^3E_g$. This is consistent with the experimental

TABLE 6. SPECTRUM OF GILLESPITE AT 6°K

| Wavelength λ (nm) | Energy ($cm^{-1}$) | Excited State | Energy ($cm^{-1}$) a. Calculated | b. Difference | |
|---|---|---|---|---|---|
| | | $^3A_2$ | 2500 | | lowest triplet |
| | | $^5E$ | 2800 | | assumed c.f., Burns et al. 1969 |
| 1235 | 8100 | $^5B_2$ | 7600 | | +500 for phonon energy |
| | | $^1B_2$ | 9030 | | lowest singlet |
| 514 | 19455 | $^3E, ^3A_2$ | 19636, 19732 | -229 | |
| 500 | 20000 | $^5B_1$ | 19000 | | +1000 phonon energy |
| 463 | 21633 | $^3A_1$ | 21847 | -161 | |
| 460 | 21739 | | | | |
| 450 | 22222 | | | | unassigned |
| 425 | 23530 | $^3B_2$ | 23484 | 184 | |
| 420 | 23810 | | | | |
| 382 | 26180 | $^3A_2$ | 26488 | -170 | |
| 378 | 26455 | | | | |
| 353 | 28330 | $^3E$ | 28232 | 383 | |
| 346 | 28900 | | | | |
| 305 | 32800 | $^3E_1$ $^3B_1$ | 32547, 32474 | 290 | |

a. B = 582 $cm^{-1}$, C = 2601 $cm^{-1}$

b. for spin-forbidden bands only standard deviation 273 $cm^{-1}$

Figure 5

Modified Tanabe-Sugano diagram for $Fe^{2+}$ in gillespite. $B = 526\ cm^{-1}$. $C = 2652\ cm^{-1}$. The ratios of the one electron energy levels are kept constant while the magnitude of the field varies. Heavy lines are quintet states, light lines are triplets and the dashed lines are singlets. Only the three lowest energy singlets are shown. At zero pressure the ground state is $^5A_1$ and $^5B_1 - {}^5A_1 = 19{,}000\ cm^{-1}$ ( 19).

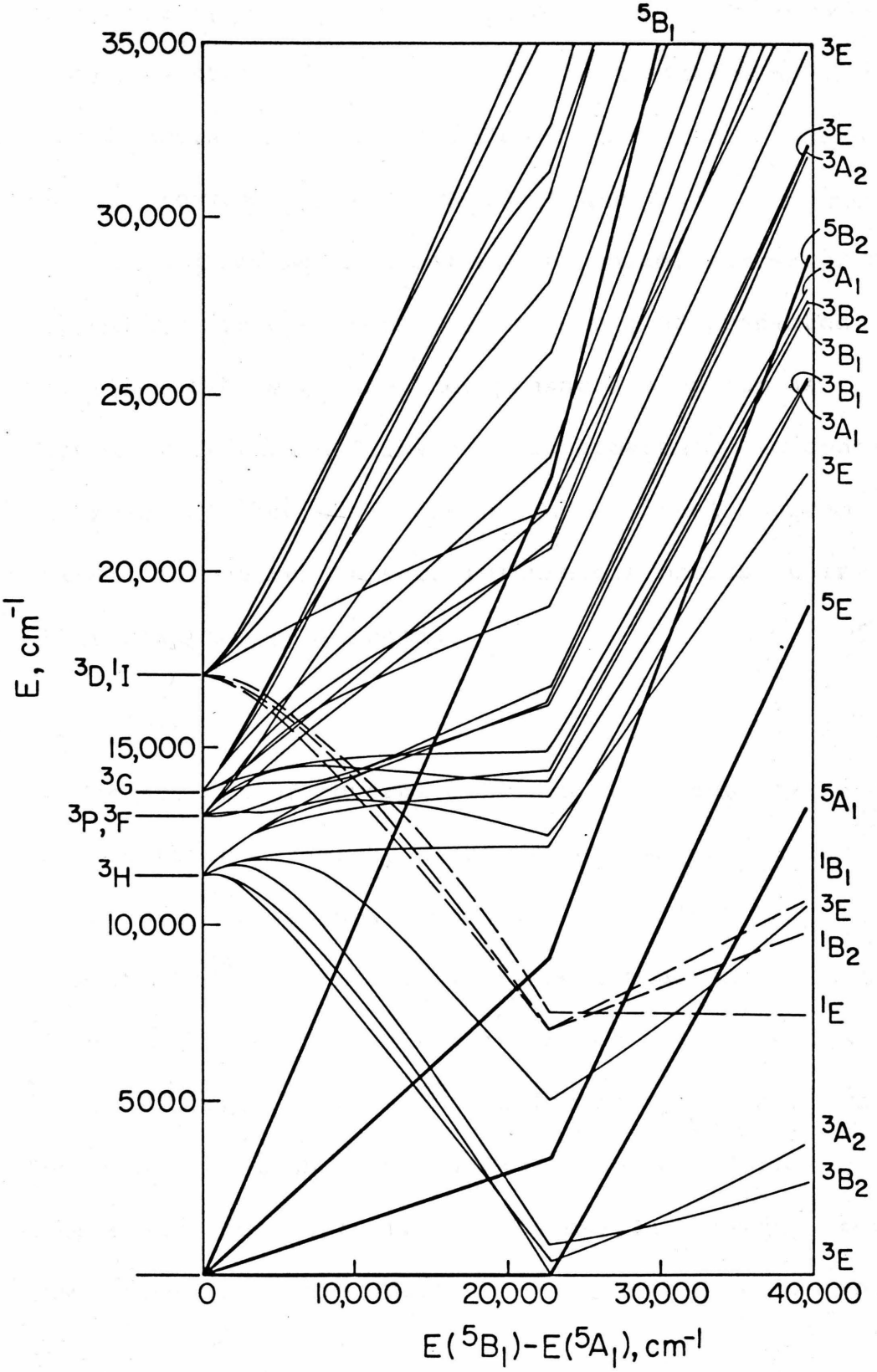
$^5B_1$
35,000
30,000
25,000
20,000
15,000
10,000
5000
0
$^3D, ^1I$
$^3G$
$^3P, ^3F$
$^3H$
E, cm$^{-1}$
10,000
20,000
30,000
40,000
E($^5B_1$)-E($^5A_1$), cm$^{-1}$
$^3E$
$^3E$
$^3A_2$
$^5B_2$
$^3A_1$
$^3B_2$
$^3B_1$
$^3B_1$
$^3A_1$
$^3E$
$^5E$
$^5A_1$
$^1B_1$
$^3E$
$^1B_2$
$^1E$
$^3A_2$
$^3B_2$
$^3E$

data of Strens (1 ) reporting an electronic phase transition at about 26 kbar. It does not seem justifiable to assign the high pressure phase a singlet ground state. However, using the revised estimate of Clark and Burns (19) for the $^5E_g$ - $^5A_{1g}$ splitting, and Strens' formulae, a greater range of stability for the triplet state would be predicted. The featureless nature of the high pressure spectrum as reported by Clark and Burns (19) is apparently in conflict with the prediction based on the energy level diagram. Perhaps the spectrum appears featureless because there are many overlapping broad bands.

D. Olivines

The spectra of several olivines have been described in considerable detail by Burns (4) who was primarily interested in the spin-allowed bands near 1000 nm. The spectra of $Fe^{2+}$-olivines show numerous weak bands in the visible which are usually attributed to spin-forbidden $Fe^{2+}$ transitions. However, detailed assignments are not often made. Caution is certainly justified in considering the spin-forbidden spectra of olivines because $Fe^{2+}$ occurs in two sites which are (different) distorted octahedra.

The distortions are fairly large and not purely tetragonal or trigonal. This situation leads to two difficulties: viz., the sites are difficult to treat theoretically and absorptions for the two sites are mixed. The splitting of the octahedral ground state ($^5T_{2g}$) is unknown for both $M_1$ and $M_2$. In the results discussed below a splitting of about 1500-3000 $cm^{-1}$ has been assumed. In view of the speculative nature of the olivine spectral assignments for spin-forbidden bands just discussed, caution is certainly called for in the application of the derived values of B and C.

The olivine spectra reported here were taken on a single crystal of Arizona peridot cut approximately normal to the β optic axis (z-crystallographic axis) and a tephroite (GRR # 7/18/72) of unknown orientation. Electron microprobe analyses of both olivines are given in Table 2. An unpolarized spectrum of both olivines was taken at room temperature and polarized spectra of the peridot at 7° K; these spectra are shown in Figure 6. The low temperature spectra in the infrared are fairly straightforward. The 1060 nm band due to $M_2$ is little affected by the low temperature with only a slight narrowing apparent. However, the bands on either side, due to vibronically allowed

Figure 6

Spectra of peridot and tephroite. a) $\gamma$-spectrum of peridot at liquid helium temperature. b) $\alpha$-spectrum of peridot at liquid helium temperature. c) Unpolarized spectrum of peridot at room temperature. d) Unpolarized spectrum of tephroite at room temperature. Sample thickness $\sim$ 2 mm for peridot, $\sim$ .5 mm for tephroite.

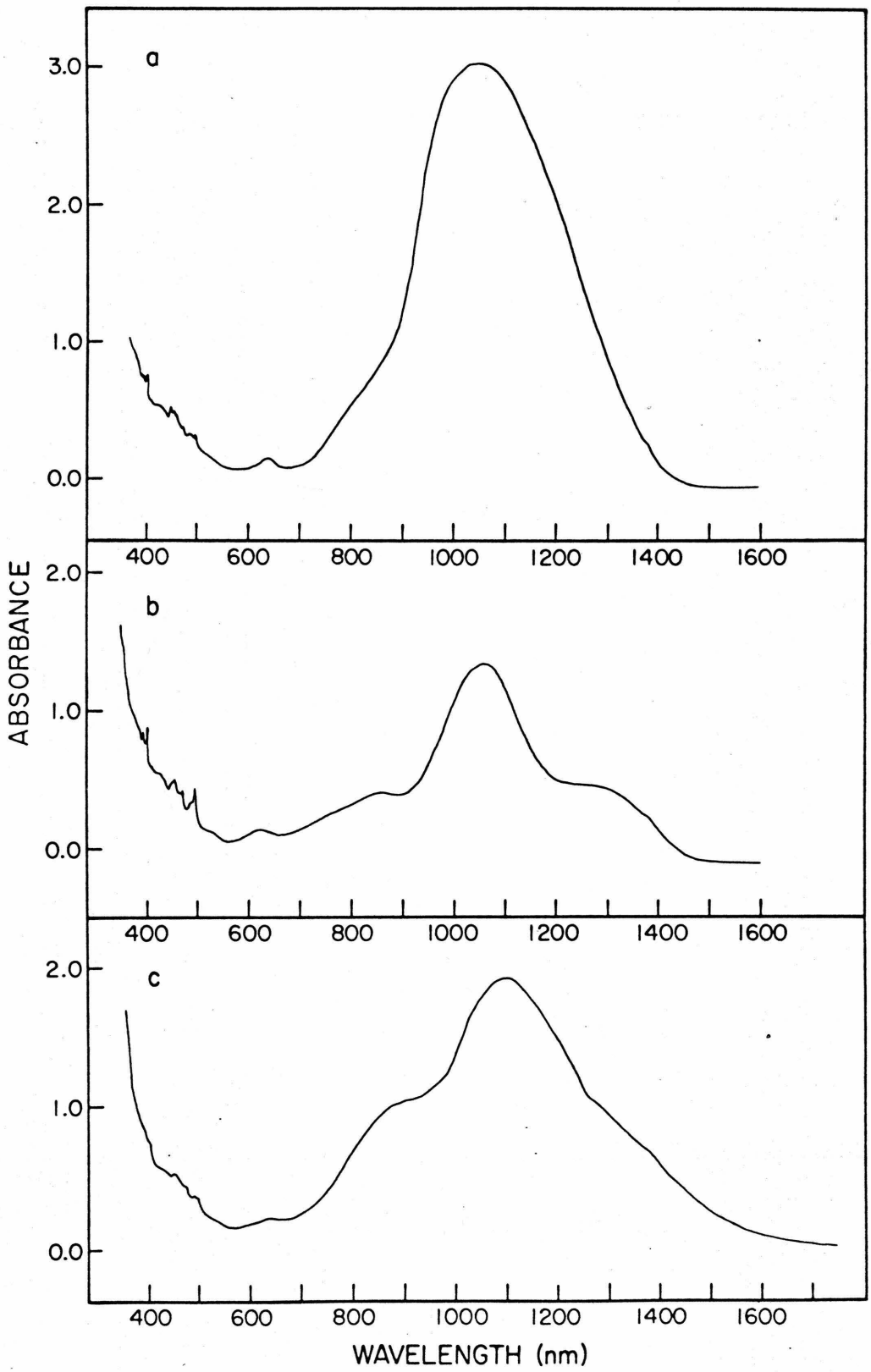
a
b
c
3.0
2.0
1.0
0.0
400
600
800
1000
1200
1400
1600
ABSORBANCE
WAVELENGTH (nm)

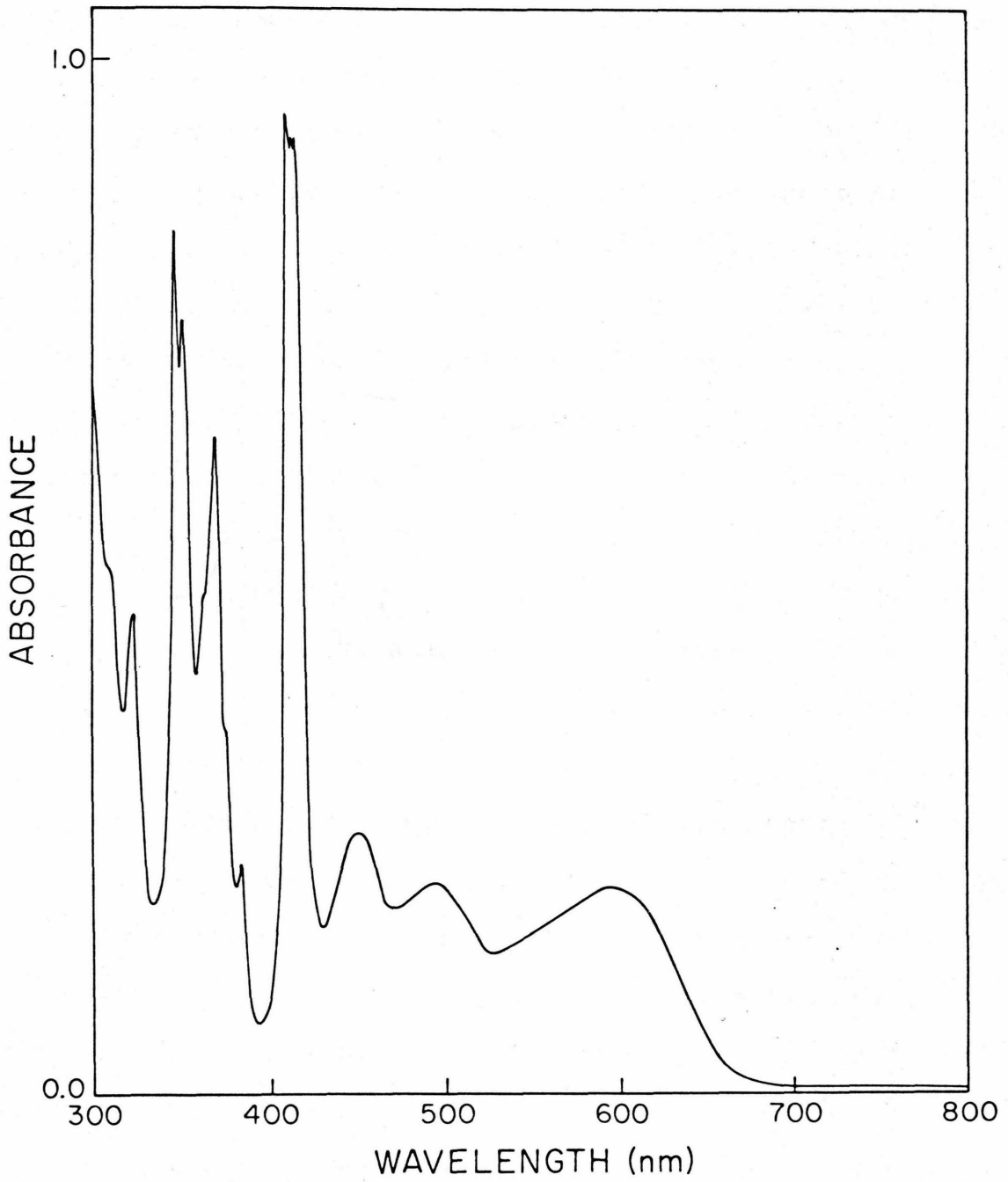
1.0
0.0
ABSORBANCE
300
400
500
600
700
800
WAVELENGTH (nm)

transitions in $M_1$ are considerably weaker at 7°K than at room temperature. This is to be expected since at low temperatures these bands can be excited only by emitting a phonon and not by absorbing one.

As with the garnets, we first consider the $Mn^{2+}$ spectra so that we may eliminate these features from the peridot spectra. The most prominent features are in the violet and ultraviolet - at 350 nm, 370 nm and 410 nm which are assigned to $^6A_1 \rightarrow {}^4E$, $^4T_2$ and ($^4A_1$, $^4E$) transitions, respectively. All of these features are split due to the presence of two sites of different symmetry, neither of which is perfectly octahedral. In view of this fact, detailed assignments of the weaker features may be unjustified, however, an assignment scheme is given in Table 8.

The visible portion of the 7°K spectra of the peridot are much more complicated with most of the bands seen at room temperature narrowing considerably and separating into several sharp peaks. As mentioned above, the complexity of the olivine structure makes a detailed assignment of the spectra very difficult. Because of the importance of spin-orbit coupling in providing any intensity at all to these bands, polarization arguments are really of little help in the assignment. Several different assignments were made

TABLE 7 SPECTRUM OF TEPHROITE

| λ(nm) | $E_{obs}(cm^{-1})$ | $E_{calc}(cm^{-1})$ | ASSIGNMENT |
|---|---|---|---|
| 605 | 16530 | 16773 | $^6A_1 \rightarrow {}^4T_1$ |
| 497 | 20120 | 20536 | $^6A_1 \rightarrow {}^4T_2$, $^4E$, $^4A_1$ |
| 448 | 22320 | | |
| 412 | 24270 | 24205 | $^6A_1 \rightarrow {}^4A_1$, $^4E$ |
| 385 | 25970 | | $^6A_1 \rightarrow {}^4T_2$ (?) |
| 370 | 27030 | 26890 | $^6A_1 \rightarrow {}^4T_2$ |
| 351 | 28490 | 28916 | $^6A_1 \rightarrow {}^4E$ |
| 347 | 28820 | | |
| 323 | 30960 | | Unassigned |

Dq = 1006 $cm^{-1}$, B = 673 $cm^{-1}$, C = 3495 $cm^{-1}$

Standard deviation of fit = 217 $cm^{-1}$.

and B and C adjusted to fit the spectra. The best fit results from the assignment scheme of Table 8.

The assignment of Burns (4) must be rejected in view of the very low Dq (553 $cm^{-1}$) required to attain a standard deviation only slightly below 400 $cm^{-1}$. Several other assignment schemes give standard deviations near 200 $cm^{-1}$ and have reasonable crystal fields, however, the values of the Racah coefficients (especially the ration C/B) seem unreasonable in most cases (in view of values consistently near 5 found in other materials (described above)). For this reason the assignment shown seems to be the best estimate of the truth. Note however, that the peaks near 21,500 $cm^{-1}$ are not assigned in this scheme. No explanation of these features is offered here.

There is an additional complication in the assignment of the olivine spectra; viz., that the splitting of the octahedral ground state ($^5T_{2g}$) is unknown for both $M_1$ and $M_2$. In the results of Table 8 a splitting of about 1500 $cm^{-1}$ has been assumed. In view of the speculative nature of the olivine spectral assignments for spin-forbidden bands just discussed, caution is certainly called for in the application of the derived values of B and C.

Table 8

Spectra of Olivine (7°K)

| α(=b) | | γ(=a) | | | |
|---|---|---|---|---|---|
| λ(nm) | $E_{obs}(cm^{-1})$ | λ(nm) | $E_{obs}(cm^{-1})$ | $E_{cal}(cm^{-1})$ [a] | Assignment |
| 1380 | 7245 | 1380 | 7245 | | $M_1$ |
| 1325 | 7545 | | | | |
| 1055 | 9480 | 1075 | 9300 | 9186 | $M_2(^5A_1 \rightarrow {}^5E)$ |
| 845 | 11830 | | | | $M_1$ |
| 750 | 13300 | | | 13072 | $M_2(^3T_1)$ |
| 625 | 16000 | 636 | 15720 | 15838 | $M_2(^3T_2)$ |
| 530 | 18870 | | | 18991 | $M_2(^3T_1)$ |
| 495 | 20200 | | | 20299 | $M_2(^3T_2)$ |
| 490 | 20410 | | | | $M_2(^3T_2) + \nu_1$ [b] |
| | | 484 | 20660 | | $M_2(^3T_2) + \nu_1 + \nu_2$ |
| 471 | 21230 | 471 | 21230 | 21339 | $M_2(^3T_1)$ |
| | | 459 | 21790 | 21752 | $M_2(^3E)$ |
| 455 | 21980 | | | | $M_2(^3T_1) + \nu_1$ |
| 451 | 22170 | 452 | 22120 | | $M_2(^3T_1) + 2\nu_1$ |
| | | 447 | 22370 | | $M_2(^3T_1) + 2\nu_1 + \nu_2$ |
| 437 | 22880 | 430 | 23260 | | Unassigned |
| 426 | 23470 | | | | |
| 410 | 24390 | 410 | 24390 | | $Mn^{2+}\ {}^6A_1 \rightarrow {}^4A_1, {}^4E$ |
| 402 | 24880 | 402 | 24880 | 24727 | $M_2(^3T_2)$ |
| 401 | 24940 | 401 | 24940 | | |
| | | 399 | 25060 | | $M_2(^3T_2) + \nu_1$ |
| | | 395 | 25320 | | $M_2(^3T_2) + \nu_1 + \nu_2$ |
| 393 | 25450 | | | | $M_2(^3T_2) + \nu_1 + \nu_2 + \nu_3$ |
| | | 387 | 25840 | | Unassigned |
| | | 384 | 26040 | 26030 | $M_2(^3A_2)$ |
| | | 375 | 26670 | 26696 | $M_2(^3T_1)$ |

a. Using pure $O_h$ symmetry Dq = 718.6 $cm^{-1}$, B = 732 $cm^{-1}$, C = 3310 $cm^{-1}$ and assuming that the ground state ($^5T_2$ in $O_h$) is split into $^5A_1$ + $^5E$ with a separation of 3000 $cm^{-1}$ and $^5A_1$ ground state.

b. Vibrational frequencies: $\nu_1 \sim 200\ cm^{-1}$, $\nu_2 \sim 250\ cm^{-1}$, $\nu_3 \sim 150\ cm^{-1}$.

E. Discussion

In the sample of minerals considered here, spin-forbidden transitions of $Fe^{2+}$ have been observed whenever ferrous iron is an important component of the mineral. The exact position and the assignment of these transitions varies markedly from one mineral to the next. This is not surprising, because of the variability of the energy of the spin-allowed transitions. Nonetheless we are led to suspect that weak features in the absorption spectra of other ferrous minerals, especially in the range 400 to 600 nm, might be due to spin-forbidden transitions of $Fe^{2+}$. Such features are found in orthopyroxene, hedenbergite, cummingtonite, gruenerite, and actinolite (5) and in the case of enstatite have been assigned to spin-forbidden transitions (6). Because of the complexity of the coordination polyhedra involved, detailed analysis of these bands is not feasible at present, however they would be a very suitable subject for a separate investigation.

The data of the previous sections may be used to try to estimate the manner in which B and C vary with interatomic distance. First, however, we must agree on the meaning of "interatomic distance" when the surrounding ions are not all at the same distance. (In the case of

olivine there is the additional complication that the interatomic distance measured by x-ray diffraction is the mean for Fe-O and Mg-O. Inasmuch as there is no way to circumvent this difficulty, the x-ray values will be used here.) The two obvious choices are the mean separation and the minimum separation. The values of B and C for the cases described above are plotted against the minimum distance in Figure 7. No apparent trend exists and the gillespite data appear to be anomalous. Use of means instead of minima does not change this.

These poor results, although clearly unsatisfying, are not at all unexpected. The materials studied are quite diverse, and in none of them is the coordination of $Fe^{2+}$ close to that in another. It appears, for the materials studied here, that the effects of coordination on B and C are at least as great as those of interatomic distance. Clearly we must study either many materials with nearly identical coordination, or one material as it is compressed, if we wish to determine how B and C will vary with interatomic distance. Drickamer and co-workers (21-23) have done the latter for B in compounds of several transition metals, but not for $Fe^{2+}$. Their results for $Co^{2+}$, $Ni^{2+}$ and $Cr^{3+}$ are summarized in Figure 8. Although B decreases on compression in each case, there is no other

Figure 7

Variation of Racah parameters, B and C, with minimum interatomic distance. Squares represent C with the scale to the right; circles represent B with the scale to the left.

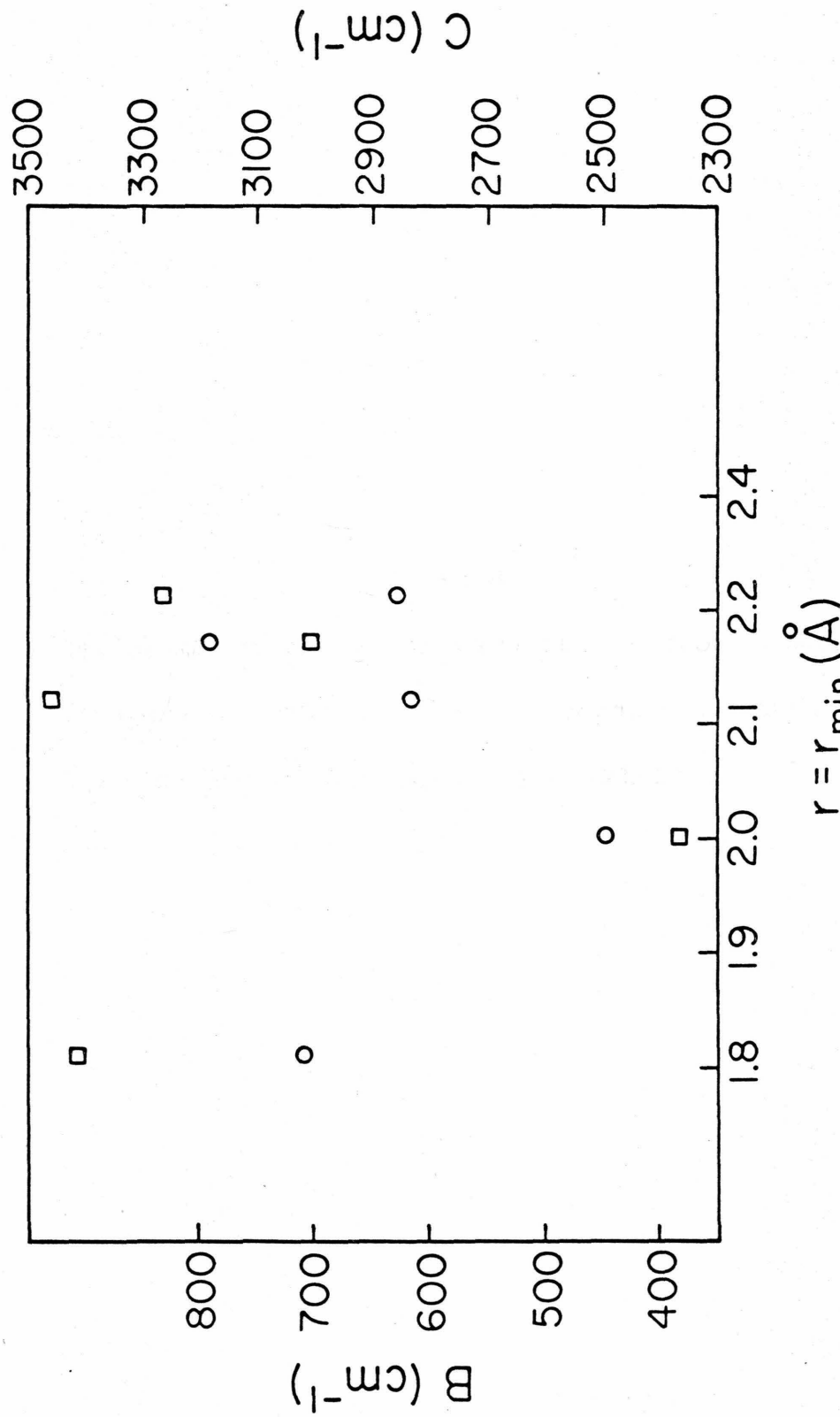
C (cm⁻¹)
3500
3300
3100
2900
2700
2500
2300
B (cm⁻¹)
800
700
600
500
400
1.8
1.9
2.0
2.1
2.2
2.4
r = r_min (Å)

Figure 8

Variation of the Racah parameter B upon compression in several transition metal compounds. Data are from Drickamer and co-workers (21-23).

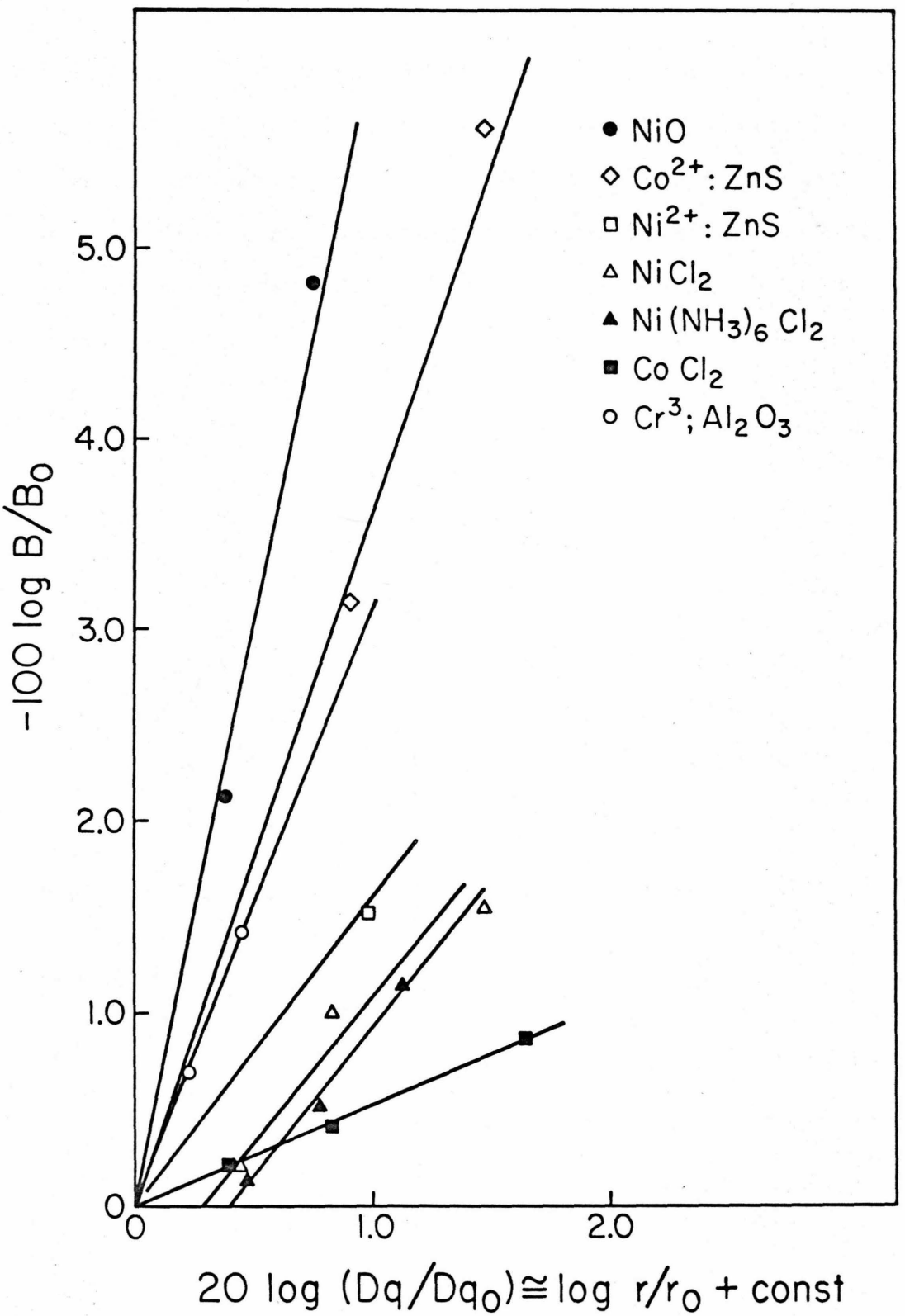
NiO
Co2+: ZnS
Ni2+: ZnS
Ni Cl2
Ni (NH3)6 Cl2
Co Cl2
Cr3; Al2 O3
-100 log B/B0
5.0
4.0
3.0
2.0
1.0
0
0
1.0
2.0
20 log (Dq/Dq0) ≅ log r/r0 + const

unique relation to r (as determined from the variation of Dq) from one compound to another. From the limited data presented it appears that dlogB/dlog r depends on the coordinating ligand, decreasing in the order O > S > $NH_3$ > Cl. For the oxides shown it ranges from 3 to about 6.

## REFERENCES

(1) R. G. J. Strens, Pressure-induced spin-pairing in gillespite, $BaFe^{II}Si_4O_{10}$. Chem Comm., 777 (1966).

(2) R. G. J. Strens, The nature and geophysical importance of spin pairing in minerals of iron (II). S. K. Runcorn (ed.) Applications of Modern Physics to the Earth and Planetary Interiors. Academic Press, New York, 213-220 (1969).

(3) C. Furlani, Spettri di assorbimento di complessi elettrostatici del $Fe^{++}$. Gazz. Chim. Ital. 87, 371-379 (1957).

(4) R. G. Burns, Crystal field spectra and evidence of ordering in olivine minerals. Am. Mineralog. 55, 1608-1632 (1970).

(5) R. G. Burns, Mineralogic Applications of Crystal Field Theory. 224 pp., Cambridge Univ. Press, Cambridge (1970).

(6) W. B. White and K. L. Keester, Optical absorption spectra of iron in rock-forming silicates. Am. Mineralog. 51 774-791 (1966).

(7) G. A. Slack, $FeAl_2O_4$-$MgAl_2O_4$: Growth and some thermal, optical and magnetic properties of mixed single crystals. Phys. Rev. 134, A 1268-1280 (1964).

(8) Y. Tanabe and S. Sugano, On the absorption spectra of complex ions. I. J. Phys. Soc. Japan 9, 753-766 (1954).

(9) G. A. Slack, F. S. Ham, and R. M. Chrenko, Optical absorption of tetrahedral $Fe^{2+}$ ($3d^6$) in cubic ZnS, CdTe, and $MgAl_2O_4$. Phys. Rev. 152, 376-402 (1966).

(10) J. S. Griffiths, The Theory of Transition-Metal Ions. p. 437, Cambridge Univ. Press, Cambridge (1964).

(11) T. J. Shankland, Pressure shift of absorption bands in $MgO:Fe^{2+}$ and the dynamic Jahn-Teller effect. J. Phys. Chem. Solids 29, 1907-1909 (1968).

(12) G. A. Slack and R. M. Chrenko, Optical absorption of natural garnets from 1000 to 30,000 wavenumbers. J. Opt. Soc. Am. 60, 1325-1329 (1971).

(13) O. Weigel and H. Ufer, Uber Mineralfarbungen. II. Die Absorption einiger rot gefarbter Mineralien und kunstlicher Praparate im sichtbaren und ultravioletten Tiel des Spektrums. Neves jahrb. Mineral. Geol. und Palaont. 57A, 397-500, 1928.

(14) B. W. Anderson, Properties and classification of individual garnets. J. Gemmology 7, 1- 7 (1959).

(15). P. G. Manning, The optical abosrption spectra of the garnets almandine-pyrope, pyrope and spessartine and some structural interpretations of mineralogical significance. Can. Mineralog. 9, 237-251.

(16) G. A. Novak and G. V. Gibbs, The crystal chemistry of the silicate garnets. Am. Mineralog. 56, 791-825 (1971).

(17) G. R. Rossman, II. Spectroscopic and mangetic studies of monomeric and dimeric $d^5$ systems. Ph. D. Dissertation, California Institute of Technology, Pasadena (1972).

(18) J. Otsuka, Electrostatic interaction of $d^n$ systems in tetragonal fields. J. Phys. Soc. Japan 21, 596-620 (1966).

(19) M.G. Clark and R. G. Burns, Electronic spectra of $Cu^{2+}$ and $Fe^{2+}$ square planar co-ordinated by oxygen in $BaXSi_4O_{10}$. J. Chem. Soc. (A), 1034-1038 (1967).

(20) J. E. Wainwright, Reinvestigation of the crystal structure of gillespite. (abs.) Joint Ann. Meeting Geol. Assoc. Canada-Mineralog. Assoc. Canada, 57 (1969).

(21) J. C. Zahner and H.G. Drickamer, Effect of pressure on crystal-field energy and covalency in octahedral complexes of $Ni^{2+}$, $Co^{2+}$ and $Mn^{2+}$. J. Chem. Phys. 35, 1483-1490 (1961).

(22) D. R. Stephens and H. G. Drickamer, Effect of pressure on the spectrum of ruby. J. Chem. Phys. 35, 427-429 (1961).

(23) R. W. Parsons and H. G. Drickamer, Effect of pressure on the spectra of certain transition metal complexes. J. Chem. Phys. 29, 930-937 (1958).

(24) R. G. Burns and F. E. Huggins. Cation determinative curves for Mg-Fe-Mn olivines from vibrational spectra. Am. Mineralog. 57, 967-985 (1972).

# IV. HIGH PRESSURE SPECTROSCOPY

The absorption spectra of minerals at very high pressures is of considerable importance to the problem of the behavior of $Fe^{2+}$ in the interior of the earth. Specifically, measurements of the pressure shifts of absorption bands, both spin-allowed and spin-forbidden, over a range of several hundred kilobars would provide an excellent basis for the prediction of crystal field effects in the lower mantle. Furthermore, should a phase change occur in the course of such experiments, it is likely that the local site symmetry of $Fe^{2+}$ in the high pressure phase could be determined from its absorption spectrum. In many cases such a knowledge, combined with the knowledge of the density of the high pressure phase, could unequivocably determine the structure of that phase.

For these reasons a program was undertaken to develop a system capable of measuring optical absorption spectra of solids during the time that they are undergoing shock wave compression to pressures in excess of 500 kbar. This system is described below and its present capabilities illustrated in the discussion of results for periclase and ruby.

## A. Experimental Technique

Time-resolved spectral measurements of a solid during shock loading have never been performed although single-frame spectra of shocked liquids have been reported (1) using an explosive-argon light source. Use of such a source is not feasible at the Caltech facility so an alternative light source has been developed for such studies. In addition, a different optical path better suited to solid samples is used.

The spectrograph system described below was specifically designed for use with the high velocity propellant gun at the Kresge Seismological Laboratory but could be adapted for use with most shock facilities. Light from an electrical-arc discharge is focused on the sample by an optic system and is internally reflected back along a similar path (see Figure 1). The ingoing and outcoming rays diverge slightly (13°) permitting the latter to be focused on the entrance slit of a simple reflection grating spectrograph. The exit part of the spectrograph is a slit, elongated in the direction of dispersion, which is the object for a TRW model 1D image converter streak

Figure 1

Schematic representation of a spectrographic system designed to measure optical absorption spectra during shock loading to pressures in excess of 500 kbar.

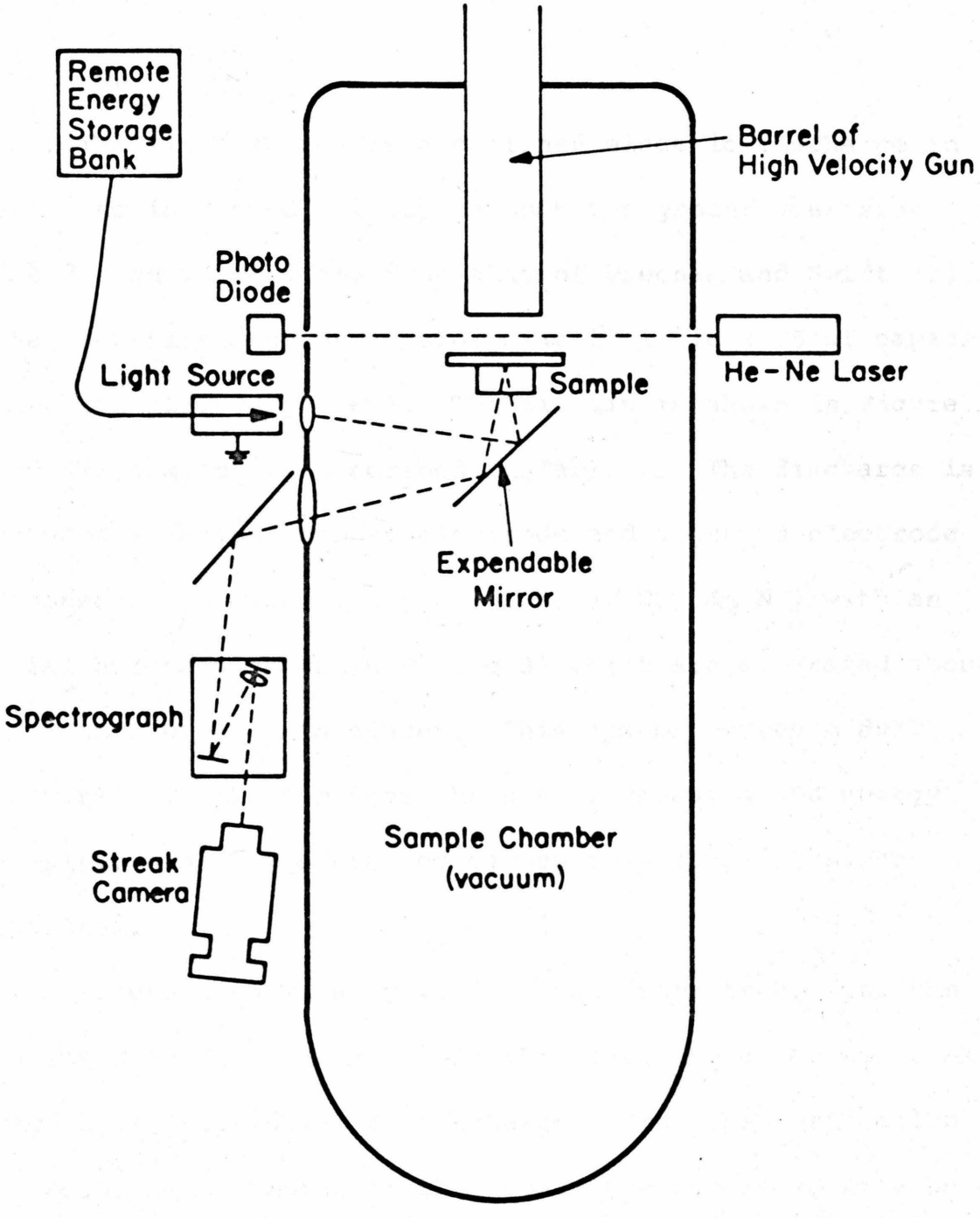
Remote
Energy
Storage
Bank
Barrel of
High Velocity Gun
Photo
Diode
Light Source
Sample
He-Ne Laser
Expendable
Mirror
Spectrograph
Streak
Camera
Sample Chamber
(vacuum)

camera. The resulting image is a plot of light intensity as a function of wavelength and time.

## A.1 Light Source

The light source is a confined electric discharge in air, and is viewed axially through the ground electrode. The design is modified from that of Preonas and Swift (2). The electrical energy is stored at 20 kv in a 75 μf capacitor bank (15,000 joules). The circuit is shown in Figure 2 and the components described in Table 1. The discharge is between a central copper electrode and a ground electrode (copper or tungsten-alloy — 70% W, 6% Cu, 4% Ni) with an axial hole (as shown in Figure 3) which are separated about 1/16 inch by a lexan spacer. This spacer serves a dual purpose; it both confines the arc, increasing the energy density, and is a source of carbon to produce a smooth spectrum.

Figure 4 shows a typical voltage-time trace from the ignitron anode to ground. In this case the capacitor bank was at 19.5 kv, prior to discharge. From the oscillation frequency and damping of this curve the arc resistance is estimated to be on the order of 0.1 ohm. The intensity of

Figure 2

Circuit diagram of a high intensity point light source used to measure spectra in shocked solids. Components are described in Table 1.

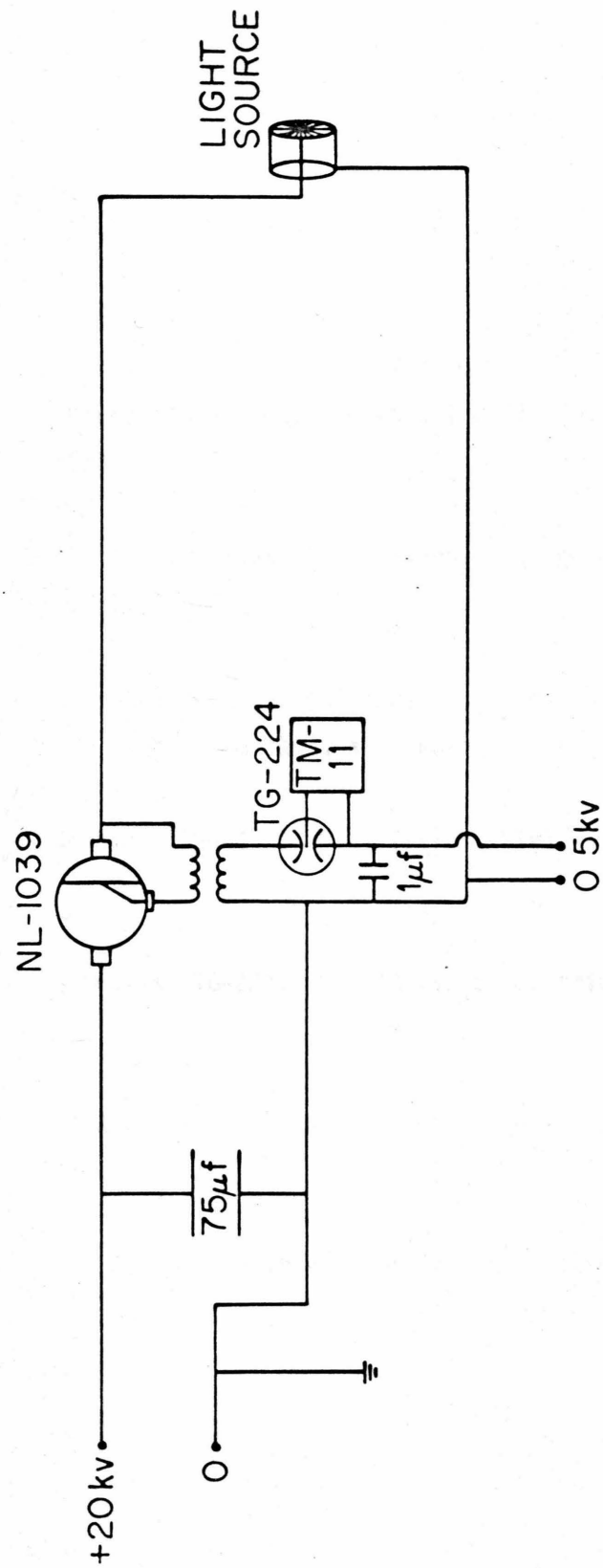
LIGHT SOURCE
NL-1039
TG-224
TM-11
1μf
0 5kv
75μf
+20kv
0

TABLE 1 COMPONENTS OF LIGHT SOURCE

| COMPONENT | DESCRIPTION |
|---|---|
| Power supply (Main) | Universal Voltronics Comtrol, 0-32 kVDC (reversible), 25mA |
| Capacitor Bank | 5 - Aerovox 15$\mu$f, 20 kV energy storage capacitors in parallel |
| Switching Ignitron (NL-1039) | National NL-1039 ignitron, 20 kV peak anode voltage, 100 kA peak current, air cooled |
| Power Supply (trigger) | Beckman 1150-1, 0-10 kV (reversible), 9 mA |
| Triggered Spark Gap (TG-224) | Signalite TG-224, .5 - 18 kV, 6 kJ, triggered spark gap |
| Trigger Module (TM-11) | EG & G TM-11 Trigger Module 0-30 kV output remote trigger |
| Cable | RG-221 14,kV 50 ohm coaxial cable (armored) |

Figure 3

Detail of the electrode configuration of high intensity point light source.

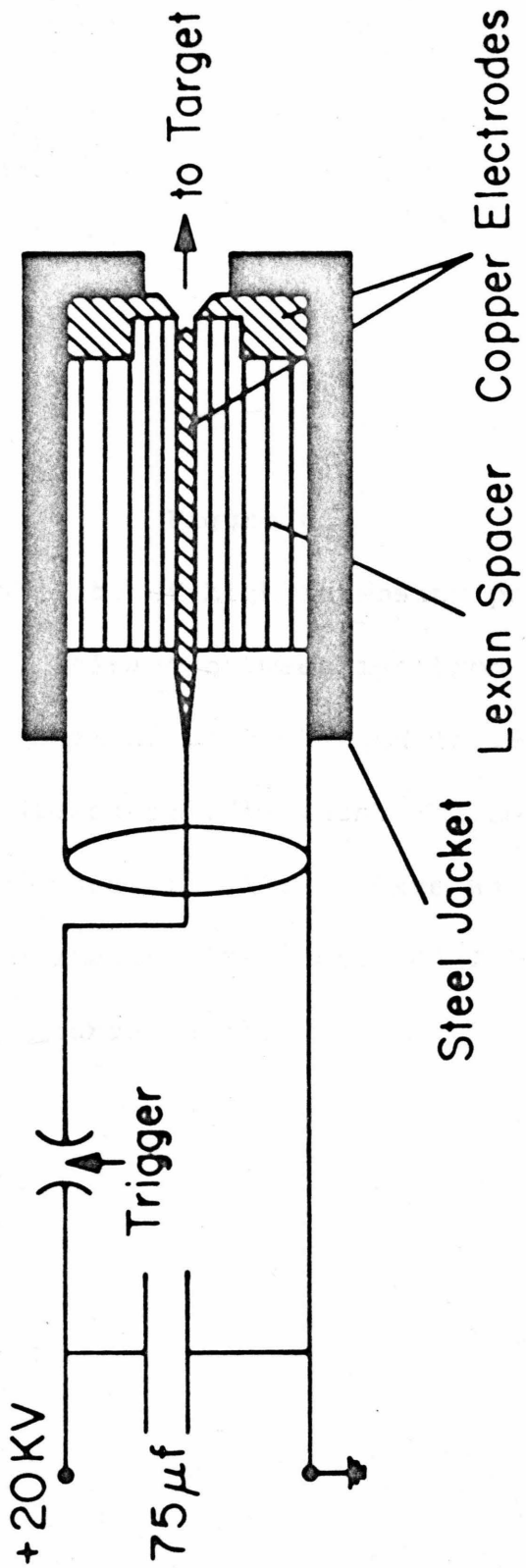
to Target
Copper Electrodes
Lexan Spacer
Steel Jacket
Trigger
+20KV
75μf

Figure 4.

Time variability of high intensity point light source. a) Voltage between ignitron anode and ground. Capacitor bank charged to 19.5 kv. Ground electrode diameter: 1/16 inch. b) Intensity of light emitted by source in (a). c)Same as (a) but ground electrode diameter: 1/8 inch. d) Intensity of light emitted by source in (c).

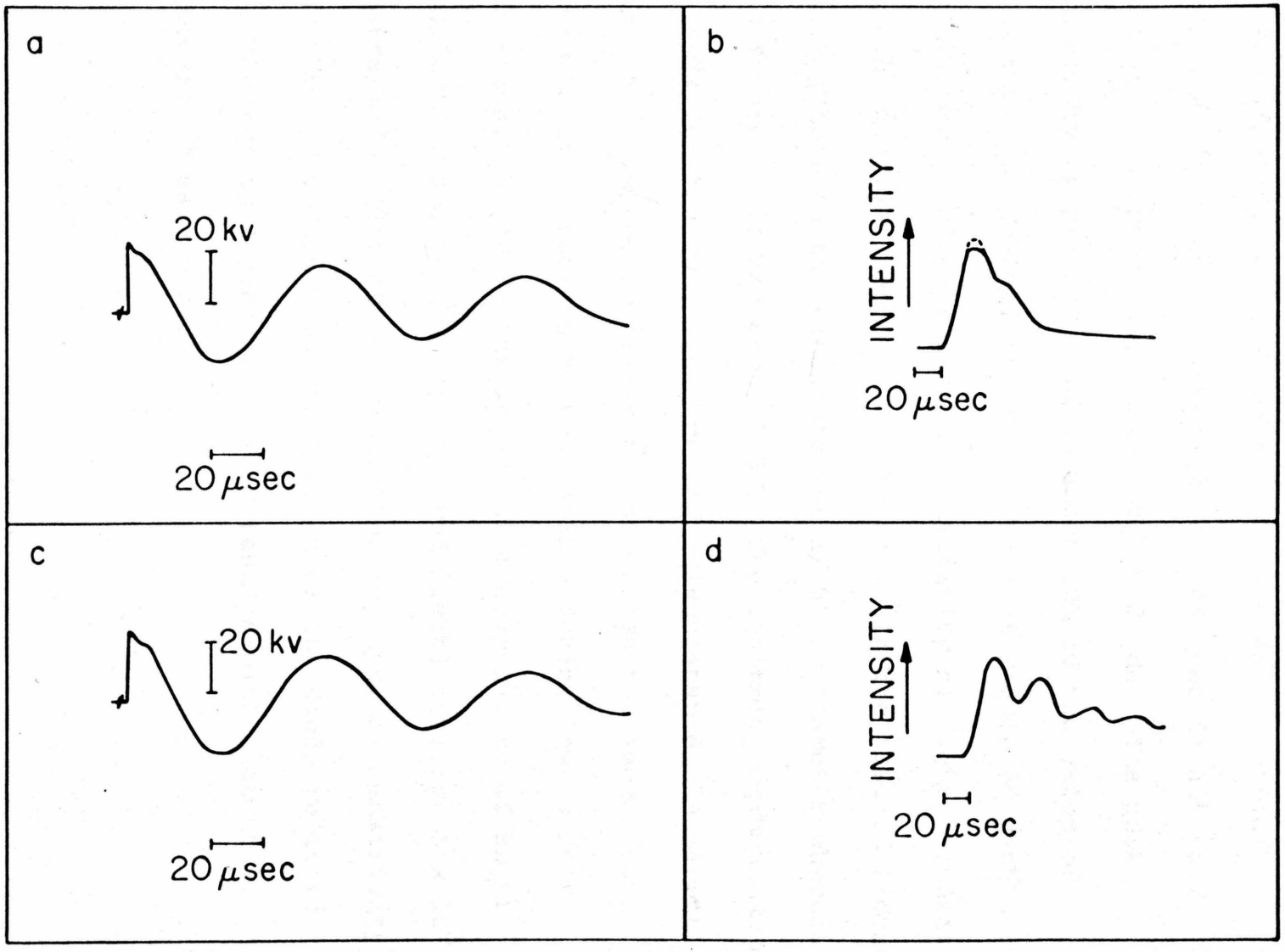
a
20 kv
20 μsec
b
INTENSITY
20 μsec
c
20 kv
20 μsec
d
INTENSITY
20 μsec

this discharge was monitored with a red-sensitive photo-diode (HP-4220) and is shown in Figure 4b. The flat portion of the curve between 25 and 45 μsec is not real but is produced by saturation of the diode. The peak intensity is probably within about 10% of the value of saturation. Comparison of the curve of Figure 4d with that of Figure 4b illustrates the sensitivity of light intensity to the detailed geometry of the gap. In the case of Figure 4b the hole in the electrode was 1/16" in diameter whereas in Figure 4d it was about 1/8". The ignitron anode voltage curves for the two cases are indistinguishable. Apparently, the large volume available to the arc in the second case permits it to cool much more rapidly during low current episodes. At 20 kv the light has a temperature of about 60,000° K and a peak intensity (red light) of about $5 \times 10^3$ watts/$cm^2$. (Use of the manufacturers "typical sensitivity" of the photo-diode and calibration of the diode relative to the sun on a clear day yield results within about 10 percent of each other.)

## A.2 Spectrograph and Camera

The spectrograph used (illustrated in Figure 5) has a linear dispersion at the exit port of about 100 Å/mm. The exit port is a slit 0.5 mm wide and about 10 cm long in the direction of dispersion. The grating can be changed to give other values of dispersion although greater dispersion is possible only by sacrificing already limited light intensity. Wavelength calibration of all records after the first one was achieved with a pulsed argon laser (TRW Model 71A).

The TRW (Model 1D) image converter streak camera used in the present system operates with a S-11 photocathode. This is the most stringent limitation on the system because of the narrow spectral sensitivity of this surface (0.4 μm to 0.63 μm). The spectral response of the camera is shown in Figure 6. The S-20 photocathode available on the same model camera would be preferable because of its greater sensitivity (about 50 percent greater) and slightly wider response. Of the various surfaces presently available one of the GaAs surfaces such as RCA's 128 or 134 would be best if available because of the sensitivity and flatness throughout the visible portion of the spectrum.

Figure 5

Schematic representation of spectrograph used for measuring optical absorption spectra of shocked solids. a) Entrance slit, b) diffraction grating, c) focusing lens, d) exit slit.

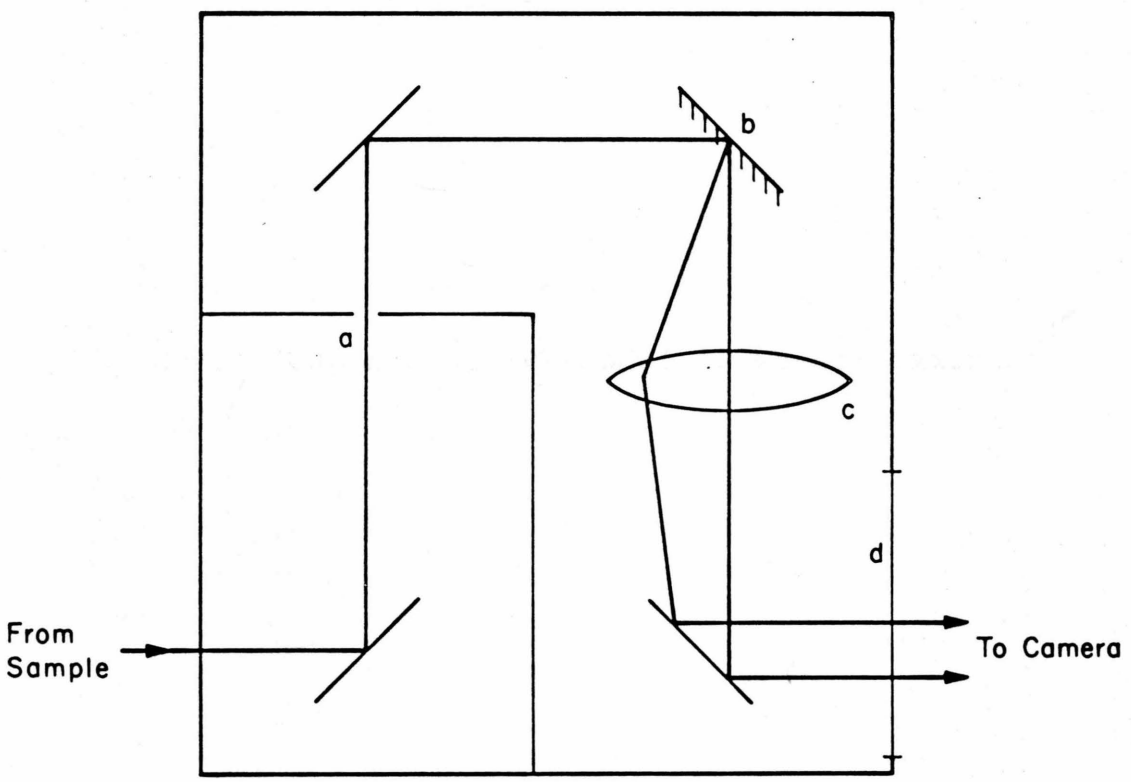
b
a
c
d
From
Sample
To Camera

Figure 6

Spectral response of TRW-Model 1D streak camera.

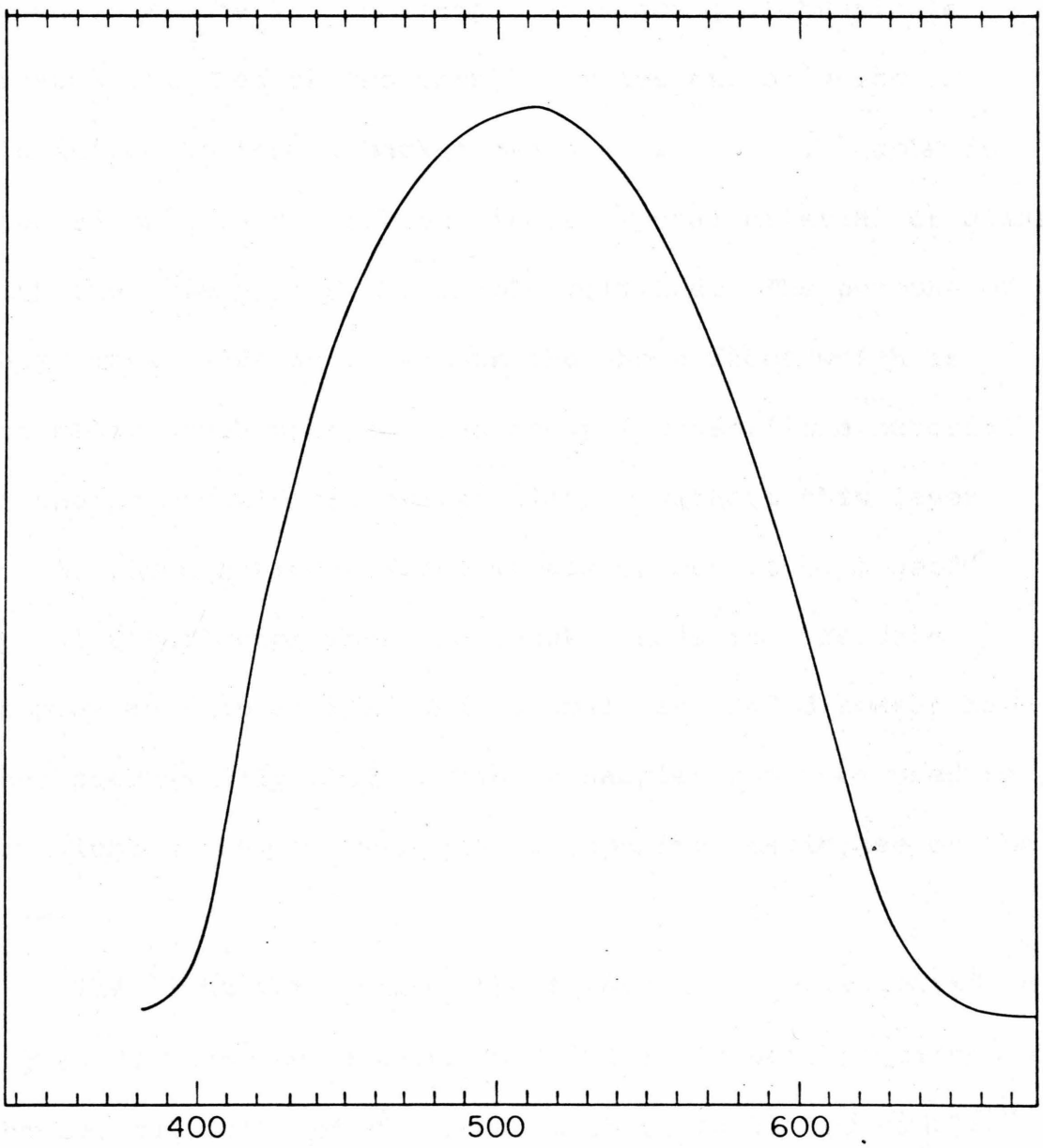
400
500
600

## A.3 Sample

The sample configuration used with this system is shown in Figure 7. The sample is a gem quality single crystal polished on two parallel sides one of which is aluminized to form a back-surface mirror. The sample is mounted on a thin slab of single crystal material or glass with the side toward the sample polished. The purpose of this extra layer is to smooth the shock front which is optically rough upon leaving the polycrystalline material of the projectile and driver plate. Without this layer the mirrored surface of the sample ceases to be a good specular reflector when the shock passes it. To date samples as thin as 1/8" and as small as 3/4" diameter have been successfully used. Thinner samples could be used by sandwiching them between glass, sapphire, periclase or the like.

The light path within the target is also indicated in Figure 7. The near normal (6 1/2° ) incidence, required by the optical path of the present shock facility, reduces reflection losses at the free surface and the double path length allows greater total absorption than a single transit. The light path after impact is also indicated.

Figure 7

Detail of the sample arrangement before impact (above) and during shock transit (below) showing light path and regions of the sample studied.

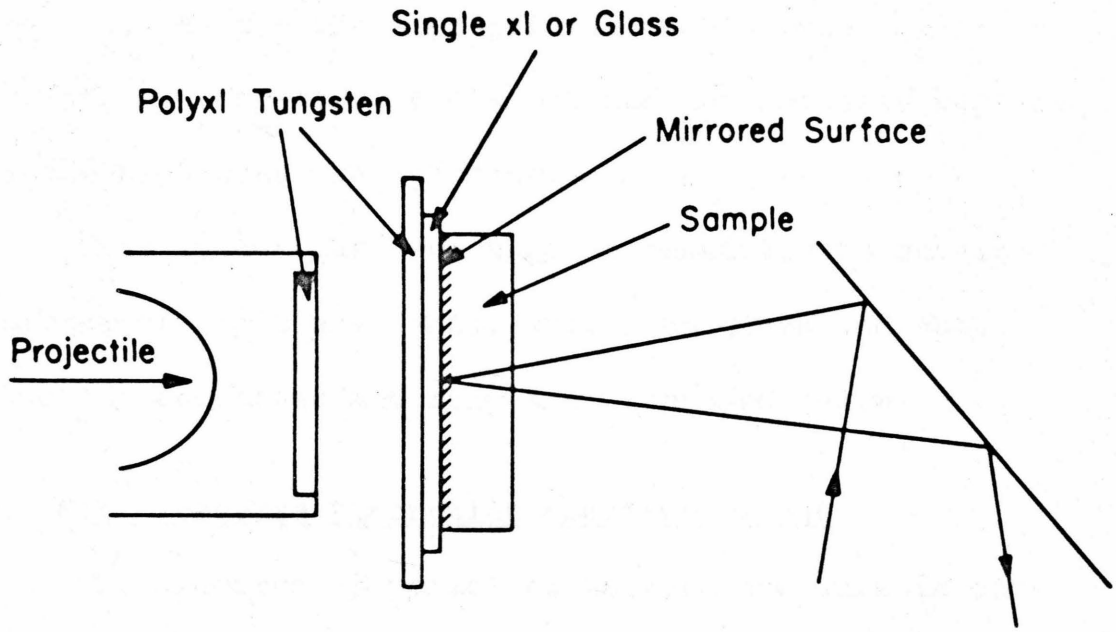


Before Impact

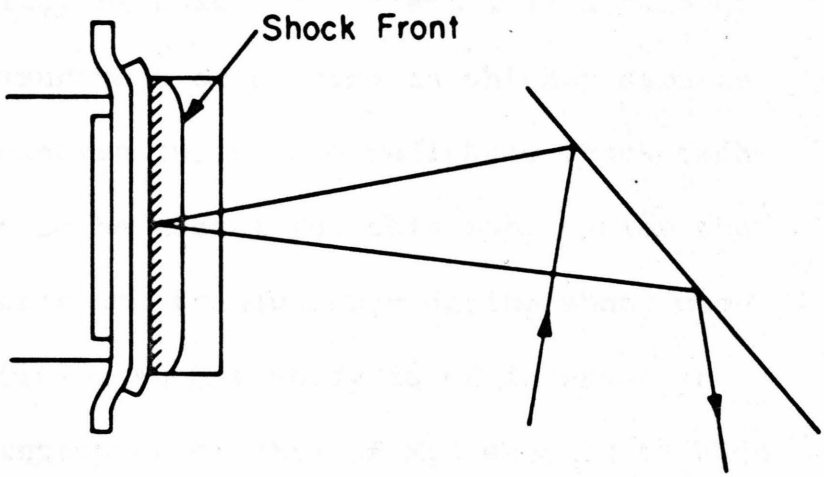


During Shock Transit

In this case the path samples both high- and low-pressure regions. As the shock progresses through the sample the low-pressure spectrum fades out and is gradually replaced by the high-pressure spectrum.

This system has been used successfully to obtain spectra of periclase (MgO), soda-lime glass and ruby. Data for periclase and ruby are discussed below.

B. High Pressure Absorption Spectrum of MgO

The spectrum of periclase at zero pressure is completely featureless in the visible region. A study of the spectrum of shock compressed MgO was undertaken to determine the feasibility of using the material as a "window" to permit the measurement of spectra in thinner samples and at higher pressures (using the reflected shock technique). In order to be useful for this application the material must retain its transparency during shock compression. In addition such a study is of interest in order to better interpret spectra of MgO shocked to high pressures and recovered. Gager et al. (3) have observed F-centers in MgO recovered from a shock pressure in excess of 500 kbar. Such features should be observable in these

absorption spectra whether they are produced on loading or unloading.

In Figure 8 a record of the absorption spectrum of MgO shocked to 465 ± 10 kbar final pressure is shown. The pressure is inferred from the impact velocity and the known Hugoniots of the flyer plate and sample. Such a shock should be preceded by an elastic precursor with a normal stress of about 90 kbar (4). The difference in velocity of the two shocks should be about 1.5 mm/μsec with the elastic shock travelling at 10.1 mm/μsec. In the upper portion of the picture we see the spectrum of the unshocked MgO followed by a sharp decrease in intensity indicating the arrival of the shock at the internal mirror surface. It is not possible with this experiment to separate the three possible causes of this decrease: 1) absorption in the shock front, 2) degradation of the mirror by the shock or 3) rotation of the mirror by an oblique shock impact. Any or all of these features could lead to observed featureless decrease in light intensity.

In the region below this discontinuity (region B) the spectrum is progressively changing from that of unshocked MgO to that of shocked MgO. The opacity of the shocked

Figure 8

Absorption spectrum of periclase (MgO) shocked to 465 kbar. See text for discussion.

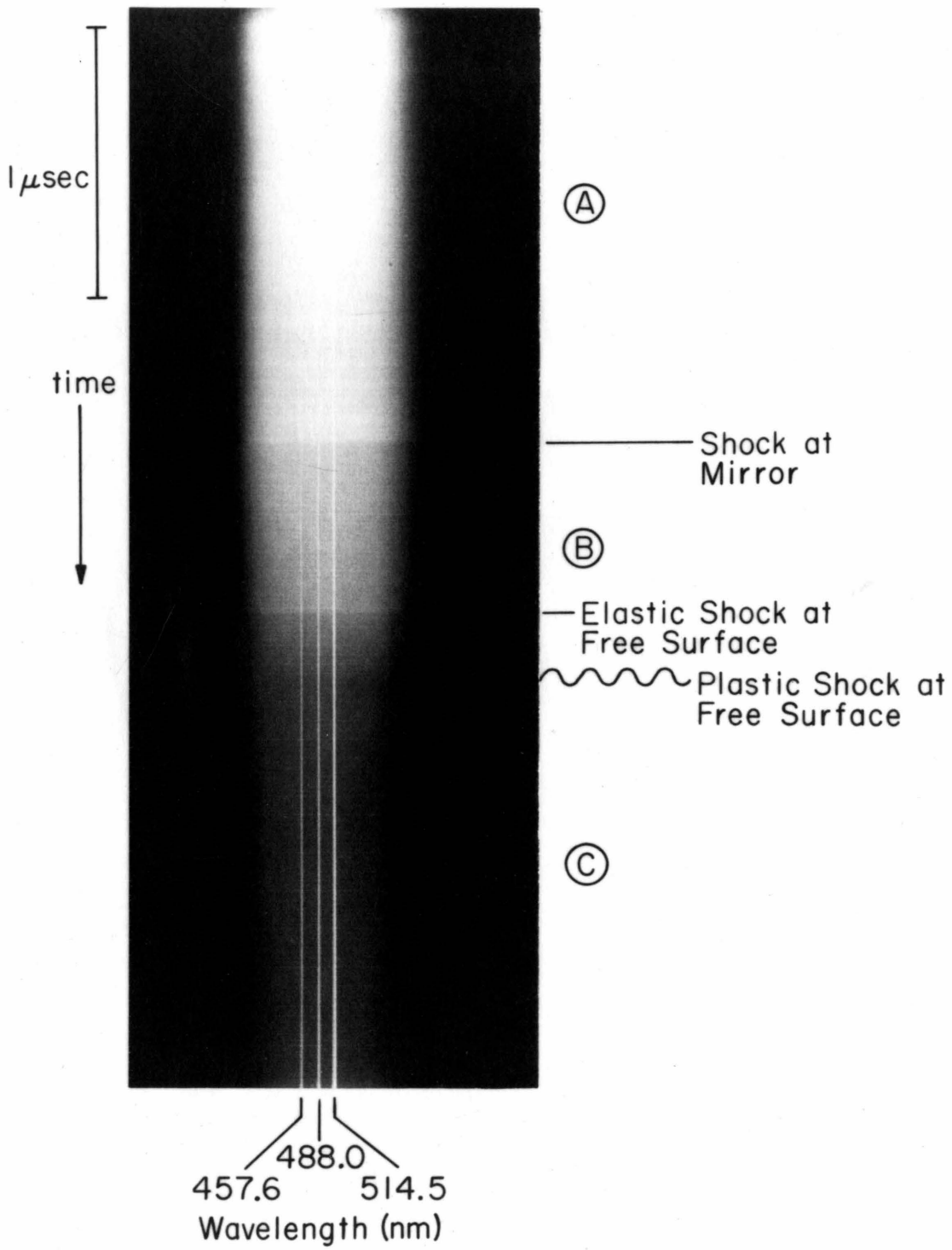
1 μsec
time
A
Shock at Mirror
B
Elastic Shock at Free Surface
Plastic Shock at Free Surface
C
488.0
457.6
514.5
Wavelength (nm)

material is greater than that of the unshocked but no spectral features are apparent. This may be an intrinsic effect due to compression of MgO to 465 kbar, or it may be due to scattering off of numerous shock induced imperfections in the crystal. In the absence of any other data we favor the latter cause.

There are two discontinuities in rapid succession at the end of region B. These are attributed to arrivals of the elastic and plastic shocks at the free surface of the sample. This can be expected to degrade the surface sufficiently to yield a substantial (featureless) decrease in light transmission. From the time separation between mirror encounter and free surface emergence we can calculate the shock velocities to be 8.0 $\pm$ 0.5 mm/$\mu$sec and 9.9 $\pm$ 0.1 mm/$\mu$sec for the plastic and elastic waves, respectively. This is very good agreement with the values of Ahrens (4), especially in view of the rather diffuse nature of the second arrival in Figure 8.

In region C of the record we have the spectrum of MgO while unloading from 465 kbar. There is no change apparent across this region indicating that no changes in the

opacity of periclase occur during the first 1 1/2 microseconds of unloading. This is sufficient time to permit complete unloading of the MgO back to the mirror (unless the low pressure shock wave reflected from the rear surface of the flyer plate interferes.) If color centers have been produced in this event they must be few in number, in some other spectral region or not yet be in their ground state. It is concluded that shock pressures greater than 465 kbar are required to produce substantial populations of color centers in periclase. Because of the qualitative nature of intensity measurements with the present system the term "substantial" just above cannot be more qualitatively defined.

C. Ruby Spectra

Although $Fe^{2+}$ is by far the most abundant of the transition metal ions in the mantle, its most intense crystal-field absorptions in most coordinations expected in the mantle are in the near infrared. This is a spectral region that cannot be studied by the present spectrographic system, so instead the effects of large compressions on the absorption spectrum of single crystal ruby

($Cr^{3+}$:$Al_2O_3$), which is in a spectral region accessible to the system, were studied in the hope that the behavior of $Fe^{2+}$ can be inferred from such data using the techniques of Chapter II. The present experiments span the range from 147 kbar to 530 kbar. The pressures attained are more than three times greater than the maximum attained in hydrostatic compression (5). Such measurements permit a determination of the local environment about the $Cr^{3+}$ impurities in the corundum ($Al_2O_3$) lattice. The data are presented below and discussed in light of the hydrostatic spectral studies and the recent Hugoniot measurements on sapphire (6).

The principle absorptions in ruby arise from $Cr^{3+}$ ion substituting in Al-sites in corundum. These sites are nearly octahedral with some trigonal distortion. In the pure octahedral field the $^4F$ ground state of $Cr^{3+}$ splits into $^4A_2$, $^4T_2$ and $^4T_1$. The observed absorptions correspond to the electronic transitions $^4A_2 \longrightarrow {}^4T_2$ at about 18,000 $cm^{-1}$ and $^4A_2 \longrightarrow {}^4T_1$ at about 25,000 $cm^{-1}$. The trigonal field splits the excited states ($^4T_2 \longrightarrow {}^4A_1 + {}^4E$ and $^4T_1 \longrightarrow {}^4A_2 + {}^4E$) by about 500 $cm^{-1}$ but this is too small (relative to the widths of the absorptions) to be

determined in the unpolarized spectra reported here. See Tanabe and Sugano (7) for a discussion of $Cr^{3+}$ spectra.

The effect of hydrostatic pressures up to 150 kbar on the spectra of ruby has been studied by Stephens and Drickamer (5). They found that Dq increased proportional to $1/r^5$ as r, the interatomic distance, decreased. This is exactly the behavior predicted for a point charge model. Since they measured the positions of both the $^4A_2 \longrightarrow {}^4T_2$ and $^4A_2 \longrightarrow {}^4T_1$ transitions up to 120 kbar they were also able to determine that one of the Racah parameters B decreases on compression approximately as $r^3$. (There is no model for predicting the change of B or C with interatomic distance.) From the polarization dependence of the spectra they found that the trigonal splitting of the $^4T_2$ and $^4T_1$ states increased on compression for pressures over 60 kbar. The value extrapolated from 120 to 150 kbar would be about 950 - 1000 $cm^{-1}$.

The samples studied here were single crystal pink ruby (0.5% Cr: $Al_2O_3$) discs 6 mm thick and 22 mm in diameter with the crystallographic c-axis at 60° to the flat surfaces. They were flat to one wave and polished with one surface aluminized. Fabrication was done by the vendor,

Union Carbide, Crystal Products Division. A transmission spectrum of one of the samples is shown in Figure 9.

Spectra were measured at three values of normal stress, one below the elastic limit (147 kbar) and two above (430 kbar and 530 kbar). The data obtained from these three experiments are summarized in Table 2. Figure 10 shows a typical photographic record. These photographic negatives were digitized and stored on tape by the Image Processing Laboratory of the Jet Propulsion Laboratory and then computer processed to reduce the noise level.

The density traces across the film are differenced to show the change in the absorption between two traces. If the earlier trace is subtracted from the later one, absorption maxima in the low pressure region appear as negative features, while those in the high pressure region will be positive features. Data from all three shots are given in the Appendix.

In order to evaluate the results summarized in Table 2 one must distinguish between absroptions in the volumes ahead of and behind the shock front, on the one hand, and at interfaces such as the internal mirror, the shock front and

Figure 9

Absorption spectrum of pink ruby ($Al_2O_3$:0.05% $Cr_2O_3$) at zero pressure.

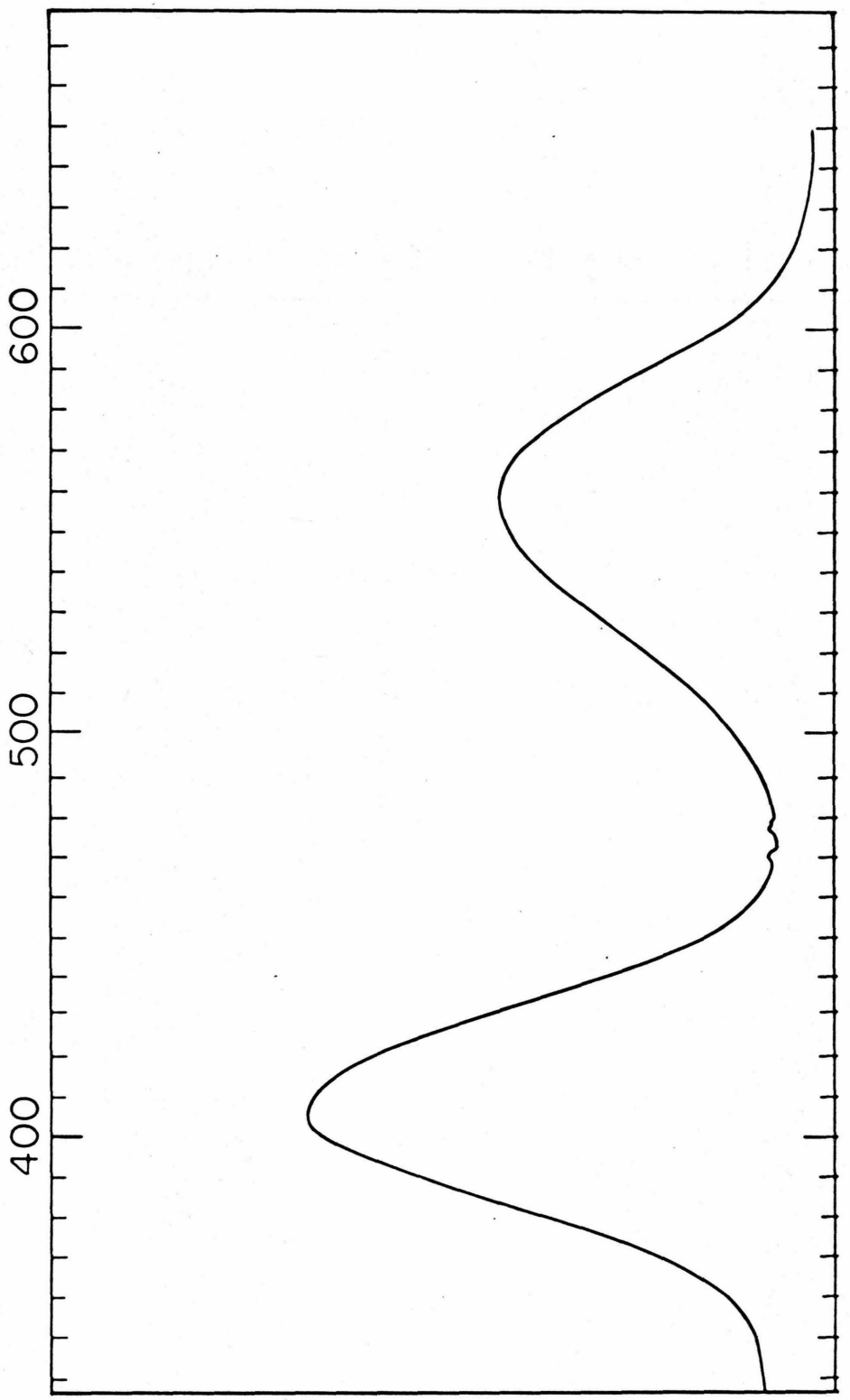
600
500
400

TABLE 2 RUBY DATA

| Pressure (kbar) | 147 ± 3 | 430 ± 10 | 530 ± 10 |
|---|---|---|---|
| Absorption | (446 ± 3) | | (411 ± 12) |
| Peaks | [22420 ± 150] | | [24330 ± 690] |
| (λ, nm) | (478 ± 5) | (460 ± 10) | |
| [E, $cm^{-1}$] | [20940 ± 210] | [21740 ± 420] | |
| | (524 ± 10) | | |
| | [19080 ± 250] | | |
| | (581 ± 4) | | |
| | [17210 ± 120] | | |

Figure 10

Absorption spectrum of pink ruby shocked to 430 kbar. Raw data (digitized from photographic negative). The four vertical lines are the emission lines of a pulsed argon laser used for wavelength calibration. The density of the negative on two scans is plotted on the right.

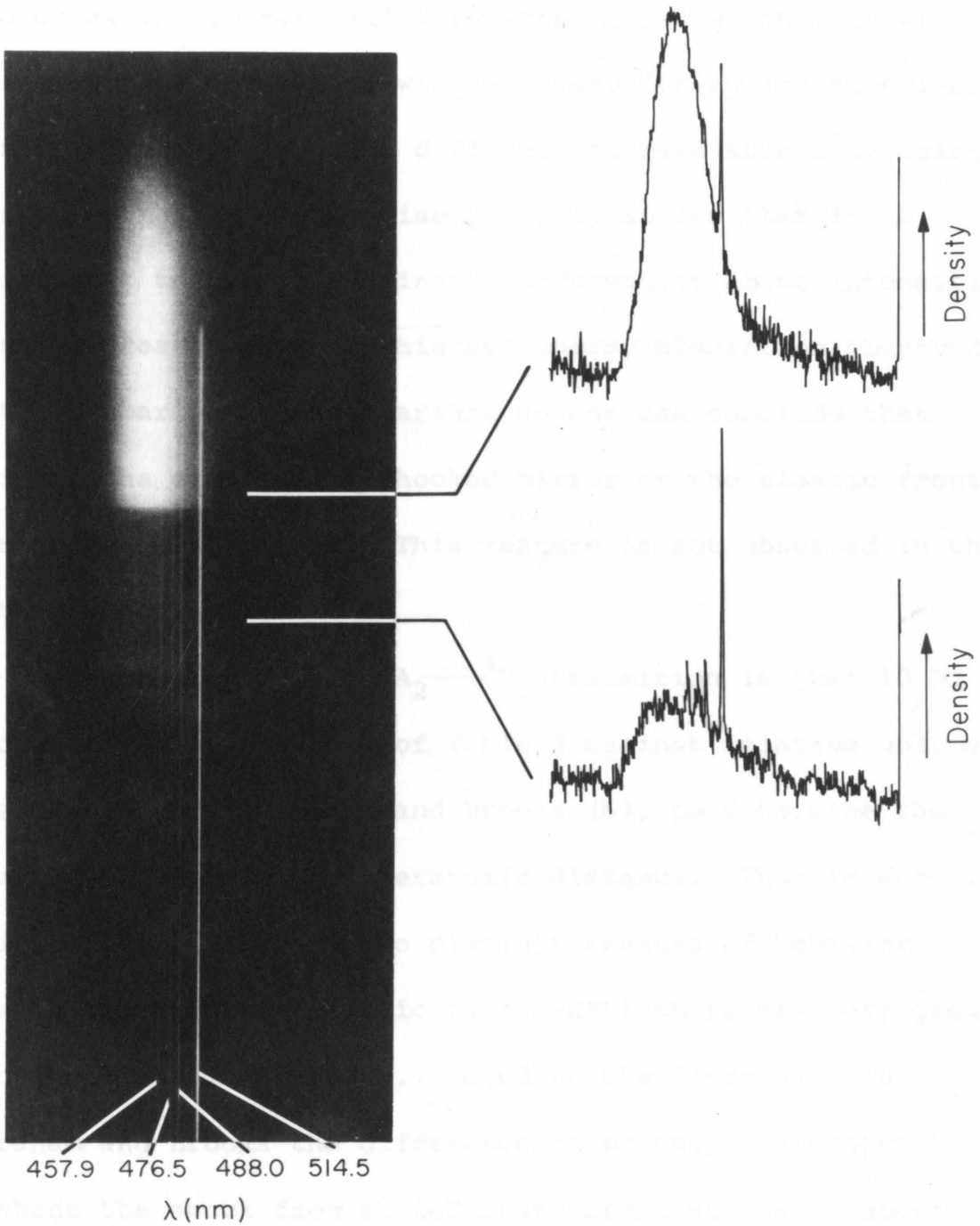
Density
Density
457.9
476.5
488.0
514.5
λ(nm)

the free surface, on the other. In principle, this is easy to do as the former will have intensities which vary with time whereas the latter will not vary during the experiment. In practice, it is often difficult to make such a decision because the signal-to-noise ratio is so low that it is difficult to obtain meaningful information about intensities. In the present case the highest energy absorption observed at 147 kbar was time invariant so one can conclude that either the elastically shocked mirror or the elastic front produces this feature. This feature is not observed in the other spectra.

The energy of the $^4A_2 \longrightarrow {}^4T_2$ transition is just 10 Dq so we can plot the data of Table 2 against relative volume, as determined by Graham and Brooks (6), to determine the variation of Dq with interatomic distance. This is done in Figure 11. There are two distinct regions of behavior. Below the Hugoniot elastic limit (HEL) there are very great non-hydrostatic stresses. Based on the discussion in Graham and Brooks the difference in principle stresses behind the shock from at 147 kbar normal stress is about 90 kbar. It is to be expected, therefore, that the local

Figure 11

Observed absorption bands and the variability of Dq with R for shock-loaded rubies. Hydrostatic spectral data of Stephens and Drickamer (5) is shown for comparison. The diagonal line is the variation of Dq with R predicted using the point charge model of Chapter II.

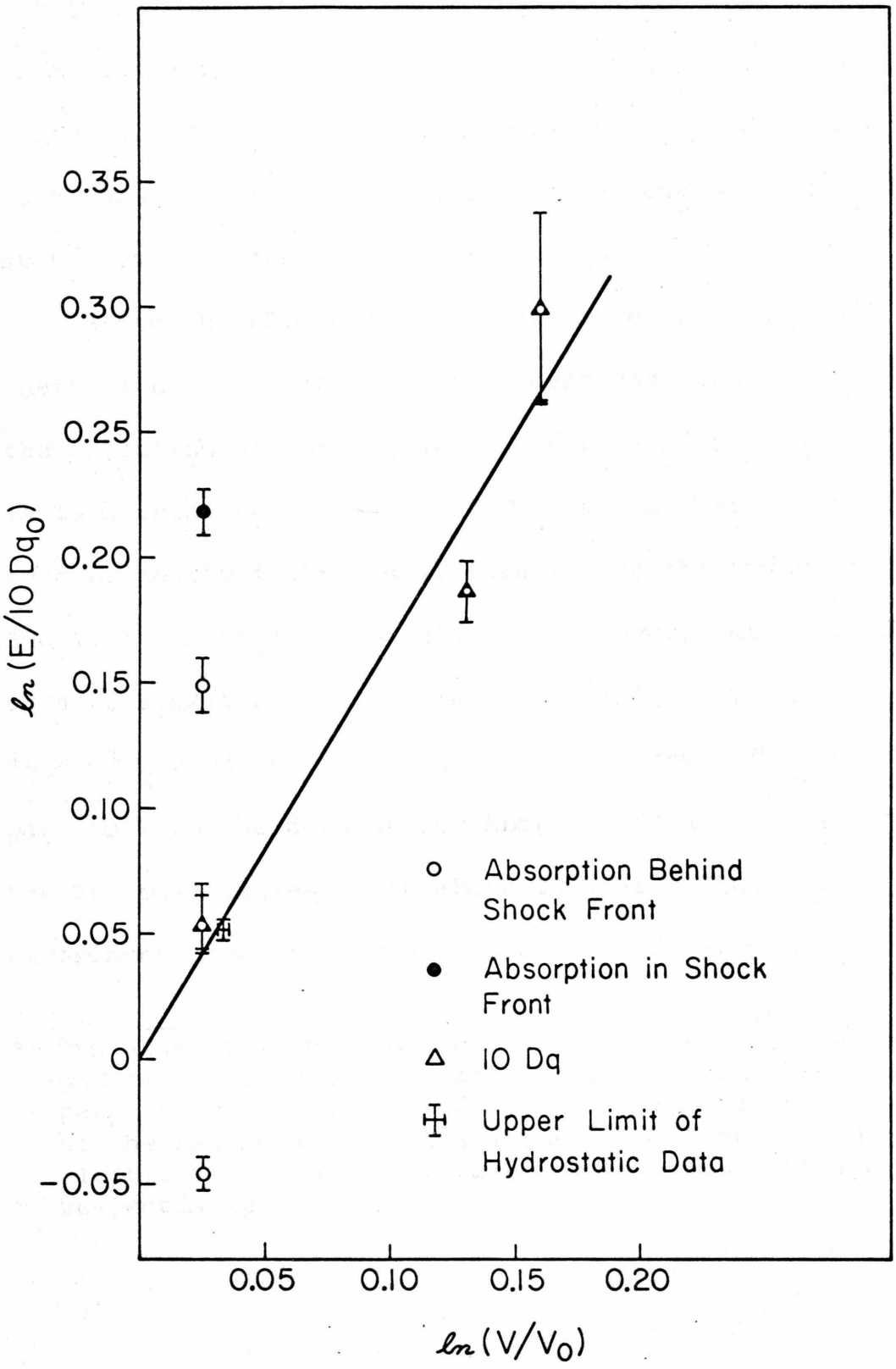
0.35
0.30
0.25
0.20
0.15
0.10
0.05
0
-0.05
0.05
0.10
0.15
0.20
ln (E/10 Dq0)
ln (V/V0)
Absorption Behind Shock Front
Absorption in Shock Front
10 Dq
Upper Limit of Hydrostatic Data

symmetry about the $Cr^{3+}$ ions to be considerably distorted from the octahedral case. This is exactly what is found below the HEL. The absorption due to $^4A_2 \longrightarrow {}^4T_2$ is split by more than 3730 $cm^{-1}$, almost four times the value from hydrostatic experiments.

Above the HEL we find a very different situation. Now there is only one absorption discernable* indicating that the splitting of the $^4T_2$ state due to non-octahedral fields is less than about 800 $cm^{-1}$. This means that the strain must be nearly isotropic at stresses on the order of 400-500 kbar, and therefore that the non-hydrostatic component of stress must be fairly small. If the splitting of $^4A_2 \longrightarrow {}^4T_2$ band is linear in the shear stress then by comparison with the data at 147 kbar the shear stress above the HEL must be less than about 20 kbar. Thus these experiments confirm, by a completely different method, the

---

* The absorption due to the elastically shocked region is not discernable because at any given moment less than 20 percent of the material behind the elastic shock is ahead of the second shock. The shock velocities for the elastic and second waves are about 11 and 9 mm/sec, respectively.

conclusions of Graham and Brooks (5) that sapphire loses most of its shear strength when shocked above the HEL. This experimental technique, with improved accuracy, has great potential as an "internal strain gauge" for detecting anisotropic strains in shock studies.

The measured value of Dq can be compared with that predicted by a point charge model assuming that the local compressibility about the $Cr^{3+}$ ion is equal to the bulk compressiblility of its host $Al_2O_3$. For a perfect octahedron such a model predicts that Dq should be proportional to $V^{-5/3}$ where V is the molar volume of sapphire. Stephens and Drickamer (5) found that this model worked very well for hydrostatic compression up to 150 kbar (3.5 precent compression). The present results demonstrate the usefulness of the model to volume compressions of nearly 15 percent. It is not possible, from these data, to determine the variation of the Racha parameters in ruby at these large compressions because the spectrograph could not follow the position of the $^4A_2 \longrightarrow {}^4T_1$ transition into the shocked region as a result of the spectral sensitivity of the streak camera photocathode.

REFERENCES

(1) H. G. David and A. H. Ewald, Photographic observations on shock waves in liquids. Austral. J. Appl. Sci. 11, 317-320 (1960).

(2) D. D. Preonas and H. F. Swift, A high-intensity point light source. 9th Internat. Cong. High-speed Photog., Denver, 1970.

(3) W. B. Gager, M. J. Klein, and W. H. Jones, The generation of vacancies in MgO single crystals by explosive shock. Appl. Phys. Letters 5, 131-132 (1964).

(4) T. J. Ahrens, High-pressure electrical behavior and equation of state of magnesium oxide from shock wave measurements. J. Appl. Phys. 37, 2532-2541 (1966).

(5) D. R. Stephens and H. G. Drickamer, Effect of pressure on the spectrum of ruby. J. Chem. Phys. 35, 427-429 (1961).

(6) R. A. Graham and W. P. Brooks, Shock-wave compression of sapphire from 15 to 420 kbar. The effects of large anisotropic compressions. J. Phys. Chem. Solids 32, 2311-2330 (1971).

(7) Y. Tanabe and S. Sugano, On the absorption spectra of complex ions. III. The calculation of the crystalline field strength. J. Phys. Soc. Japan 11, 864-877 (1956).

# V. BEHAVIOR OF IRON IN THE EARTH'S LOWER MANTLE

Iron is an important contributor to a number of controversies about the properties of the earth's lower mantle. The amount of iron has been the subject of much discussion for several years (1-4), and this discussion depends critically on the spin-state of $Fe^{2+}$ in the lower mantle. In addition, many of the physical properties of the lower mantle such as thermal conductivity (5, 6) and seismic parameters will depend on the spin-state of $Fe^{2+}$. It is the purpose of the present work to assess the possible effects of low-spin $Fe^{2+}$ in the earth's lower mantle. The presence and behavior of low-spin $Fe^{2+}$ in this region will depend on the transition-metal nature of $Fe^{2+}$, that is, on crystal field effects.

In order to predict crystal field effects on minerals in the mantle we must first know three things: 1) what minerals are likely to contain ferrous iron in the mantle and what the spin state of that iron will be, 2) what the response of these minerals is to high pressures, and 3) the effects of compression on the parameters used to describe the crystal fields. However, before considering

these points in turn let us first consider the pyrolite model proposed by Ringwood (7).

A. Ringwood's Pyrolite

Ringwood's pyrolite model is summarized in Table 1. The exact details of the model, such as percentages of various phases, are not so important to our discussion as are its gross features, such as phases present and approximate compositions. The results would not be greatly different if discontinuities moved slightly or if compositions varied by a few percent. For present purposes the salient feature is the appearance of several crystal structures not familiar from low pressure silicate chemistry.

Below 650 km all of the proposed structures have Si in six-coordination however, the coordination of (Mg, Fe) is variable.* In the ilmenite structure (Mg, Fe) would also be in six-coordination in a nearly perfect octahedron. (There will be some slight trigonal distortion.) This is the most usual coordination of (Mg, Fe) in the upper mantle.

---

* In this section it is assumed that there is always solid solution between $Mg^{2+}$ and $Fe^{2+}$. In the next section, the effects, as well as the necessity, of removing this simplification will be discussed.

TABLE 1

RINGWOOD's (1970) pyrolite mantle.

| | | |
|---|---|---|
| 700 - 1050 km (240 - 400 kb) $\rho_o$ = 3.99 | | |
| | 55% $(Mg,Fe)\ SiO_4$ | (strontium plumbate structure) |
| | 36% $(Mg,Fe,Cr,Al)\ (Si,Al)\ O_3$ | (ilmenite structure) |
| | $6\frac{1}{2}\%$ $CaSiO_3$ | (perovskite structure) |
| | $2\frac{1}{2}\%$ $NaAlSiO_4$ | (calcium ferrite structure) |
| Below 1050 km (greater than 400 kb) | | |
| | $(Ca,Mg,Fe)\ SiO_3$ | (perovskite structure) |
| | $NaAlSiO_4$ | (calcium ferrite structure) |
| | $(Mg,Fe)\ (Al,Cr)_2\ O_4$ | (calcium ferrite structure) |
| | $(Mg,Fe)\ SiO_4$ | (calcium ferrite structure) or (potassium nickel fluoride structure) |

In the $Sr_2PbO_4$ structure the (Mg, Fe) will be in the Sr site illustrated in Figure 1a. The site is seven-coordinated with $C_{2v}$ symmetry. In the $CaFe_2O_4$ structure the (Mg, Fe) must go into two sites. In the Fe site (Mg, Fe) is six-coordinated nearly in an octahedron but in the Ca site it is eight-coordinated (Figure 1b) with $C_{2v}$ symmetry. In the $K_2NiF_4$ the (Mg, Fe) will be in the K site (Figure 1c), a nine-coordinated site with $C_{4v}$ symmetry. In the perovskite structure (Mg, Fe) will be in the 12-coordinated Ca site (Figure 1d) with $O_h$ symmetry. For the purposes of these calculations, the silicate structures are taken as identical to the type structure except for a scale factor determined by density. Where the type structure has (Fe, Mg) and Si in identical sites the Fe-O distance is taken so that Si-O is 1.78 Å as in stishovite (8) and the mean of Fe-O and Si-O is the distance given from the type structure.

It is assumed that all compressions are isostructural and that Fe/(Fe + Mg) = .2. The bulk modulus K was taken to be the mean predicted after Anderson (9) and Anderson and Anderson (10). dK/dP was taken to be 4 in a Birch-Murnaghan equation. As we shall see later, changing these

Figure 1

Coordination polyhedra for $Fe^{2+}$ in proposed mantle minerals. a) $Sr_2PbO_4$ structure, b) $CaFe_2O_4$ structure, c) $K_2NiF_4$ structure, and d) perovskite structure.

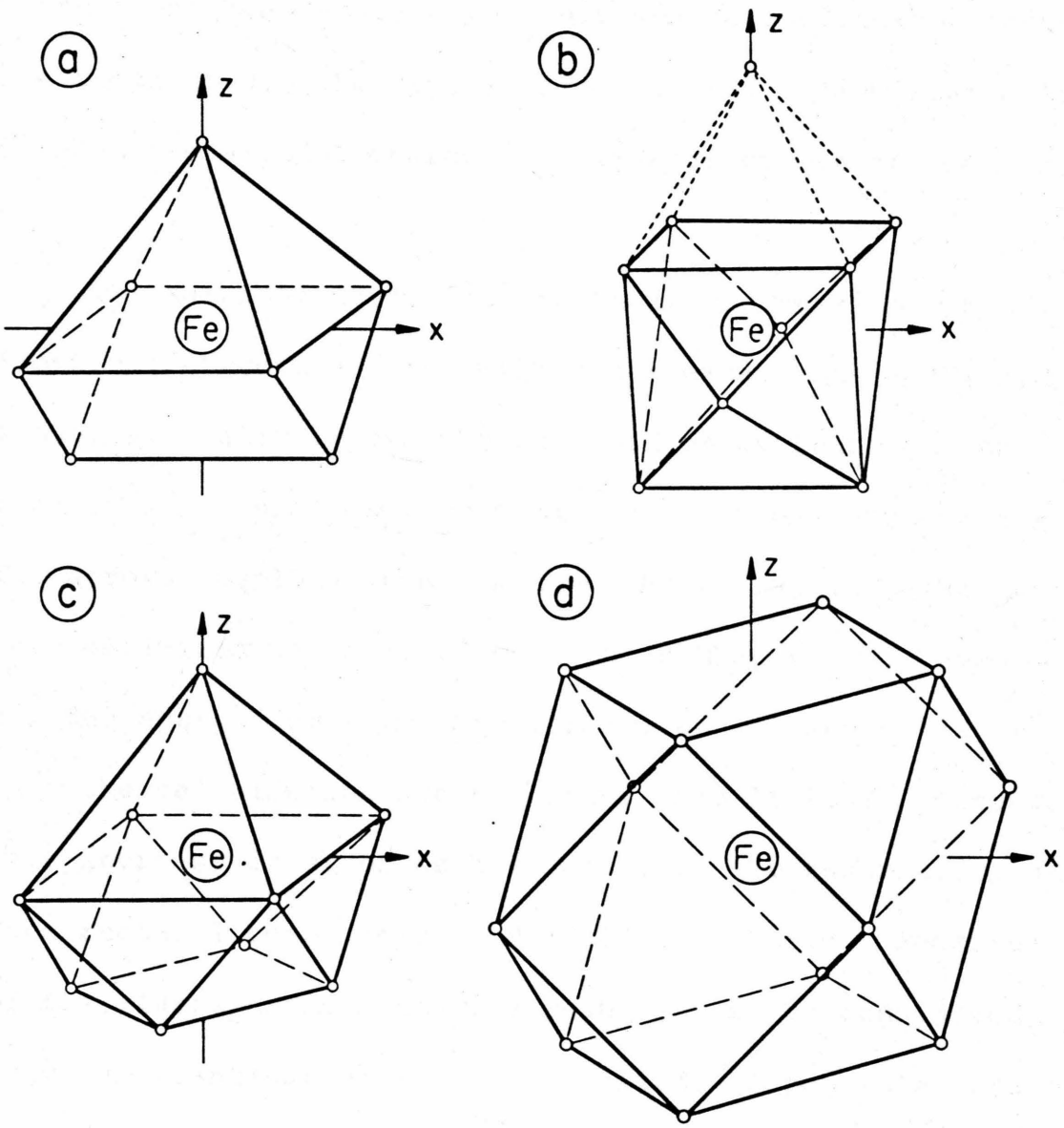
a
z
Fe
x
b
z
Fe
x
c
z
Fe
x
d
z
Fe
x

elastic properties slightly does not affect the conclusion. A completely ionic model with actual ions replaced by point charges has been assumed and only nearest neighbor effects are considered. The crystal field energies have been calculated using a point charge technique described in Chapter II.

The assumptions of isostructural compression and of identical structures are, with minor exceptions mentioned above, virtually impossible to avoid or evaluate due to lack of structural data on silicates in these strucutures. The errors involved in estimating the radial integrals were estimated at about 10 percent in Chapter II. When all the sources of error are considered, it seems likely that the calculations are no better than 15 to 20 percent. This increase in error is due mainly to the assumptions of isostructural compression and ideal structures. Because of this large uncertainty the results must be considered only semiquantitative and the magnitude of possible errors must be considered in the subsequent discussion. However, one can still draw some important conclusions.

The results of the above calculations are given in Tables 2 and 3. Here the one-electron energy levels of $Fe^{2+}$ ions in various structures at zero pressure and at various levels in the mantle are shown.

Before beginning a discussion of chemical fractionation of $Fe^{2+}$ and $Mg^{2+}$ in the lower mantle, a brief digression is in order, to evaluate the relative importance of CFSE's in $Fe^{2+}$ distribution in minerals. Such a distribution will depend on the free energy of the minerals concerned and therefore, at some pressure and temperature on the enthalpy, the entropy and the specific volume. The CFSE contributes to the enthalpy while the ionic radius contributes to both the enthalpy (largely through its effect on CFSE) and the specific volume. In order to have a complete knowledge of the system the effect of entropy must also be considered. However, the accuracy of the predictions of CFSE and specific volume is not sufficient to warrant treating the free energy as such. It is probably safe to assume that if both CFSE and radius arguments favor $Fe^{2+}$ enrichment in some phase such enrichment

TABLE 2

Energy levels of 3d orbitals of $Fe^{2+}$ ions in $Mg_{1.6}Fe_{0.4}SiO_4$ in proposed high pressure phases. Where "$z^2$" and "$x^2-y^2$" are indicated these orbitals interact and "$z^2$" indicates the combination which reduces to $z^2$ when interaction energy is zero. Energy units are $cm^{-1}$.

| E(0 km) | E(700 km) | E(1050 km) | Orbital |
|---|---|---|---|
| $Sr_2PbO_4$ structure ($\rho_o$ = 4.09 gm/cm$^3$) | | | |
| 4970 | 5650 | 5980 | xy |
| 1350 | 1450 | 1520 | xz |
| 1050 | 1160 | 1280 | "$x^2-y^2$" |
| -1760 | -1930 | -2170 | "$z^2$" |
| -5590 | -6320 | -6610 | yz |
| $K_2NiF_4$ structure ($\rho_o$ = 4.3 gm/cm$^3$) | | | |
| E(0 km) | E(1050 km) | E(1250 km) | Orbital |
| 2960 | 3950 | 4070 | $z^2$ |
| 360 | 320 | 310 | xz,yz |
| 160 | 660 | 730 | xy |
| -3820 | -5240 | -5410 | $x^2-y^2$ |
| $CaFe_2O_4$ structure ($\rho_o$ = 4.3 gm/cm$^3$) | | | |
| E(0 km) | E(1050 km) | E(1250 km) | Orbital |
| 8-site | | | |
| 1440 | 1640 | 1670 | yz |
| 1250 | 1670 | 1760 | xz |
| 570 | 720 | 750 | xy |
| -310 | -490 | -530 | "$x^2-y^2$" |
| -2960 | -3530 | -3660 | "$z^2$" |
| 6-site | | | |
| 7620 | 10670 | 11440 | $x^2-y^2,z^2$ |
| -5080 | -7120 | -7630 | xy,yz,xz |

TABLE 3

Energy levels of 3d orbitals of $Fe^{2+}$ ions in $Mg_{0.8}Fe_{0.2}SiO_3$ in proposed high pressure phases. Energy units are $cm^{-1}$.

Ilmenite structure ($\rho_o$ = 3.87 gm/cm$^3$)

| E(0 km) | E(700 km) | E(1050 km) | Orbital |
|---|---|---|---|
| 4329 | 4610 | 5490 | $x^2-y^2, z^2$ |
| -2890 | -3070 | -3660 | xy, yz, xz |

Perovskite structure ($\rho_o$ = 4.45 gm/cm$^3$)

| E(0 km) | E(1050 km) | E(1250 km) | Orbital |
|---|---|---|---|
| 1520 | 1820 | 1890 | xy, yz, xz |
| -1020 | -1210 | -1260 | $x^2-y^2, z^2$ |

will occur. To estimate the size of CFSE terms required to produce appreciable fractionation consider the spectra of olivine and orthopyroxene as given by Burns (13). The difference in CFSE between $M_1$ and $M_2$ is about 100 $cm^{-1}$; no fractionation is observed between these sites. On the other hand for orthopyroxenes the CFSE's of $M_1$ and $M_2$ differ by about 590 $cm^{-1}$ ($M_2 > M_1$)* and there is appreciable fractionation between sites in the expected sense. On the other hand, the behavior of $Fe^{2+}$ in garnet-olivine combinations (considerable $Fe^{2+}$ enrichment in garnet), must be the effect of ionic radius since the CFSE's of garnet and olivine $M_1$ are identical. ($Fe^{2+}$ is 0.05 Å larger than the site available in forsterite.)

From the point of view of chemical fractionation of $Fe^{2+}$ relative to $Mg^{2+}$ the results are recast in Table 4. Between 650 km and 1050 km, $Fe^{2+}$ shows a large (about 9 kcal/mole) crystal field stabilization energy (CFSE) preference for the $Sr_2PbO_4$ structure relative to that of ilmenite. This is large enough as to be valid as discussed

---

* 1.68 kcal/mole (cf., 1.5 kcal/mole calculated by Ahrens (35)).

TABLE 4

Parameters affecting distribution of $Fe^{2+}$ in the mantle. The dashed line separates structures found above and below the 1050 km discontinuity.

| Structure (coord.) | CFSE[a] | | r[b] | I.R.[c](Fe) | I.R.[c](Mg) |
|---|---|---|---|---|---|
| | ($cm^{-1}$) | (kcal/mole) | (Å) | (Å) | (Å) |
| $Sr_2PbO_4$ (7) | 6610 | 18.9 | 2.16 | (2.15) | (2.09) |
| Ilmenite (6)[d] | 3660 | 10.5 | 2.17 | 2.15 | 2.09 |
| $CaFe_2O_4$ (6) | [8690] | [24.9] | [1.88] | [1.93] | 2.09 |
| $CaFe_2O_4$ (8) | 3530 | 10.1 | 2.09 | 2.28[e] | 2.27[e] |
| $K_2NiF_4$ (9) | 5240 | 15.0 | 2.23 | (2.28)[e] | (2.27)[e] |
| Perovskite (12) | 1210 | 3.5 | 2.40 | (2.28)[e] | (2.27)[e] |

a. Crystal field stabilization energy.

b. Metal-oxygen distance

c. Sum of radii of $O^{2-}$ and $M^{2+}$ from Shannon and Prewitt (11) except as otherwise noted. Parentheses indicate value for coordination other than that in high pressure phase.

d. Square brackets indicate value for low spin $Fe^{2+}$.

e. Interatomic distance for eight coordination in pyrope-almandine garnets (12).

above. However, trigonal distortion of the (Fe, Mg) site in ilmenite which will stabilize that site has been ignored so the effect may be smaller than calculated. The size of the sites involved is virtually identical so there will be no preference on that account. So one should expect $Fe^{2+}$ to concentrate in the $Sr_2PbO_4$ structure relative to the ilmenite structure.

Below 1050 km Ringwood's model is less specific and $Fe^{2+}$ partition in two different models must be considered: $CaFe_2O_4$ structure + perovskite structure and $K_2NiF_4$ structure + perovskite structure. In either case $Fe^{2+}$ should avoid the perovskite structure because of the very small CFSE. Even a large non-cubic distortion of the dodecahedral site in the perovskite structure should not have enough effect to change this result. In the two other phases $Fe^{2+}$ will have a very large preference for the six-coordinated site in the $CaFe_2O_4$ structure relative the $K_2NiF_4$ structure and the eight-coordinated site in $CaFe_2O_4$. Furthermore, the $Fe^{2+}$ will be spin-paired according to the criteria of Griffiths (14), producing a good fit in ionic size. The obvious conclusion is that $Fe^{2+}$ will be spin-paired in the lower mantle if the assignment of the

$CaFe_2O_4$ structure is valid. Indeed if crystal field effects in $Fe^{2+}$ alone were the deciding factor, $(Mg,Fe)SiO_4$ in the lower mantle will not be in the $K_2NiF_4$ structure but must be in the $CaFe_2O_4$ structure.

The effects of $Fe^{2+}$ on possible radiative transfer in the mantle can be evaluated by considering transitions between the states in Tables 2 and 3. These transitions from the ground state to higher energy states occur with absorption of light of the appropriate energy. The theory of radiative transfer (5) requires low absorbance in the region of the spectrum of interest for radiative transfer. Figure 2 has some of the pertinent information shown for three levels in the mantle. The spectra are at very best only educated guesses based on these calculations. The width of the absorption bands and the intensities are arbitrary. The high temperatures in the mantle will lead to widening of absorption bands relative to low termperatures and the high pressures may lead to increase in intensity (15).

It is difficult to predict, with any certainty, the behavior of charge transfer bands with pressure in the mantle. At low pressures they are found in the ultraviolet

Figure 2

Factors governing radiative transfer in the mantle at three depths. At each depth (a) shows the positions of possible transitions from Tables 3 and 4, (b) shows a schematic absorption spectrum due only to $Fe^{2+}$ absorption, and (c) shows the region of the spectrum of interest for radiative transfer as the unshaded portion.

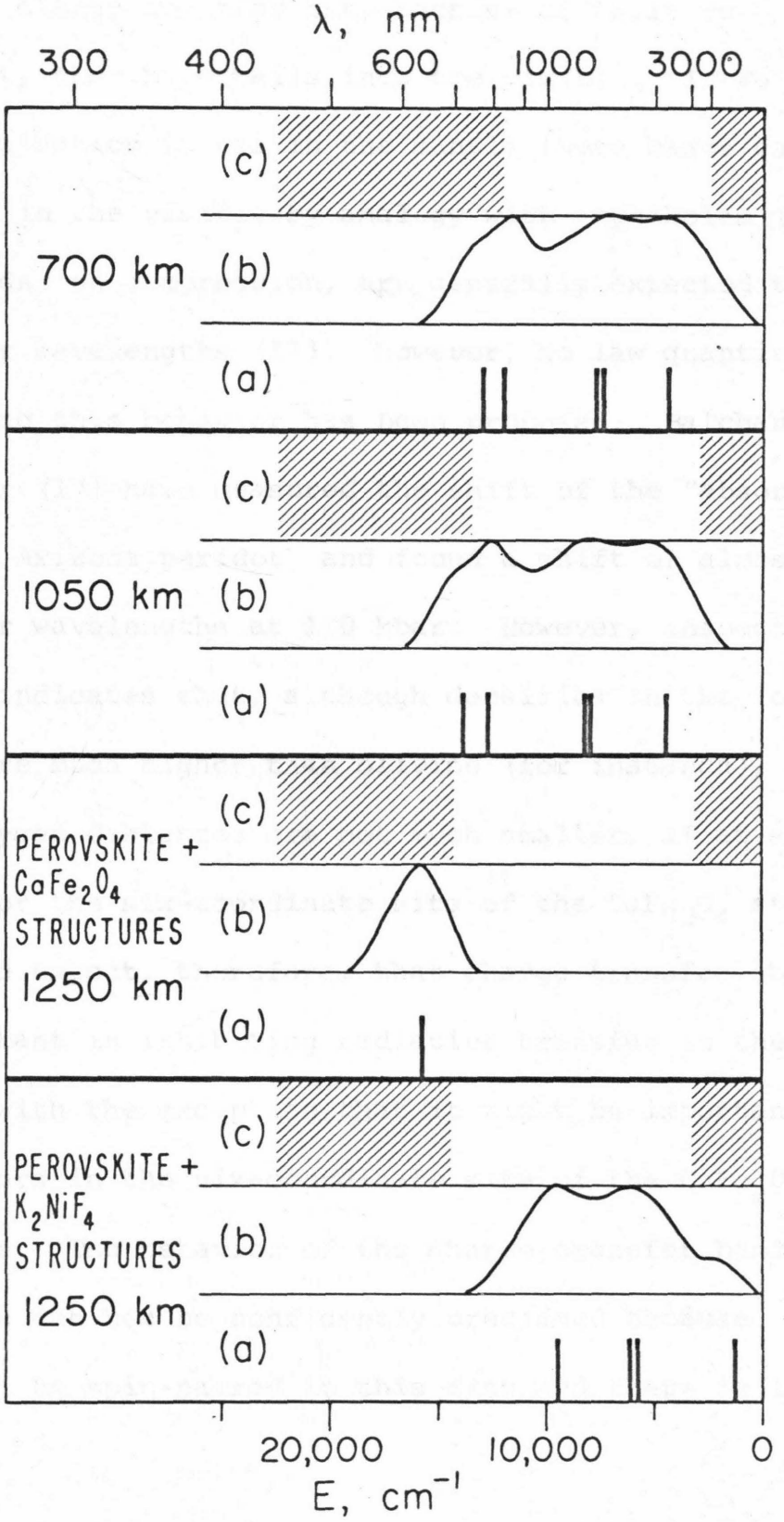
λ, nm
300
400
600
1000
3000
(c)
700 km (b)
(a)
(c)
1050 km (b)
(a)
(c)
PEROVSKITE + $CaFe_2O_4$ STRUCTURES
(b)
1250 km
(a)
(c)
PEROVSKITE + $K_2NiF_4$ STRUCTURES
(b)
1250 km
(a)
20,000
10,000
0
E, $cm^{-1}$

for Fe-O charge transfer but, because of their very great intensity, they have tails into the visible. If Fe occurs in two oxidation states in the mantle these bands can be expected in the visible by analogy with amphiboles (16). Such bands, on compression, are generally expected to move to longer wavelengths (17). However, no law quantitatively describing this behavior has been proposed. Balchan and Drickamer (17) have measured the shift of the "absorption edge" in Arizona peridot and found a shift of almost 10% to longer wavelengths at 150 kbar. However, inspection of Table 5 indicates that, although densities in the lower mantle are much higher than olivine (for instance), the metal-oxygen distances are not much smaller, if at all, except for the six-coordinate site of the $CaFe_2O_4$ structure. One would expect, therefore, that charge transfer should not be important in inhibiting radiative transfer in the lower mantle, with the exception that it might be important if $Fe^{2+}$ occurs in the six-coordinate site of the $CaFe_2O_4$ structure. The behavior of the charge transfer bands in that case can not be confidently predicted because the iron will be spin-paired in this site and there is little

data to extrapolate. However, Strens data on gillespite (18) indicate that for a triplet ground state the charge transfer bands are well into the ultraviolet.

It is apparent, even allowing for the possible errors in these calculations, that radiative transfer will be effectively blocked between 650 km and 1050 km by absorption due primarily to $Fe^{2+}$ in the $Sr_2PbO_4$ structure. Below 1050 km both models will permit radiative transfer if charge transfer does not interfere with the $CaFe_2O_4$ structure model having a considerably larger radiative conductivity than $K_2NiF_4$ structure model.

Up to this point the pyrolite model does not contradict any of the known facts. However, when we calculate the seismic parameter ($\Phi = V_p^2 - 4/3\ V_s^2$) and density of such a model in the following sections we shall find that a pyrolite composition for the lower mantle is not possible.

B. Effect of $Fe^{2+}$ on the Mineralogy and Elasticity of the Lower Mantle

The mineralogy of $Fe^{2+}$ in the lower mantle will depend on the behavior of three ions — high-spin $Fe^{2+}$, low-spin

$Fe^{2+}$ and $Mg^{2+}$. These ions have radii of 0.77 Å, 0.61 Å,* and 0.72 Å, respectively (11). According to the Goldschmidt radius criterion for solid solubility (less than 15 percent difference in ionic radii) $Mg^{2+}$ and $Fe^{2+}$ (h.s.) can be expected to form solid solutions but $Mg^{2+}$ and $Fe^{2+}$ (l.s.) will not. The result will be that if $Fe^{2+}$ goes to a low spin ground state in the lower mantle another phase will appear. This possibility of a separate phase for $Fe^{2+}$ (l.s.) leads to several more potential phase changes in the lower mantle.**

---

* This radius is based both on sulfide crystal structure and on plots of ionic radius versus electronic configuration. $Fe^{2+}$(l.s.) has not been observed in eith oxides or fluorides, nor has nay other low-spin divalent first row transition metal ion been observed in oxides. However, the trivalent counterparts are known. Shannon and Prewitt plot ionic radius versus number of 3d electrons for these ions and find fairly smooth variability from $d^0$ to $d^6$ ($Co^{3+}$) and from $d^6$ to $d^{10}$ for the low-spin compounds. The values for low-spin $Fe^{2+}$ and $Co^{2+}$ deduced from sulfides behave in a very similar manner which lend some credence to the values given. However, a fairly large error must be attached to the radius of low-spin $Fe^{2+}$, perhaps about .03 Å.

** The Goldschmidt radius criterion is only a rule of thumb to which numerous exceptions can be cited. At high temperatures, especially, it is to be expected that a larger variability of size could be accommodated in a solid solution. However, pressure should act to decrease the range of ionic sizes that can be accommodated. The net result is that it is difficult to predict how the criterion should be modified for use in the lower mantle. It will be used here as stated above with the caveat that solid solution between $Fe^{2+}$(l.s.) and $Mg^{2+}$ cannot be ruled out unequivocally in the lower mantle.

The phases possible with $Mg^{2+}$ and $Fe^{2+}$ (h.s.) are taken to be those of Ringwood (7) so that there are two phase changes in which may occur in a pyrolite below 700 km, viz.,

$(Mg, Fe)_2SiO_4$ (strontium plumbate) $\longrightarrow$ (a)

$(Mg,Fe)_2SiO_4$ (calcium ferrite or potassium nickel fluoride)

$(Mg,Fe)SiO_3$ (ilmenite) $\longrightarrow$ $(Mg,Fe)SiO_3$ (perovskite) (b)

No denser phases have been proposed, but Johnson (19) and Whitcomb and Anderson (20) and others have detected evidence for at least five discontinuities in the lower mantle.

It has already been pointed out that $Fe^{2+}$ should prefer, in any such reactions, to spin-pair and enter the six-coordinate site of a calcium ferrite structure as $Mg^{VIII}(FeSi)^{Vi}O_4$. We shall also be interested here in other possible reactions involving low-spin $Fe^{2+}$. Three reactions are likely

$(Mg,Fe)_2SiO_4$ (strontium plumbate) $\longrightarrow$

$MgFe$(l.s.)$SiO_4$ (calcium ferrite) + $Mg_2SiO_4$ (c)

$MgFeSiO_4$ (calcium ferrite) + $Mg_2SiO_3$ $\longrightarrow$

$FeSiO_3$ (ilmenite) + $Mg_2SiO_4$ (d)

$FeSiO_3$ (ilmenite) + $Mg_2SiO_4$ $\longrightarrow$

FeO (low-spin, rock salt) + $2MgSiO_3$ (e)

The zero pressure density of these proposed minerals can be estimated using the radius of low-spin $Fe^{2+}$ and various density systematics. For FeO in the rock salt structure the relation $a_0 = 2(r(Fe^{2+}, \text{l.s.}) + r(O^{2-}))$ is used where $r(O^{2-})$ is taken as 1.38 Å which predicts the correct $a_0$ for MgO. Then $a_0$(FeO, l.s.) = 3.99 Å and $\rho_0$= 7.55 gm/cm$^3$. Using this value for $\rho_0$(FeO, l.s.) and the relation (7) that $\rho_0$ (ilmenite) is 3 percent less than that of the isochemical misture of oxides one finds $\rho_0(FeSiO_3)$ = 5.43 gm/cm$^3$.

For the density of $MgFeSiO_4$ in the calcium ferrite structure two systematic relations derived from unit cell volume-ionic radius systematics (Table 5) are used. The first is relation between unit cell volume (4 formula units) and the radius of the octahedral ion for nine compounds $M^{2+}X_2^{3+}O_4$ in the calcium ferrite structure. The six compounds with M = Ca define a straight line. If this line is projected to the arithmetic or geometric mean of $r(Si^{4+})^{VI}$ and $r(Fe^{2+}, \text{l.s.})^{VI}$ the probable unit cell volume of $Ca(FeSi)O_4$ is obtained. (Reid <u>et al.</u> (21) have shown that for $NaM^{3+}X^{4+}O_4$ compounds the distribution M and X in the octahedral sites are completely random so we are

TABLE 5. Volume Systematics for $M^{2+}X_2^{3+}O_4$ in Calcium Ferrite Structures

| Compound | Unit Cell Volume ($Å^3$) | $r_M^{VIII}$ (Å) | $r_X^{VI}$ (Å) | Reference |
|---|---|---|---|---|
| $CaFe_2O_4$ | 298 | 1.12 | .645 | (36), (37) |
| $CaV_2O_4$ | 288 | 1.12 | .640 | (38) |
| $CaCr_2O_4$ | 295 | 1.12 | .615 | (36) |
| $CaAl_2O_4$ | 264 | 1.12 | .530 | (39) |
| $CaSc_2O_4$ | 330 | 1.12 | .730 | (40) |
| $CaIn_2O_4$ | 350 | 1.12 | .790 | (41) |
| $MgSc_2O_4$ | 320 | .89 | .730 | (42) |
| $SrSc_2O_4$ | 350 | 1.25 | .730 | (43) |
| $SrIn_2O_4$ | 369 | 1.25 | .790 | (44) |

justified in treating the sites as equivalent even through they are crystallographically distinct. They also point out that the observed interatomic distances are very nearly equal to those derived by taking the mean of the two radii.) Next, it is noted that for the $MSc_2O_3$ and $MIn_2O_3$ compounds the difference in unit cell volume for M = Ca and M = Sr is a constant (20 $\mathring{A}^3$). The inference can be drawn therefrom that substitution of the $M^{2+}$ ion can be treated as a simple addition of a constant to the unit cell volume determined for $MX_2O_4$ for the same X. For $MgSc_2O_3$ this term is just 8 $\mathring{A}$/unit cell so the unit cell volume is 240 $\mathring{A}^3$ or 236 $\mathring{A}^3$ for the arithmetic or geometric mean radius, respectively. The mean (238 $\mathring{A}^3$) leads to a density of 4.76 gm/cm$^3$.

A second approach to the same data leads to a similar conclusion. The percentage difference between the density of the mixed isochemical oxides and the calcium ferrite structure depends on the radius of the eight-coordinated divalent ion. Although calcium ferrite structures are up to 8.6 percent denser than the oxides for large divalent ions, they are actually less dense for small ions such as $Mg^{2+}$. Using the value of 2.5 percent (from $MgSc_2O_4$) for $MgFeSiO_4$ the predicted density is 4.76 gm/cm$^3$. (In the

section on elastic properties the density of $Fe^{VIII}$(h.s.) $Fe^{VI}$(l.s.)$SiO_4$ in this structure will also be needed. Noting that in garnets $Mg^{VIII}$ and $Fe^{VIII}$(h.s.) are almost identical in size (12) one would predict a density of 5.63 $gm/cm^3$ for this phase. If, on the other hand one assumes it is 2.5 percent less dense than the oxides the density is 5.55 $gm/cm^3$; here the density $\rho_0 = 5.6 \pm 0.0$ $gm/cm^3$ is adopted.)

Although the potassium nickel fluoride and perovskite structures of most compounds should be considerably denser than the corresponding oxides, this will not be true for the low-spin ferrous minerals because the $Fe^{2+}$ must remain in six-coordination in order for the crystal field splitting of the 3d electronic energy levels to be sufficient to maintain the low-spin ground state. If the $Si^{4+}$ were to go to coordination greater than six these structures might include low-spin iron, but that is unlikely to occur below several megabars pressure.

Having determined the structure and uncompressed density of possible low-spin ferrous minerals in the mantle let us now consider their response to pressure, that is their bulk moduli and pressure derivatives, again employing systematics to predict behavior where there is no experimental data.

Plotting the compressibility against inverse molecular volume for compounds of the composition MO involving both zincite and rock salt structures (Figure 3), and ignoring, for the moment, the transition metal oxides (except MnO where $Mn^{2+}$ has five d-electrons in a half-filled shell so there are no crystal field effects) a linear relation is obtained for all mean atomic weights

$$\frac{1}{K(Mb)} = - 0.04 + .035V_{molec}(\mathring{A}^3)$$

whence one infers K(FeO, l.s.)=1.950 Mbar. However, the observed values of FeO, CoO and NiO fall well below the curve. These cations have, respectively, one, two and three d-electrons contributing to crystal field effects. There seems, therefore, to be an effect due to these electrons leading to a different behavior. Indeed, the four transition metal oxides fall very close to a straight line themselves:

$$\frac{1}{K(Mb)} = - 1.076 + .083V_{molec}(\mathring{A}^3).$$

Since low-spin $Fe^{2+}$ also has d-electrons contributing to crystal field effects (six of them) it seems preferable to use this relation to infer K(FeO, l.s.) = 4.160 Mb.

There is less data for sequioxides but the three oxides without crystal field effects ($Al_2O_3$, $Fe_2O_3$ and $SrTiO_3$) all

Figure 3

Compressibility-density systematics for oxides MO.

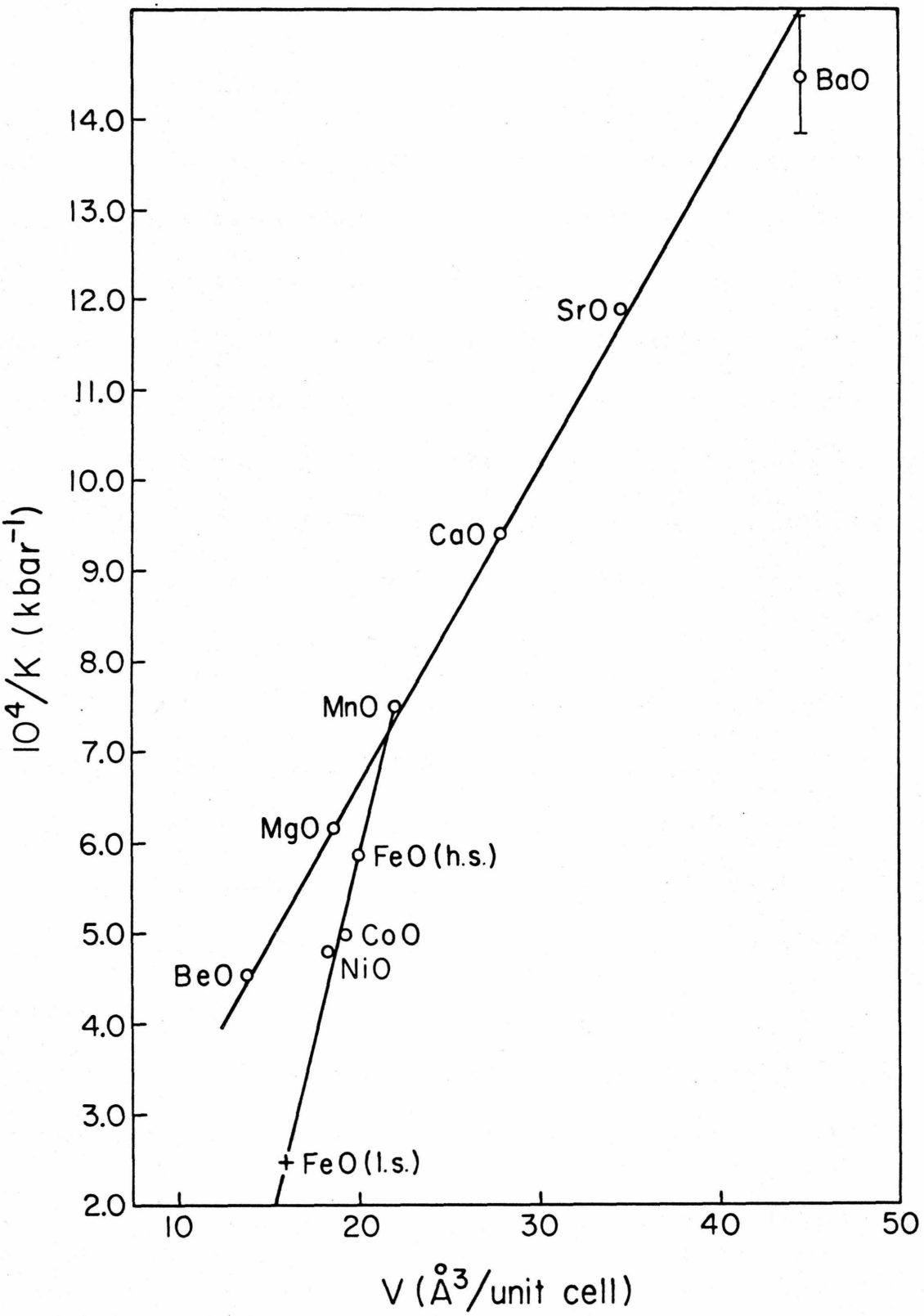
BaO
SrO
CaO
MnO
MgO
FeO (h.s.)
CoO
NiO
BeO
FeO (l.s.)
14.0
13.0
12.0
11.0
10.0
9.0
8.0
7.0
6.0
5.0
4.0
3.0
2.0
10
20
30
40
50
$10^4/K$ (kbar$^{-1}$)
V (Å$^3$/unit cell)

lie on the line:

$$\frac{1}{K(Mb)} = -0.04 + 0.01V_{molec}(\text{Å}^3)$$

but the oxide $Cr_2O_3$ with two ions with crystal field effects lies slightly below that line. The $Cr_2O_3$ and $Fe_2O_3$ points are too close to justify the inference of a crystal field line as with MO; furthermore the use of such a line derived for $M_2^{3+}O_3$ to predict behavior for $M^{2+}N^{4+}O_3$ crystal field effects would not appear, on the face of it, to be reasonable. Rather, take $\Phi_0$ for low-spin FeO and assume that the $\Phi_0$'s of the oxides are additive in a compound whose density is near that of the mixture of oxides (9). Using $\Phi_0$=82.2 (km/sec)$^2$ for stishovite (22) the predicted bulk moduli of $FeSiO_3$ and $MgFeSiO_4$ are 3.74 Mbar and 2.9 Mbar, respectively. (For $Fe_2SiO_4$ in the calcium ferrite structure K=3.1$\pm$ .025 Mbar).

In order to estimate the magnitude of dK/dP in the high pressure phases of the lower mantle we have used a relation between the density and (dK/dP-5/3). In Figure 4 we show the experimental data taken from Anderson et al. (23) and Davies and Anderson (24)*. There is considerable scatter

---

* Davies and Anderson's data is reduced from shock wave experiments and depends on the equation of state used by them. The values given by them for iron-rich compounds have been omitted for the present study.

Figure 4

Variation of dK/dP with density. + ultrasonic data (23), • static compression data (28), Δ shock wave data (24), O shock wave data for polymineralic rocks (24) (G = granite, E = eclogite), □ shock wave data for feldspar-rich systems (24) (N = albitite, K = microcline, N, NC = two points: oligoclase and anorthosite. Numbers by points indicate mean atomic weight ($\bar{M}$).

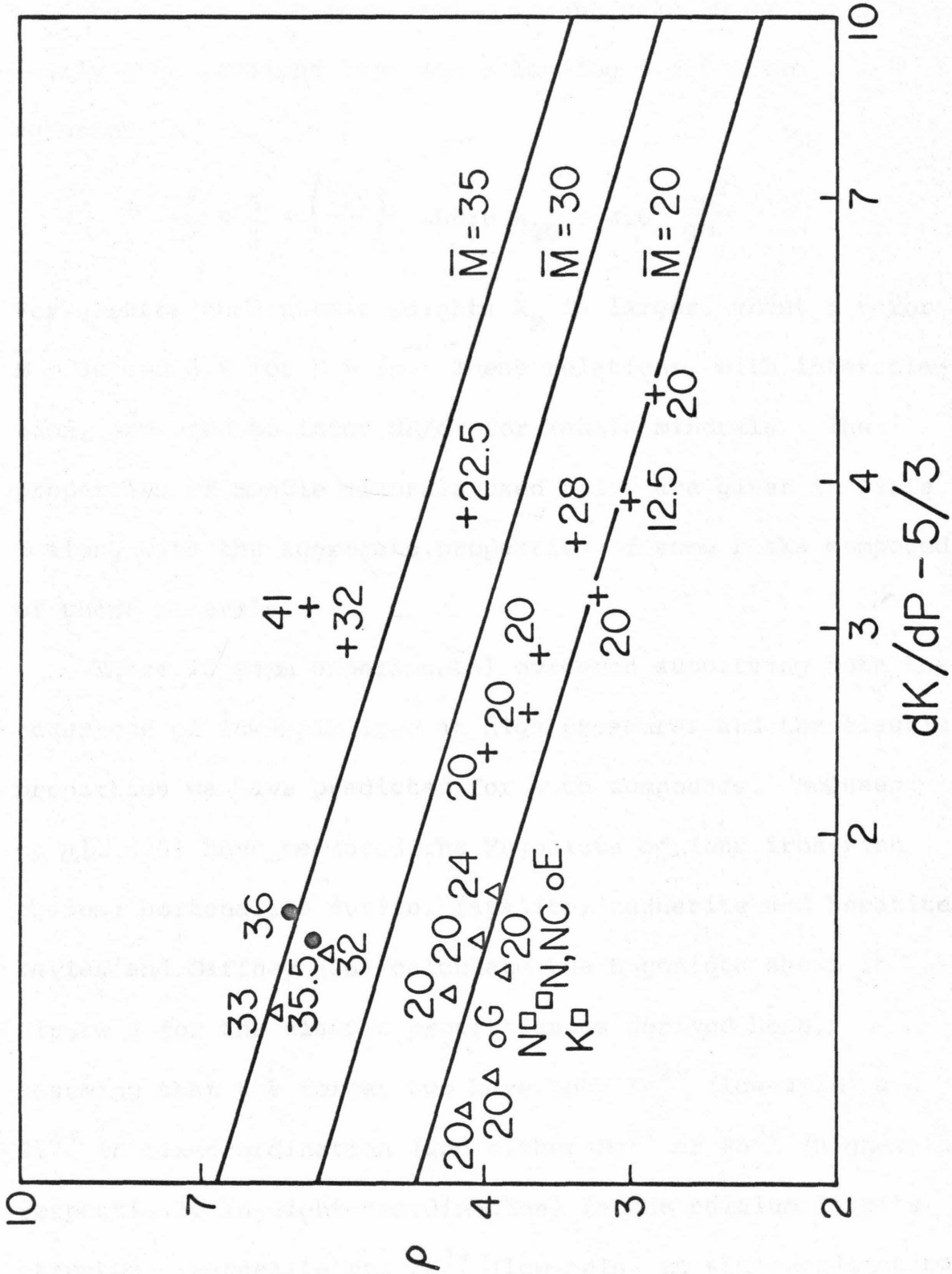
10
7
4
3
2
ρ
2
3
4
7
10
dK/dP - 5/3
M̄ = 35
M̄ = 30
M̄ = 20
+22.5
+28
12.5
20
41
+32
36
33
35.5
32
24
N□ □N, NC oE
K□
oG

but the points with mean atomic weight near 20 define a fairly good straight line (on a log-log plot) whose equation is

$$\frac{dK}{dP} = \frac{5}{3} + \left(\frac{k_{20}}{\rho}\right)^3 \quad \text{where } k_{20} = 4.6 \ \frac{cm^3}{gm}$$

For greater mean atomic weights $k_M$ is larger, about 5.6 for $\bar{M} = 30$ and 6.8 for $\bar{M} = 35$. These relations, with interpolation, are used to infer dK/dP for mantle minerals. The properties of mantle minerals used below are given in Table 6 along with the aggregate properties of some rocks composed of those minerals.

There is some experimental evidence supporting both the occurance of low-spin iron at high pressures and the elastic properties we have predicted for such compounds. McQueen et al. (25) have measured the Hugoniots of four iron-rich phases: hortonalite dunite, fayalite, magnetite and hematite. Davies and Gaffney (26) calculate the Hugoniots shown in Figure 5 for the elastic properties as derived here, assuming that the former two have both $Fe^{2+}$ (low-spin) and $Si^{4+}$ in six-coordination (and either $Mg^{2+}$ or $Fe^{2+}$ (high-spin), respectively in eight-coordination) in the calcium ferrite structure, magnetite has $Fe^{3+}$ (low-spin) in six-coordination

TABLE 6. Properties of Mantle Minerals and Rocks

| Mineral Composition | Structure | $\rho_o$ | $\tilde{M}$ | $K_o$(kb) | $\phi_o$ | $K'_o$ |
|---|---|---|---|---|---|---|
| $(Mg_{.89}Fe_{.11})_2SiO_4$ | $Sr_2PbO_4$ | 4.02 | 21.07 | 2302 | 57.26 | 3.17 |
| | $K_2NiF_4$ | 4.17 | 21.07 | 2665 | 63.91 | 3.01 |
| $Mg_2SiO_4$ | $Sr_2PbO_4$ | 3.85 | 20.10 | 2272 | 59.00 | 3.37 |
| | $K_2NiF_4$ | 3.99 | 20.10 | 2621 | 65.69 | 3.20 |
| $Mg(FeSi)O_4$ (l.s.) | $CaFe_2O_4$ | 4.76 | 24.61 | 2900 | 60.92 | 2.69 |
| $NaAlSiO_4$ | $CaFe_2O_4$ | 3.90 | 20.29 | 2163 | 55.47 | 3.30 |
| $(Mg_{.89}Fe_{.11})SiO_3$ | ilmenite | 3.96 | 20.76 | 2280 | 59.57 | 3.23 |
| | perovskite | 4.28 | 20.76 | 3111 | 72.69 | 2.91 |
| $MgSiO_3$ | ilmenite | 3.84 | 20.08 | 2255 | 58.72 | 3.39 |
| | perovskite | 4.15 | 20.08 | 3076 | 74.12 | 3.02 |
| $FeSiO_3$ | ilmenite | 5.43 | 26.39 | 3740 | 68.88 | 2.45 |
| $CaSiO_3$ | perovskite | 3.97 | 23.23 | 3096 | 77.99 | 3.22 |
| $Al_{1.64}Cr_{.18}Fe_{.18}O_3$ | sapphire | 4.15 | 21.90 | 2032 | 48.95 | 3.02 |
| FeO (low spin) | rock salt | 7.55 | 35.93 | 4160 | 55.10 | 2.40 |
| $Fe_2SiO_4$ | $CaFe_2O_4$ | 5.6 | 29.1 | 3100 | 55.36 | 2.65 |

| Rock | Composition[a.] | $\rho_o$ | $\phi_o$ | $K_o$ | $K'_o$ | $\rho_{1600}$ | $\phi_{1600}$ |
|---|---|---|---|---|---|---|---|
| A | .36Ho+.64En (ilmenite) | 4.21 | 59.5 | 2503 | 3.13 | 4.04 | 56.0 |
| B | .33Ho+.67Fo(str. plumb.) | 4.13 | 60.6 | 2503 | 3.22 | 3.97 | 57.1 |
| C | .33Ho+.67Fo($K_2NiF_4$) | 4.25 | 64.0 | 2720 | 3.03 | 4.08 | 60.8 |
| D | .33Fs+.67Fo($K_2NiF_4$) | 4.35 | 66.5 | 2894 | 2.95 | 4.18 | 63.5 |
| E | .22Ho+.11Fs+.67En(perovskite) | 4.46 | 70.5 | 3142 | 2.88 | 4.28 | 67.8 |
| P1 | | 4.00 | 58.5 | 2339 | 3.20 | 3.84 | 54.7 |
| P2 | c | 4.03 | 60.0 | 2416 | 3.25 | 3.87 | 56.2 |
| P3 | c, d | 4.05 | 61.1 | 2474 | 3.23 | 3.89 | 57.5 |
| P4 | a, c | 4.08 | 62.1 | 2534 | 3.17 | 3.92 | 58.6 |
| P5 | b, c, d | 4.12 | 65.1 | 2681 | 3.13 | 3.96 | 61.7 |
| P6 | a , c, d | 4.13 | 66.2 | 2732 | 3.14 | 3.97 | 62.9 |
| P7 | b, c | 4.13 | 62.9 | 2598 | 3.36 | 3.97 | 59.5 |
| P8 | a, b, c | 4.19 | 64.1 | 2687 | 3.08 | 4.02 | 60.8 |
| P9 | a, b, c, d | 4.20 | 68.2 | 2864 | 3.05 | 4.03 | 65.1 |
| P10 | a, b, c, d, e | 4.24 | 69.3 | 2938 | 3.00 | 4.07 | 66.3 |

a. Ho = $MgFeSiO_4$(Calc. ferr.)
En = $MgSiO_3$
Fo = $Mg_2SiO_4$
Fs = $FeSiO_3$(ilmenite)
for rocks P1-P10 composition is that of pyrolite
a, b, c, d, and e indicate that those reactions (see text p. )have occurred.
a and b refer to any composition $M_2SiO_4$ and $MSiO_3$ respectively

Figure 5a

Predicted Hugoniot of hortonalite dunite assuming high pressure phase is $MgFe(l.s.)SiO_4$ in a calcium ferrite structure with the properties given in Table 7. O - experimental data (25), ⊢ - initial density, ↓ - zero pressure density of high pressure phase.

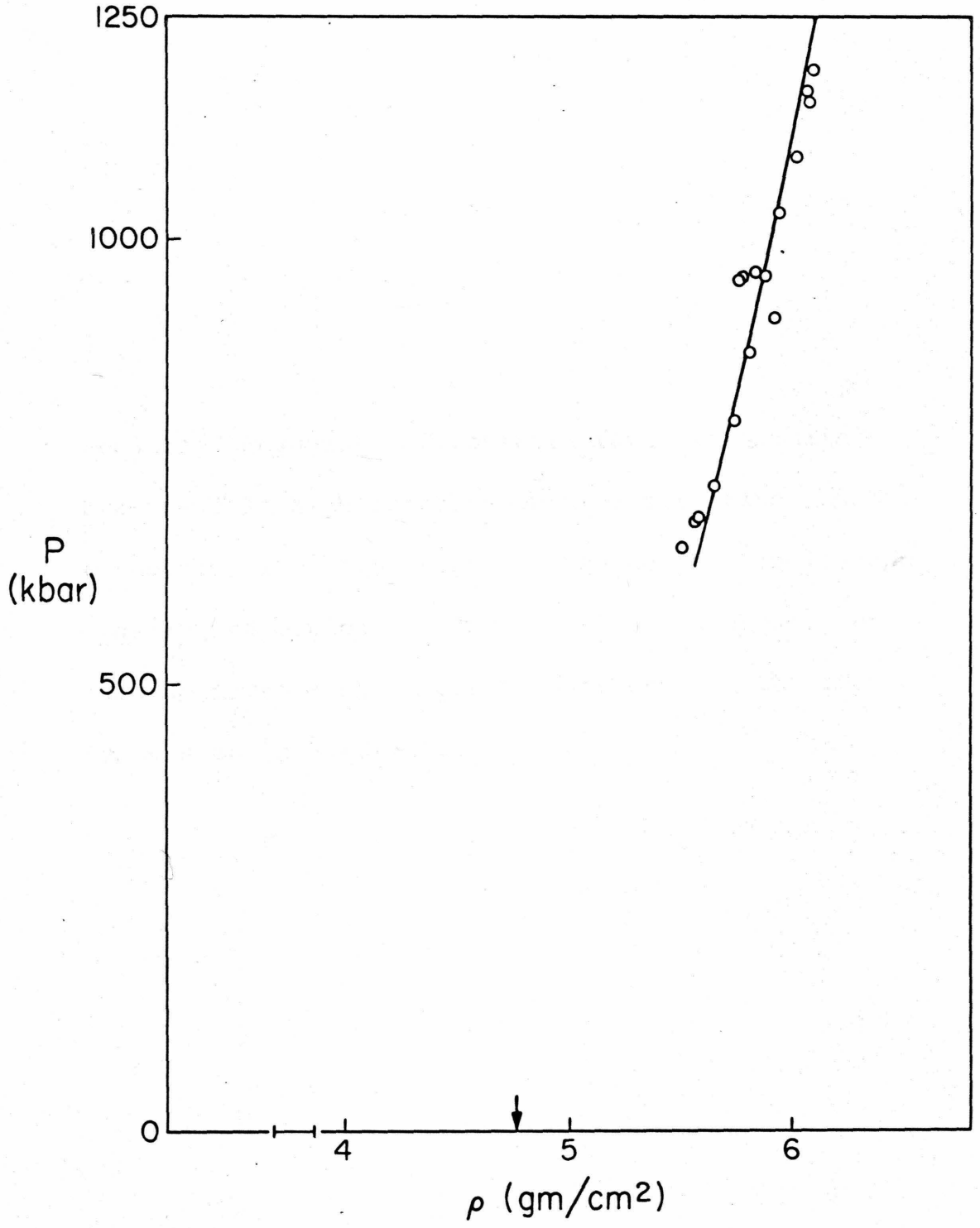
1250
1000
500
0
P
(kbar)
4
5
6
ρ (gm/cm²)

Figure 5b

Predicted Hugoniots of Rockport fayalite assuming two possible high pressure phases: strontium plumbate structure with high-spin iron having the density and elastic properties of wustite plus stishovite, or calcium ferrite structure as discussed in the text. Symbols as in Figure 5a.

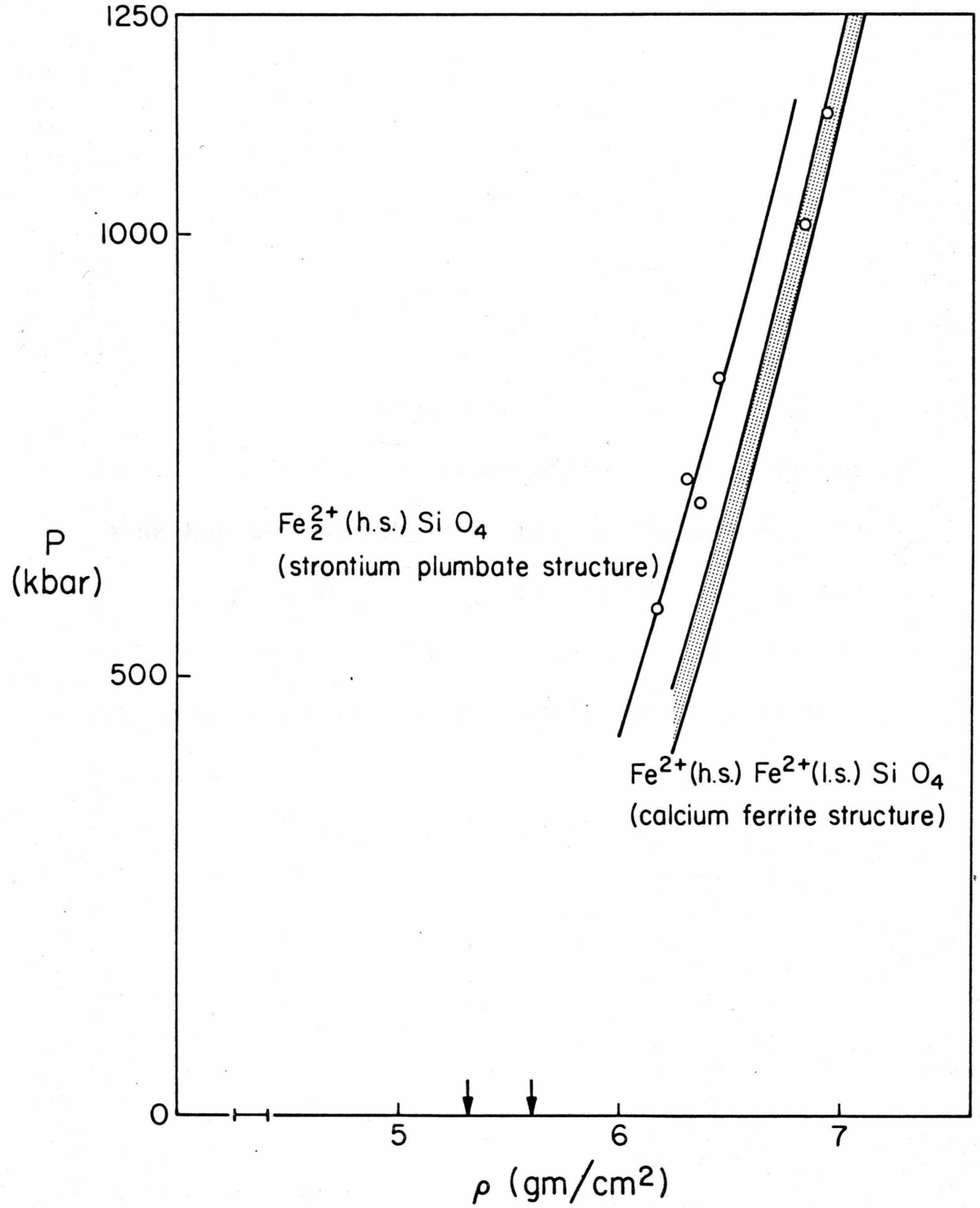
1250
1000
500
0
P
(kbar)
$Fe_2^{2+}$ (h.s.) Si $O_4$
(strontium plumbate structure)
$Fe^{2+}$(h.s.) $Fe^{2+}$(l.s.) Si $O_4$
(calcium ferrite structure)
5
6
7
ρ (gm/cm²)

Figure 5c

Hugoniot of hematite assuming that high pressure phase has the density appropriate for low-spin $Fe^{3+}$ in a corundum structure. The bulk-modulus of the high pressure phase has been chosen so as to fit the data of McQueen et al. (25). Symbols as in Figure 5a.

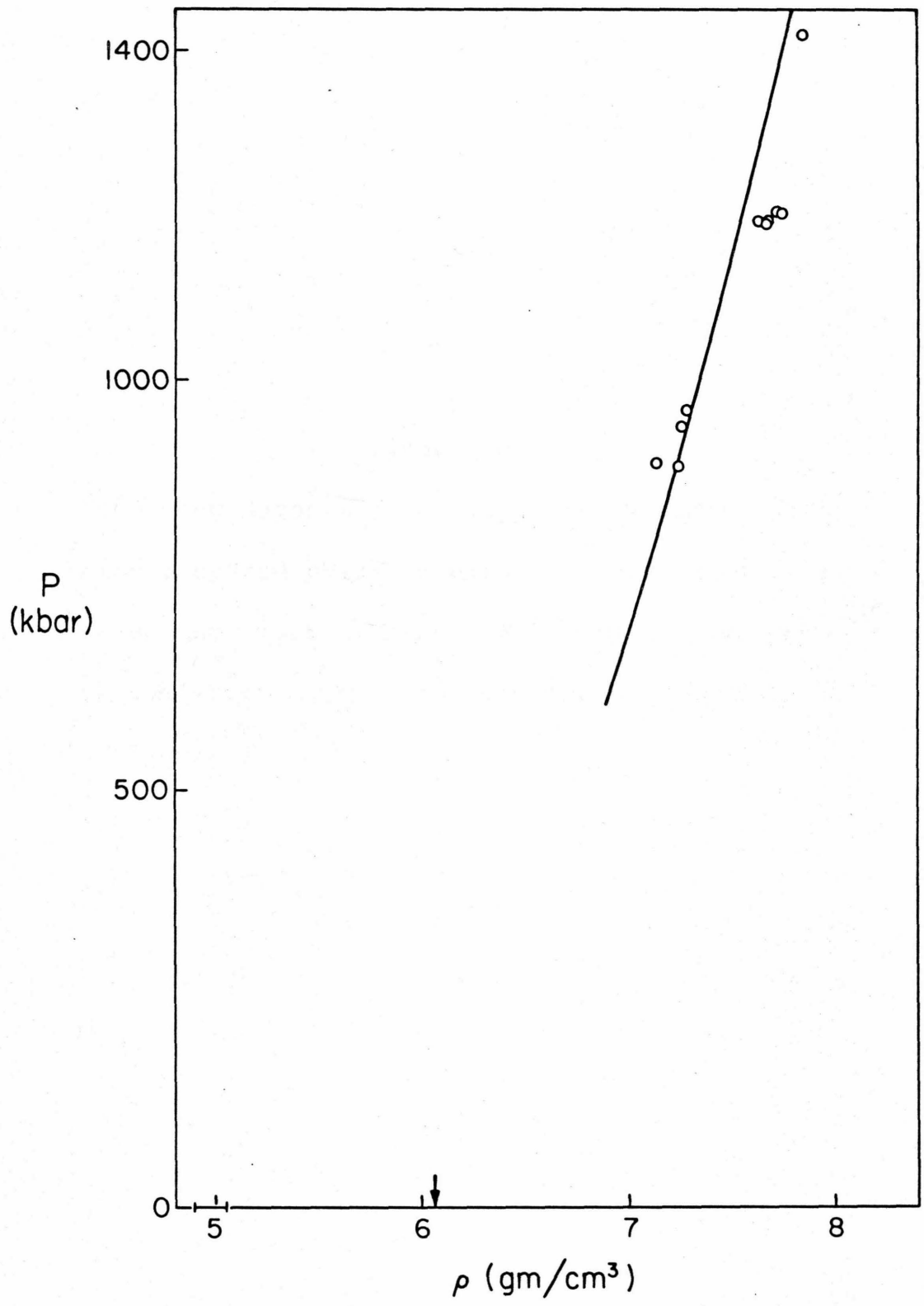
1400
1000
500
0
P
(kbar)
5
6
7
8
ρ (gm/cm³)

Figure 5d

Predicted Hugoniots for magnetite assuming that the high pressure phase is either a calcium ferrite structure (with high-spin $Fe^{2+}$ and low-spin $Fe^{3+}$) or a mixture of the low-spin oxides. Symbols as in Figure 5a.

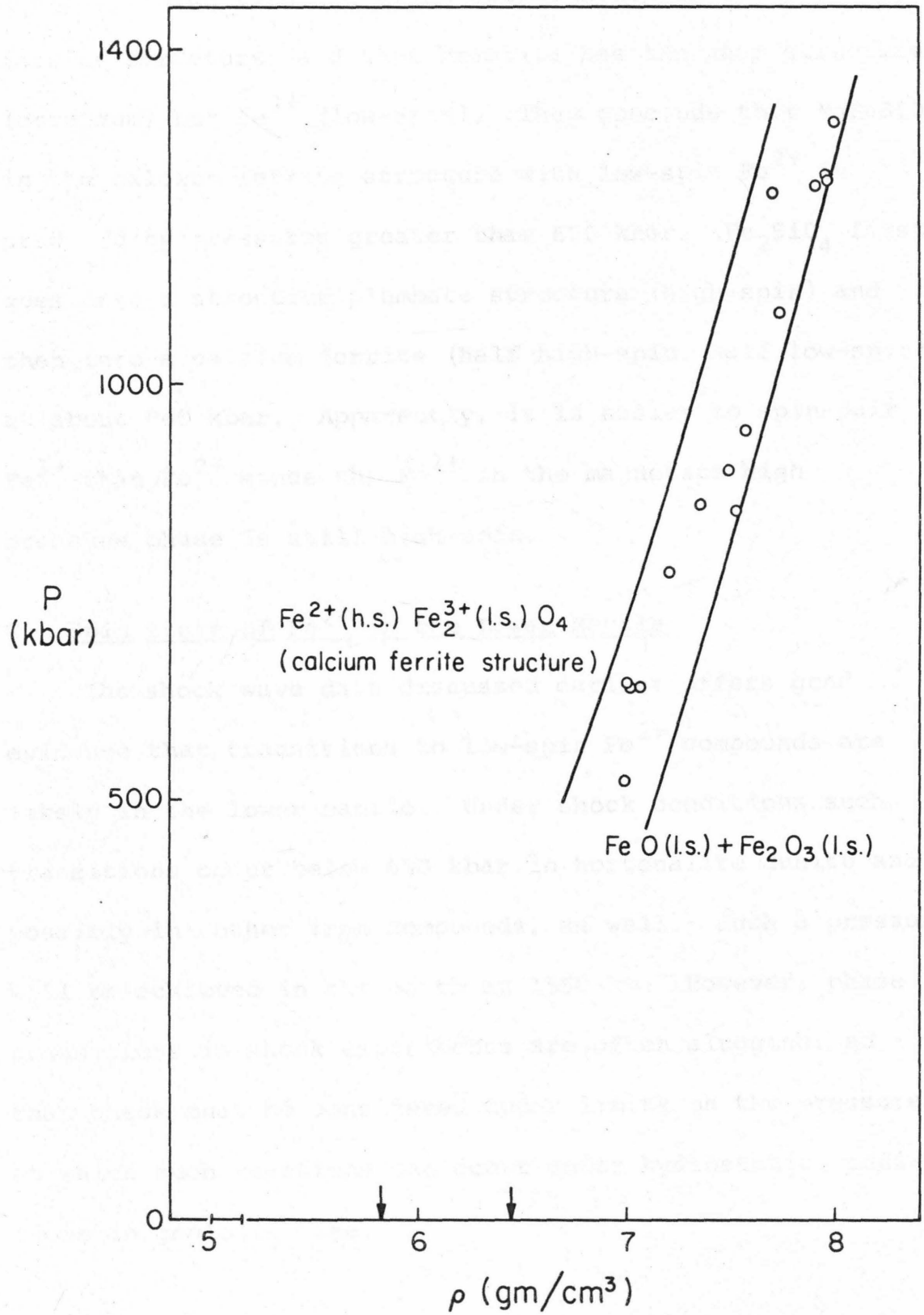
1400
1000
500
0
P
(kbar)
Fe2+(h.s.) Fe23+(l.s.) O4
(calcium ferrite structure)
Fe O (l.s.) + Fe2 O3 (l.s.)
5
6
7
8
ρ (gm/cm3)

and $Fe^{2+}$ (high-spin) in eight-coordination in the calcium ferrite structure, and that hematite has the same structure (corundum) but $Fe^{3+}$ (low-spin). They conclude that $MgFeSiO_4$ in the calcium ferrite structure with low-spin $Fe^{2+}$ is produced by pressures greater than 650 kbar. $Fe_2SiO_4$ first goes into a strontium plumbate structure (high-spin) and then into a calcium ferrite (half high-spin, half low-spin) at about 900 kbar. Apparently, it is easier to spin-pair $Fe^{3+}$ than $Fe^{2+}$ since the $Fe^{2+}$ in the magnetite high pressure phase is still high-spin.

C. Spin State of $Fe^{2+}$ in the Lower Mantle

The shock wave data discussed earlier offers good evidence that transitions to low-spin $Fe^{2+}$ compounds are likely in the lower mantle. Under shock conditions such transitions occur below 650 kbar in hortonalite dunite and possibly in other iron compounds, as well. Such a pressure will be achieved in the earth at 1550 km. However, phase transitions in shock experiments are often sluggish, so that these must be considered upper limits on the pressures at which such reactions can occur under hydrostatic conditions in geologic time.

In Chapter II the variation of the crystal field parameter with compression was discussed. The crystal field was separated into a part proportional to $r^{-3}$ and a part proportional to $r^{-5}$ where r is the interatomic distance between the transition metal and the coordinated ion. This technique worked fairly well in predicting the zero pressure spectra of several ferrous iron compounds. It was shown in Chapter IV that this point charge model predicts the behavior of the spectrum of ruby with up to 15% volume compression. This model is used below and the results are expected to be accurate to about 10 to 20 percent as before.

The problem of crystal field effects is more complicated if we wish to consider the possibility of spin-pairing. The energy difference between states of different spin-multiplicity will depend not only on the crystal fields but also on the magnitude of the electron repulsion energy. This energy enters into the calculation by way of the Racah parameters, B and C.

In an octahedral site the crystal field energy required to induce spin-pairing in $Fe^{2+}$ will be about 4C + 2 1/2 B (14). As the interatomic distance decreases increased covalent bonding is expected to lower B and C. Indeed, the

value of B and C in $Fe^{2+}$ in minerals is less than that of the free-ion as shown in Chapter III. However, no simple relation between B, C and R can be derived. In the models below both $r^3$ and $r^6$ are used as the variability of B and C with R.

Calculations of crystal field strengths combined with knowledge of the Racah parameters provides another means of bounding the pressures required to produce spin-pairing. The pressure required to induce spin-pairing in the high-spin phases such as $(Mg, Fe)_2SiO_4$ spinel or $(Mg, Fe)SiO_3$ ilmenite will be an upper limit since the spin-paired state could be achieved earlier in some phase peculiar to low-spin $Fe^{2+}$ (such as $MgFeSiO_4$ in the calcium ferrite structure). The upper limits are more than 1 Mbar for $(Mg, Fe)_2SiO_4$ (strontium plumbate structure) and $(Mg, Fe)SiO_3$ (ilmenite). However, for wustite using Mizutani et al.'s (22) elastic data and dK/dP from Figure 4 transition pressures at 0° C will be 370 and 250 kbar for the lower and upper limits on the variability of B and C from Chapter III. At the higher temperatures of a geotherm, spin-pairing is predicted at 460 and 340 kbar (1200 km and 900 km). Although FeO is probably not a separate phase in the mantle this will

still be a good upper limit on the pressures of the high- to low-spin transition. As pointed out by Strens (27) the local compressibility about $Fe^{2+}$ in most oxides and silicates is probably much less variable than the bulk compressibility of the host. (It should be noted that this is not the same calculation as that undertaken by Strens (27). He attempted to estimate an equilibrium between FeO (h.s.) and FeO (l.s.). Furthermore, although he did use B and C lower than the free-ion values, he did not consider them to decrease further upon compression. Data cited at the end of Chapter III were thus not considered.) Static compression studies of FeO up to 300 kbar (28) indicate that the $r^6$ upper limit for variability of B and C is too high. No discontinuity in the lattice constant was seen up to 300 kbar, but the occurance of spin-pairing should very certainly produce one because no change in structure (only in spacing) is required.

On the other hand, the lower limit of stability of low-spin $Fe^{2+}$ in these low-spin phases will be a lower limit on the transition pressures. The low-spin compounds are

predicted to be low-spin even at zero pressure.* The result is that, with the present inaccuracies, primarily in predicting the Racah parameter, it is not possible to predict the exact pressure at which spin-pairing can be expected in the lower mantle. Further experimental work, especially at low pressures on hortonalite is required to resolve this difficulty. Nonetheless we are assured that below 1200 km any $Fe^{2+}$ in the earth's mantle will be spin-paired, and this reopens the question of the composition of the lower mantle.

D. Composition of the Lower Mantle

Given that $Fe^{2+}$ will be in a low-spin state somewhere in the lower mantle we turn to an investigation of its effects on geophysically observable quantities. The effect on the importance of radiative transfer was discussed earlier and the general results of that argument are still valid, i.e., radiative transfer will be important if $Fe^{2+}$ is spin-paired but will be inhibited by crystal field absorption if it is not spin-paired.

---

* That is not to say that they are thermodynamically stable, only that if they did exist at zero pressure they would be low-spin.

Using the elastic properties given earlier (Table 6) the density $\rho$ and the seismic parameter $\Phi$ can be calculated for various minerals and rocks in the mantle. A Murnaghan equation rather than a Birch-Murnaghan equation is used to extrapolate to high pressures because it is probably more appropriate for small dK/dP such as have been adopted. The calculations were carried out using the continental geotherm of Stacy (29) with $dK/dP = -1.5$ kbar/deg and $\alpha = 25 \times 10^{-6}$. An initial set of calculations was done using Ringwood's pyrolite composition with high pressure transitions (a) through (e) occuring at a variety of levels. The range of the calculated $\Phi (=K/\rho)$ and $\rho$'s is shown in Figure 6. Values deduced from seismic data by Jordan and Anderson (30) are shown for comparison. The densities are much too low throughout the lower mantle although the $\Phi$'s are acceptable. Agreement is best above 800 km where a pyrolite composition is barely possible. This is not surprising since pyrolite composition was, in fact, designed on the basis of upper mantle data. In the region above 800 km the best pyrolite model has $Fe^{2+}$ spin-paired in $MgFeSiO_4$ (calcium ferrite structure). No fit of pyrolite to the data can be obtained

Figure 6

Range of values calculated for density (vertical pattern) and seismic parameter (horizontal pattern) with a pyrolite bulk composition. Observed values (30) are given for comparison.

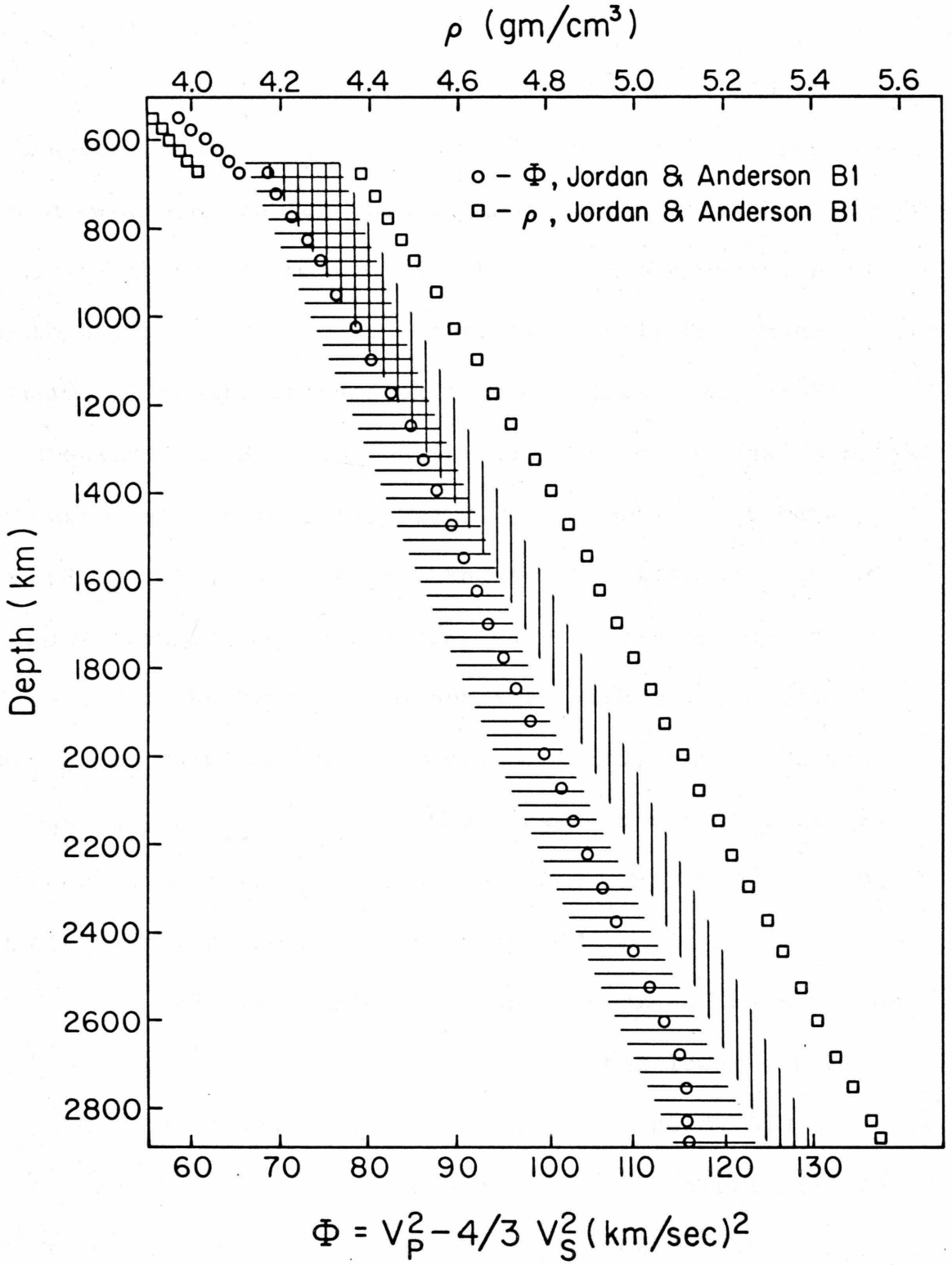
ρ (gm/cm³)
4.0
4.2
4.4
4.6
4.8
5.0
5.2
5.4
5.6
o – Φ, Jordan & Anderson B1
□ – ρ, Jordan & Anderson B1
Depth (km)
600
800
1000
1200
1400
1600
1800
2000
2200
2400
2600
2800
60
70
80
90
100
110
120
130
Φ = V_P^2 – 4/3 V_S^2 (km/sec)^2

with high-spin iron. Below 800 km, no phase assemblage with a pyrolite composition fits the data.

Plotting the probable major mineral data and the observed seismic data in a $\rho$-$\Phi$ plot for various pressures on a geotherm one can then estimate the mineralogic composition of the lower mantle and then check the estimate as with the pyrolite model. Considering only Mg, Fe and Si in $MgSiO_3$ (ilmenite or perovskite structure), $(Mg, Fe)SiO_3$ (ilmenite), $Mg_2SiO_4$ (strontium plumbate or potassium nickel fluoride structure), $(Mg, Fe)_2SiO_4$ (strontium plumbate), $MgFeSiO_4$ (calcium ferrite), and $FeSiO_3$ (ilmenite) the seismic results can be fit very well as can be seen in Figure 7. The best fit is obtained with a composition $Mg_{1.67}Fe_{.33}SiO_4$ at 650 km varying, fairly smoothly, to about $Mg_{.89}Fe_{.33}SiO_{3.21}$ at the core-mantle boundary. The latter value corresponds to .40 MgO + .15 FeO + .45 $SiO_2$ (mole fraction) which can be compared to .38 MgO + .16 FeO + .46 $SiO_2$ (mole fraction) determined by Anderson (31) to be the average composition of the lower mantle. All of the iron in this model is spin-paired below 630 km. Above about 1500 km the low-spin ferrous mineral will be $MgFeSiO_4$ but $FeSiO_3$ is present at greater depths. The

Figure 7

Density and seismic parameter for several possible mantle assemblages: —— A, --- B, ..... C, — -- — D, — — E.

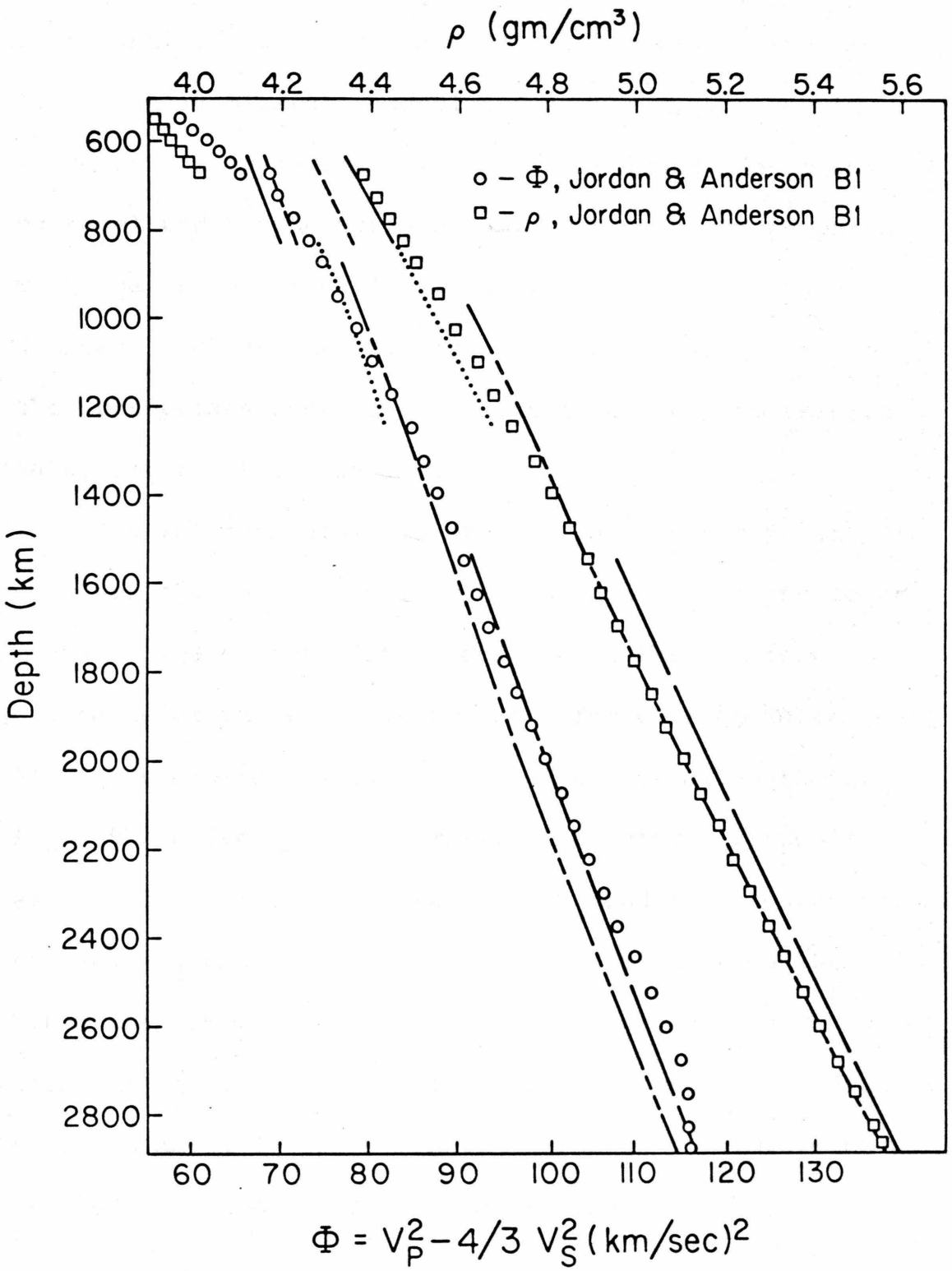
ρ (gm/cm³)
4.0
4.2
4.4
4.6
4.8
5.0
5.2
5.4
5.6
o – Φ, Jordan & Anderson B1
□ – ρ, Jordan & Anderson B1
Depth (km)
600
800
1000
1200
1400
1600
1800
2000
2200
2400
2600
2800
60
70
80
90
100
110
120
130
Φ = V_P^2 – 4/3 V_S^2 (km/sec)^2

values for $\rho_0$ and $\Phi_0$ in Table 6 range from 3.97 to 4.28 $g/cm^3$ and 56.0 to 67.8 $(km/sec)^2$ respectively for the lower mantle mineral assemblages at P = 0, T = 1600° C which is the approximate value of the lower mantle adiabat extrapolated to the surface (32). This can be compared with the values of 4.11 - 4.14 $g/cm^3$ and 55.0 - 57.5 $(km/sec)^2$ determined by Anderson and Jordan (2) to be the appropriate average values, determined from seismic data, for the lower mantle.

A brief comment is in order regarding the possibility of other elements, primarily Al, Ca and Na, in the lower mantle. The effect of the addition of the oxides or silicates of these metals can be inferred from Table 6. All three minerals will lower the density although for $Al_2O_3$ the effect will be small. The seismic parameters will be lowered by addition of $Al_2O_3$ and to a lesser extent by $NaAlSiO_4$ but will be raised by addition of $CaSiO_3$. Since the fit to the density of the lower mantle is quite good but the calculated $\Phi$ is somewhat too high, additions of up to about 10 percent $Al_2O_3$ might be possible without jeoprodizing the fit to the observations. Only small

amounts of $NaAlSiO_4$ and $CaSiO_3$ can be accomodated, however, because of their large effect on density.

E. Origin of the Upper Mantle

The likelihood of iron and silicon enrichment in the lower mantle relative to the upper mantle has been shown. The presence of a separate phase containing $Fe^{2+}$ will greatly facilitate such a process if it does occur. At low pressures in silicate systems, it is usually found that silica and iron are concentrated in the early melting components, so they might be removed by any type of partial melting. However, at several hundred kilobars Si should be six-coordinated and $Fe^{2+}$ should be spin-paired, so there is no reason to expect behavior similar to that at low pressures. Indeed $Fe^{2+}$ should prefer the solid to the liquid if spin-paired by extension of the argument of Burns and Fyfe (33) and Curtis (34). This effect should be accentuated by the small ionic radius of $Fe^{2+}$ (low-spin). So it can be expected that if the lower mantle were ever partially molten that it should be enriched in iron relative to, say, the upper mantle which would receive the early melt. If the $Fe^{2+}$ solid being left behind in the lower

mantle were $FeSiO_3$ some silica enrichment would also occur. Low-spin $Fe^{2+}$ in the lower mantle provides a convenient mechanism for iron (and perhaps silicon) enrichment in the lower mantle, and its elastic effects do not remove the imperative from seismological data that such enrichment exists. It seems, therefore, that the upper mantle is a differentiate of the whole mantle just as basalt is commonly regarded as a differentiate of the upper mantle (pyrolite).

The upper mantle, for which pyrolite can be taken as a good approximation, contains much less FeO and $SiO_2$ than inferred here for the lower mantle. A recent model by Ahrens (35) likewise has less FeO. Ringwood (4) has considered the whole mantle to be uniform in composition and, therefore, to be deficient in $SiO_2$ and FeO compared to carbonaceous chondrites, the presumed parent material for the Earth and the other terrestrial planets. He, therefore, devised a scheme by which ferromagnesian silicates were reduced in the high temperature, terminal stages of accretion and the reduced Fe and Si entered the core, thereby depleting the mantle in FeO and $SiO_2$. The present composition of the mantle can be matched by chondrite abundances (3) and this removes the motivation to expose the mantle

material to the reduction processes envisaged by Ringwood (4) and also removes the main argument that silicon is the light alloying element in the core.

REFERENCES

(1) D. L. Anderson, Chemical inhomogeneity of the mantle. Earth Planet. Sci. Letters 5, 89-94 (1968).

(2) D. L. Anderson and T. Jordan, The composition of the lower mantle. Phys. Earth Planet. Interiors 3, 23-35 (1970).

(3) D. L. Anderson, C. Sammis and T. Jordan, Composition and evolution of the mantle and core. Science 171, 1103-1112 (1971).

(4) A. E. Ringwood, The chemical composition and origin of the earth. P. Hurley (ed.), Advances in Earth Science. MIT Press, Boston, 287-356 (1966).

(5) S. P. Clark, Jr., Radiative transfer in the earth's mantle. Trans. Am. Geophys Un. 38, 931-938 (1957).

(6) E. S. Gaffney, Crystal field effects in mantle minerals. Phys. Earth Planet. Interiors (in press, 1972).

(7) A. E. Ringwood, Phase transformations and the constitution of the mantle. Phys. Earth Planet. Interiors 3, 109-155 (1970).

(8) W. H. Baur and A. A. Kahn, Rutile-type compounds. IV. $SiO_2$, $GeO_2$ and a comparison with other rutile-type structures. Acta Cryst. B27, 2133-2139 (1971).

(9) D. L. Anderson, Bulk modulus-density systematics. J. Geophys. Res. 74, 3857-3864 (1969).

(10) D. L. Anderson and O. L. Anderson, The bulk modulus-volume relationship for oxides. J. Geophys. Res. 75, 3494-3500 (1970).

(11) R. D. Shannon and C. T. Prewitt, Effective ionic radii in oxides and fluorides. Acta Cryst. B25, 925-946 (1969).

(12) G. A. Novak and G. V. Gibbs, The crystal chemistry of the silicate garnets. Am. Mineralog. 56, 791-825 (1971).

(13) R. G. Burns, Mineralogical Applications of Crystal Field Theory. 224 pp., Cambridge Univ. Press, Cambridge (1970).

(14) J. S. Griffiths, The Theory of Transition-Metal Ions. p. 238, Cambridge Univ. Press, Cambridge (1966).

(15) D. R. Stephens and H. G. Drickamer, Effect of pressure on the spectra of certain complexes of $Cu^{++}$, $Co^{+++}$, and $Fe^{++}$. J. Chem. Phys. 35, 424-426 (1961).

(16) G. H. Faye and E. H. Nickel, The effect of charge-transfer processes on the color and pleochroism of amphiboles. Can. Mineralog. 10, 616-635 (1970).

(17) A. S. Balchan and H. G. Drickamer, Effect of pressure on the spectra of olivine and garnet. J. Appl. Phys. 30, 1446-1447 (1959).

(18) R. G. J. Strens, Pressure-induced spin-pairing in gillespite, $BaFeSi_4O_{10}$. Chem. Comm. 777 (1966).

(19) L. R. Johnson, Array measurements of P velocities in the lower mantle. Bull. Seism. Soc. Am. 59, 973-1008 (1969).

(20) J. H. Whitcomb and D. L. Anderson, Reflection of P'P' seismic waves from discontinuities in the mantle. J. Geophys. Res. 75, 5713-5728 (1970).

(21) A. F. Reid, A. D. Wadsley and A. E. Ringwood, High pressure $NaAlGeO_4$, a calcium ferrite isotype and model structure for silicates at depth in the earth's mantle. Acta Cryst. 23, 736-739 (1967).

(22) H. Mitzutani, Y. Hamano, S. Akimoto, and O. Nishizawa. Elasticity of stishovite and wustite (abs.). Trans. Am. Geophys. Un. 53, 527 (1972).

(23) O. L. Anderson, E. Schreiber, R. L. Lieberman, N. Soga. Elastic constant data on minerals. Rev. Geophys. 6, 491-524 (1968).

(24) G. F. Davies and D. L. Anderson, Revised shock-wave equations of state for high-pressure phases of rocks and minerals. J. Geophys. Res. 76, 2617-2627 (1971).

(25) R. G. McQueen, S. P. Marsh, and J. N. Fritz, Hugoniot equations of state of twelve rocks. J. Geophys. Res. 72, 4999-5036 (1967).

(26) G. F. Davies and E. S. Gaffney, Equations of state of shock-induced high pressure phases of rocks and minerals. (manuscript in preparation).

(27) R. G. J. Strens, The nature and geophysical importance of spin pairing in minerals of iron (II). S. K. Runcorn (ed.) The Application of Modern Physics to the Earth and Planetary Interiors. Academic Press, New York, 213-220 (1969).

(28) R. L. Clendenon and H. G. Drickamer, Lattice parameters of nine oxides and sulfides as a function of pressure. J. Chem. Phys. 44, 4223-4228 (1966).

(29) F. D. Stacy, Physics of the Earth, p. 259, Wiley and Sons, New York (1969).

(30) T. Jordan and D. L. Anderson, manuscript in preparation.

(31) D. L. Anderson, Petrology of the mantle. Mineral. Soc. Am. Spec. Paper 3, 85-93 (1970).

(32) S. P. Clark, Jr., and A. E. Ringwood, Density distribution and constitution of the mantle. Rev. Geophys. 2, 35-88 (1964).

(33) R. G. Burns and W. S. Fyfe, Site preference energy and selective uptakes of transition metal ions from a magma. Science 144, 1001-1003 (1964).

(34) C. D. Curtis, Applications of the crystal-field theory to the inclusion of trace elements in minerals during magmatic differentiation. Geochim. et Cosmochim. Acta 28, 389-403 (1964).

(35) T. J. Ahrens, Petrologic properties of the upper 670 km of the earth's mantle; geophysical implications. preprint (1972).

(36) P. M. Hill, H. S. Peiser and J. R. Rait, The crystal structure of calcium ferrite and $\beta$-calcium chromite. Acta. Cryst. 9, 981-986 (1956).

(37) B. F. Decker and J. S. Kasper, The structure of calcium ferrite. Acta Cryst. 10, 332-337 (1957).

(38) E. F. Bertaut, P. Blum and G. Magnano, Structures des vanadite, chromite et ferrite monoclacique. Bull. Soc. franc. Mineral. Crist. 79, 536-561 (1956).

(39) A. F. Reid and A. E. Ringwood, Newly observed high pressure transformations in $Mn_3O_4$, $CaAl_2O_4$, and $ZrSiO_4$. Earth Planet. Sci. Letters 6, 205-208 (1969).

(40) H. Müller-Buschbaum and H. G. Schnering, Über Oxocandate. I. Zur Kenntnis des $CaSc_2O_4$. Z. anorg. allgem. Chem. 336, 295-305 (1965).

(41) A. F. Reid, Calcium indate, an isotype of calcium ferrite and sodium scandium titanate. Inorg. Chem. 6, 631-633 (1967).

(42) H. Müller-Buschbaum, Über Oxoscandate. II. Zur Kenntnis des $MgSc_2O_4$. Z. anorg. allgem. Chem. 343, 113-120 (1966).

(43) J. R. Carter and R. S. Feigelson, Preparation and crystallographic properties of $A^{2+}B_2^{3+}O_4$ type calcium and strontium scandates. J. Am. Ceram. Soc. 47, 141-144 (1964).

(44) H. Schwarz and D. Bommert, Über ternäre Oxide des Indiums, Yttriums und der Saltenen Erden mit den Erdalkalimetallen Calcium, Strontium und Barium. Z. Naturforsch. 19b, 955-956 (1964).

# VI. SUMMARY

Iron is generally considered to be an important constituent of the earth's mantle. Its behavior will, to a great extent, be determined by crystal field effects on electronic energy levels. Crystal field theory has been briefly reviewed with particular emphasis on the point charge model which permits prediction of one electron energy levels. They are found to depend on interatomic distance R as $A_2/R^3 + A_4/R^5$. Given these, a complete energy level scheme can be obtained, for many symmetries, with the use of the two Racah parameters B and C. If absorption spectra are available the one electron energy levels can be determined from the location of spin-allowed bands and the Racah parameters, from the spin-forbidden bands.

The spectra of spinels, garnets, gillespite and olivines are investigated. After due consideration of electronic transitions in other elements, all of those containing $Fe^{2+}$ as the dominant transition metal are found to have features attributable to spin-forbidden transitions in $Fe^{2+}$. These bands are assigned and values of Racah parameters fit to the observed data with standard

deviations on the order of 1 - 2 percent. The resulting B's range from 582 $cm^{-1}$ to 797 $cm^{-1}$; C's from 2601 $cm^{-1}$ to 3457 $cm^{-1}$ with C/B always near 5. There is some indication that B and C decrease with interatomic distance but the effects of coordination are dominant. Previous work indicates that on compression B and C are proportional to $R^n$ where n = 3 to 6.

A new experimental technique has been developed for measuring time-resolved optical absorption spectra of solids during shock loading. The technique is used to demonstrate that shock stresses in excess of 465 kbar are required to produce substantial changes in the absorption spectrum of MgO. From a study of spectra of shocked ruby it can be determined that a) below the Hugoniot elastic limit (HEL) there are considerable non-hydrostatic strains, b) above the HEL these strains are not observable, and c) the variation of the crystal field parameter, Dq, with compression above the HEL follows the prediction of the point charge model.

Using the point charge model, as well as various systematic relationships between density and bulk elastic constants, the effects of $Fe^{2+}$ on the properties of the

lower mantle are predicted. It is found that the mantle below 670 km cannot be a pyrolite but must have more iron. Furthermore, this iron will be spin-paired. With $Fe^{2+}$ spin-paired in the lower mantle, radiative transfer will be considerably enhanced relative to the upper mantle. The best fit to the observed seismic data is obtained with a lower mantle varying from $Mg_{1.67}Fe_{.33}SiO_4$ at 650 km to $Mg_{.89}Fe_{.33}SiO_{3.21}$ at the core-mantle boundary. Considerable $Al_2O_3$ but only minor amounts of $NaAlSiO_4$ and $CaSiO_3$ can also be accomodated. It has been proposed that the upper mantle has been derived by chemical fractionation from the lower mantle.

# APPENDIX. DATA REDUCTION OF SHOCKED RUBY SPECTRA

The raw data from the spectrograph system (Chapter IV) are in the form of 4 x 5 inch Royal-X pan negatives. These are developed in Acufine developer yielding an effective ASA rating of 3000. The negatives were then scanned, digitized and stored on magnetic tape by JPL's Image Processing Laboratory. The spot size was 25 microns with a line spacing of 25 microns. All of the photographs of spectra shown here (Figures 1 and 2) and in Chapter IV are prints of negative produced in the scanning process as a check on the density scale in the scan.

The data were read off the tape line by line and averaged over four successive lines and plotted as shown in Figure 10 Chapter IV with the Calcomp plotter. The resulting curves were then smoothed by hand. These smoothed data were then analysed by subtracting later lines from a typical line just after shock arrival in the sample. Typical results of such data reduction are shown in Figures 3, 4 and 5. Absorptions behind the shock front will appear as positive features while those in front of the shock front will be negative features.

Figure 1

Digitized record of absorption spectrum of ruby shocked to 147 kbar. Time increasing downward, red on the right and violet on the left. Vertical scratch is at about 700 nm.

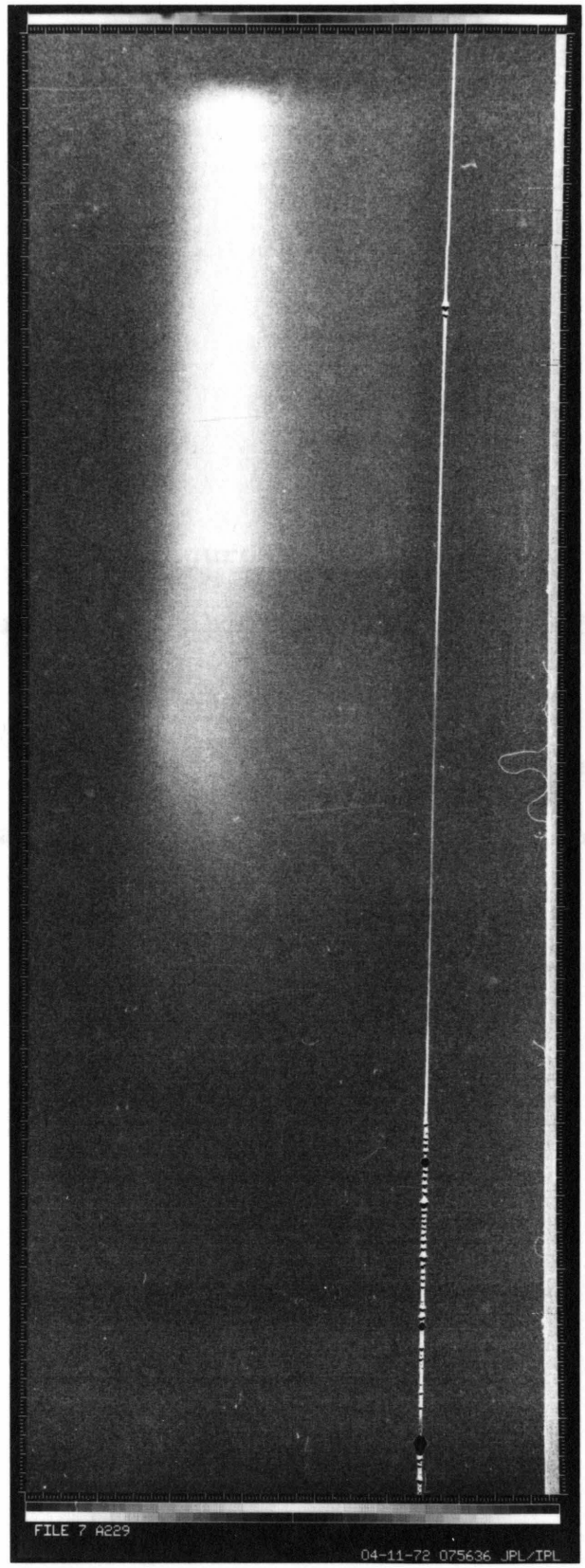
FILE 7 A229
04-11-72 075636 JPL/IPL

Figure 2

Digitized record of absorption spectrum of ruby shocked to 530 kbar final pressure. Time increasing downward. The three (overexposed) laser emission lines are at 457.9 nm, 488 nm and 514.5 nm from left to right.

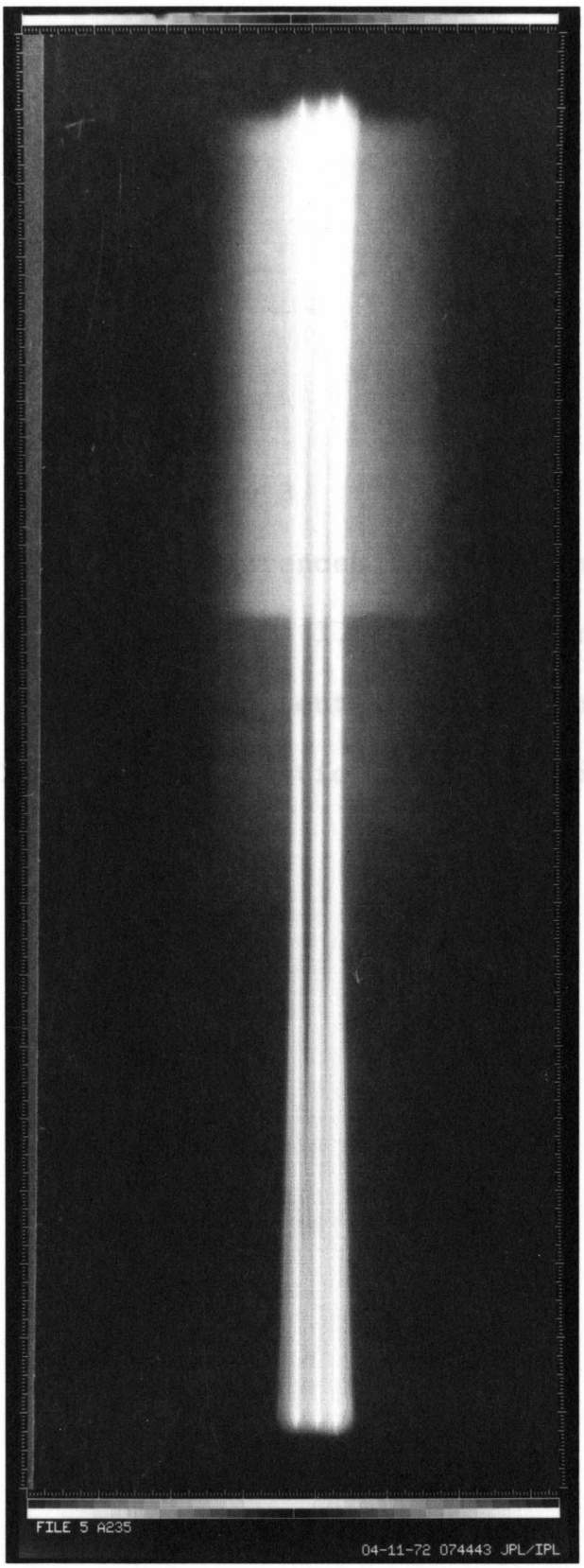
FILE 5 A235
04-11-72 074443 JPL/IPL

Figure 3

Two representative differences between lines in the photograph shown in Figure 1. A large number of absorption bands are apparent in this record which is below the Hugoniot elastic limit of sapphire.

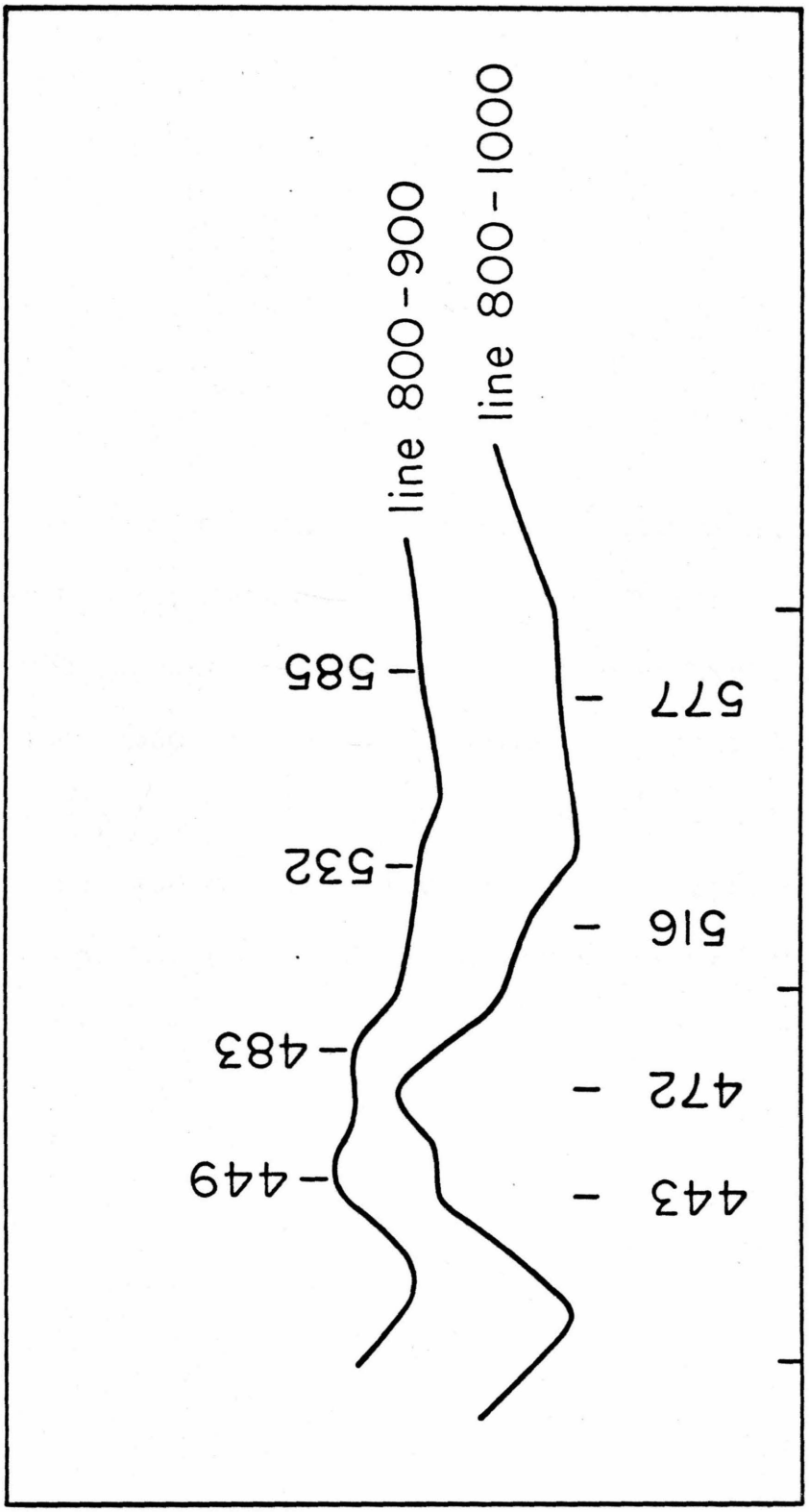
line 800-900
line 800-1000
585
532
483
449
577
516
472
443
400
500
600
λ(nm)

Figure 4

Two representative differences between lines in photograph shown in Figure 10, Chapter IV for ruby shocked to 430 kbar. The positive features at about 460 nm are due to absorption behind the shock front in the high pressure region. The features at about 400 and 550 nm are due to absorption in the unshocked region ahead of the shock front.

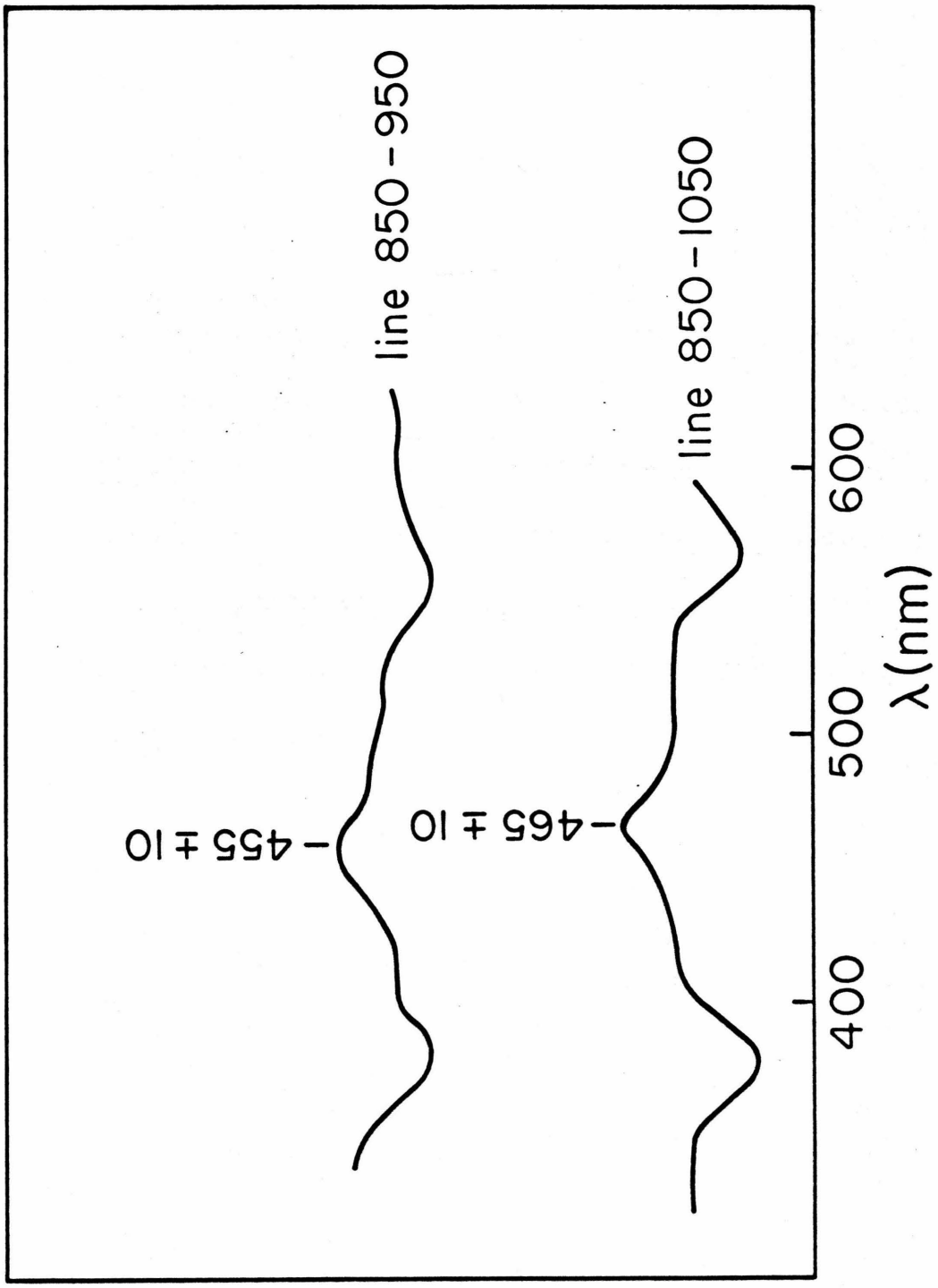
line 850-950
line 850-1050
455 ± 10
465 ± 10
400
500
600
λ(nm)

Figure 5

Two representative differences between lines in the photograph shown in Figure 2 for ruby shocked to 530 kbar. Unlike previous records this one shows absorption increasing at about 400 nm indicating strong absorption in the shocked medium there. There is a decrease in absorption at 550 nm as in lower pressure shots.

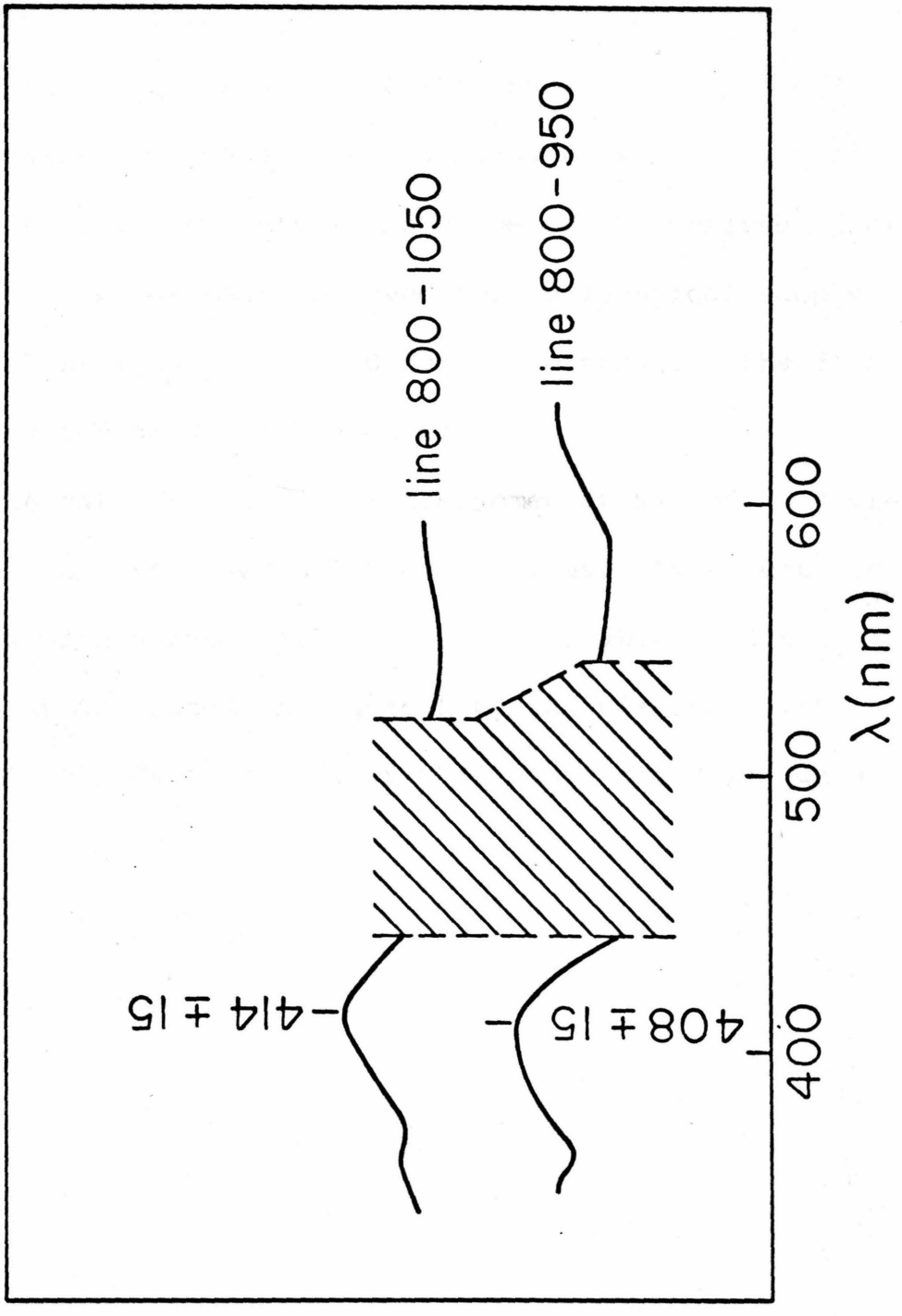
line 800-1050
line 800-950
414 ± 15
408 ± 15
400
500
600
λ(nm)

In one case (147 kbar shock pressure, Figures 1 and 3) there are no laser emission lines for wavelength calibration. In this case the dispersion on the negative was obtained by changing the spacing between data points for plotted results until the shape of the observed profiles were the same as that observed for an identical sample with calibration lines (430 kbar). Otherwise, the data were treated as described above.

The data from 530 kbar are somewhat marred by over-exposure of the laser calibration lines. This resulted in loss of any data between 440 nm and about 530 nm. This region is indicated in Figure 5 by the diagonal pattern. However, the data outside of this range are quite good.

## BIOGRAPHICAL NOTE

On a cold winter's night, 'twas in Brooklyn, New York,
That our hero was brought into life by The Stork
In the year nineteen hundred plus forty and three.
For the next sixteen years, betwixt forest and sea,
Oh, he wandered this country by air and by rail
'Til he finally settled on college at Yale.
It was there amongst young men who'd deal soon in stocks
He spelunked and began on his study of rocks.

And then, after B.S., nineteen sixty and four,
He continued his studies at Eliazar's door.
After two years, a Master in geology,
He began his return to the westernmost sea.
First a year out in Westwood with nothing to show,
And from there on to Caltech (well, wouldn't you know?).
It was here, under Rossman and Ol' Uncle Tom,
That he did all this junk. And to what will it come?